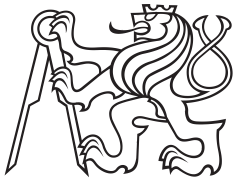

Czech
Technical
University
in Prague

F4

Faculty of Nuclear Sciences and Physical Engineering
Department of Physics

DOCTORAL THESIS

Enhanced Plasma Confinement in Tokamaks with Focus on the Turbulence-Flow Interaction

Prague 2021

Ondřej Grover

Bibliografický záznam

Autor	Ing. Ondřej Grover České vysoké učení technické v Praze, Fakulta jaderná a fyzikálně inženýrská Katedra fyziky
Název práce	Zlepšené udržení plazmatu v tokamacích se zaměřením na interakci turbulence a toků
Studijní program	Aplikace přírodních věd
Studijní obor	Jaderné inženýrství
Školitel	Ing. Martin Hron, Ph.D. oddělení Tokamak Ústav fyziky plazmatu AV ČR, v. v. i.
Školitel–specialista	Mgr. Jakub Seidl, Ph.D. oddělení Tokamak Ústav fyziky plazmatu AV ČR, v. v. i.
Akademický rok	2021
Počet stran	92
Klíčová slova	tokamak, zlepšené udržení, turbulence, H-mód, L-H přechod, limitní cyklové oscilace, I-mód

Bibliographic Entry

Author	Ing. Ondřej Grover Czech Technical University in Prague, Faculty of Nuclear Sciences and Physical Engineering Department of Physics
Title of Dissertation	Enhanced Plasma Confinement in Tokamaks with Focus on the Turbulence-Flow Interaction
Degree Programme	Applications of Natural Sciences
Field of Study	Nuclear Engineering
Supervisor	Ing. Martin Hron, Ph.D. Tokamak department Institute of Plasma Physics of the Czech Academy of Sciences
Supervisor–specialist	Mgr. Jakub Seidl, Ph.D. Tokamak department Institute of Plasma Physics of the Czech Academy of Sciences
Academic Year	2021
Number of Pages	92
Keywords	tokamak, enhanced confinement, turbulence, H-mode, L-H transition, limit cycle oscillations, I-mode

Abstrakt

Zlepšené udržení je klíčové pro úspěšné operování budoucích fúzních elektráren. Tato práce podává přehled stavu poznání škálování udržení v budoucích reaktorech typu tokamak a známých režimů se zlepšeným udržením. Práce se zaměřuje především na tzv. H-mód (mód vysokého udržení) a související úkazy jako např. limitní cyklové oscilace, studovány především v tokamaku COMPASS. Výzkum těchto oscilací vedl k vytvoření a zobecnění modelu založeného na prvních principech, který systematicky předpovídá pozorované frekvence tlakem uvolněných limitních cyklových oscilací v blízkosti přechodu do H-módu ve 4 tokamacích (JET, ASDEX Upgrade, COMPASS, Globus-M). Zobecnění tohoto modelu také přispělo k rozšíření jiného, ale souvisejícího modelu vyvinutého pro tokamak ASDEX Upgrade pro dosažení H-módu na libovolný druh iontů v plazmatu. Jsou také ukázány příspěvky ke studiu alternativního režimu udržení I-módu v tokamaku ASDEX Upgrade. Závěrem je robustně charakterizován vliv pozice X-bodu v oblasti divertoru na přechod do H-módu v tokamaku COMPASS a je také ukázáno jak jeho vliv otevřel cestu k režimu udržení bez okrajových nestabilit typu I s vlastnostmi H-módu i I-módu v tokamaku ASDEX Upgrade.

Abstract

Enhanced confinement is a key ingredient for successfully operating future fusion power plants. This thesis offers an overview of the current state of knowledge concerning scaling laws predicting confinement in future tokamak reactors and known enhanced confinement modes. The main focus of the thesis is the H-mode (high confinement mode) and associated phenomena such as limit cycle oscillations, primarily studied in the COMPASS tokamak. Studies of of these oscillations led to the development and generalization of a first-principles-based model which systematically predicts the observed frequency of pressure relaxation limit cycle oscillations in the vicinity of the transition to H-mode in 4 tokamaks (JET, ASDEX Upgrade, COMPASS, Globus-M). The generalization of the model also contributed to the extension of different, but related model for the H-mode access developed for the ASDEX Upgrade tokamak to arbitrary ion plasma species. The contribution to the study of the alternative confinement regime I-mode in the ASDEX Upgrade tokamak in are also reported. Finally, the impact of the X-point configuration within the divertor region on the H-mode access is robustly characterized in the COMPASS tokamak and is shown to open a path to an Type-I edge-localized-mode-free regime with both H-mode and I-mode features in the ASDEX Upgrade tokamak.

Contents

Introduction . . . 1
Goals of the thesis . . . 2
1 Enhanced confinement in tokamaks **3**
1.1 Confinement and scalings . . . 3
1.1.1 Scaling laws . . . 5
1.1.2 Confinement time scaling . . . 5
1.2 L-H transition and H-mode . . . 6
1.2.1 L-H power threshold scaling laws . . . 9
1.2.2 Ion heat flux and density dependence . . . 10
1.2.3 Divertor configuration and X-point dependence . . . 11
1.2.4 Isotope dependence . . . 12
1.2.5 Zonal flows and limit cycle oscillations . . . 12
1.2.6 Separatrix operational space . . . 14
1.3 Type-I ELM-free confinement regimes . . . 16
2 Experimental and theoretical analysis methods **19**
2.1 Tokamaks . . . 19
2.2 Powerlaw scaling regression analysis . . . 21
2.2.1 Causal graphical models . . . 23
2.3 DALF model of edge plasma turbulence . . . 25
3 Results **27**
3.1 L-H transition in the COMPASS tokamak . . . 27
3.1.1 Limit cycle oscillations measurements . . . 27
3.1.2 Dependence on the X-point position . . . 41
3.2 First-principles model of pressure relaxation LCO in tokamaks . . . 43
3.2.1 Further extensions of the model . . . 59
3.3 Generalization of the separatrix L-H transition model to arbitrary ion mass and charge . . . 60
3.3.1 Ion mass and Charge in interchange-drift-Alfvén turbulence (part of article draft) . . . 61
3.3.2 Impact of impurities (part of article draft) . . . 62
3.3.3 Ongoing and future work . . . 63
3.4 I-mode experiments in ASDEX Upgrade . . . 65
3.4.1 I-mode seeding experiments . . . 65
3.4.2 I-mode transition power threshold dependence . . . 66
3.4.3 Investigation of the I-mode separatrix operational space . . . 68
3.4.4 Search for I-mode in favorable ∇B drift . . . 70
4 Conclusions and Outlook **75**
4.1 General conclusions and summary . . . 77
4.2 Summary and declaration of direct contributions by the author . . . 78
Acknowledgments **79**
Nomenclature **81**
Bibliography **83**

Introduction

The human-kind's unending quest for ever-cleaner, cheaper, safer, denser and abundant energy sources has been motivated in the past centuries by the scarcity and finiteness of resources and an ever-increasing demand for energy [1]. This demand for environmentally clean energy has been accentuated in the last decades by the impending climate change crisis. While renewable energy sources such as wind turbines and solar panels can provide large amounts of electric power, the current unavailability of batteries or capacitors with sufficient storage capacity means that in many geographical locations baseline power sources such as conventional coal, gas or nuclear fission power plants are still required in a viable energy mix. However, the massive usage of fossil-fuel-based conventional baseline sources presents significant risks to the environment while political support for constructing new nuclear fission plants is limited.

Future fusion power reactors may be able to replace such baseline power sources in the second half of the 21. century according to the updated EUROfusion roadmap [2]. Preliminary analysis suggests that they would be an economically and environmentally viable alternative [3]. Achieving a ten-fold net power gain in the ITER reactor after 2035 is one of the most important milestones in the roadmap for fusion reactors to become a reality. The ITER reactor being currently constructed in France will be the culmination of an unprecedented international effort over the last three decades. Its size is the result of intensive international research in many different machines. In the past sixty years the steady progress towards achieving fusion power thanks to better confinement went hand in hand with the machines becoming larger as explained in section 1.1. Additionally, special regimes of enhanced confinement were discovered which should make it possible to reach the target with the proposed design.

In chapter 1 the current state of knowledge of enhanced confinement in tokamaks is summarized. The aim of the thesis is not to become a general tokamak physics textbook such as [4, 5] (which the reader likely knows well already), therefore, only specific specialist topics relating directly to the thesis are covered. Specifically, section 1.1 introduces issues with confinement in tokamaks due to turbulent transport, describes scalings of confinement time towards future reactors and discusses the issues of the currently employed methodology for creating scaling laws, section 1.2 then describes the H-mode (high confinement mode), currently the reference enhanced confinement scenario for ITER, its power threshold scalings and associated phenomena such as zonal flows an limit cycle oscillations. Finally, section 1.3 introduces various other enhanced confinement regimes which could be an alternative to the H-mode in the future.

The results obtained in the scope of this thesis by the author are shown in chapter 3. The investigation of the transition to H-mode in the COMPASS tokamak including the study of the associated limit cycle oscillations is reported in section 3.1. The subsequent development of an extended model

for such limit cycle oscillations in many different tokamaks is described in section 3.2. The resulting generalization of a model for the separatrix operational space in ASDEX Upgrade to Helium and other ion species is covered by section 3.3. Finally, section 3.4 shows the author's attempts to investigate the intermediate confinement (I-mode) regime as an alternative to H-mode in the ASDEX Upgrade tokamak.

Goals of the thesis

The primary goal of the thesis was to advance the understanding of the access to enhanced confinement regimes in tokamaks. More specifically the goal was to study the interaction between turbulence and flows in order to seek mechanisms leading to the transition to enhanced confinement.

Chapter 1

Enhanced confinement in tokamaks

1.1 Confinement and scalings

Future fusion tokamak reactors must operate in regimes with a characteristic confinement time τ_E in the order of several seconds in order to achieve sustainable thermonuclear fusion with net energy gain [5, 6]. The energy confinement time τ_E represents the characteristic time scale with which the plasma energy[1] W would exponentially decrease if all input heating power P_{heat} was turned off or lost and energy was being lost in the form of radiation and particles losses at a rate quantified by the loss power P_{loss} assumed to be proportional to W.

A large body of research [7] focuses on describing the energy losses due to particles being transported across magnetic field-lines, because they typically represent the dominant energy loss channel, since the hydrogen isotopes used in current tokamak experiments and planned tokamak reactors are (or are assumed to be) fully ionized throughout the majority of the plasma volume. Therefore, line radiation, bremsstrahlung or synchrotron radiation are not considered dominant energy loss channels. However, impurity accumulation originating e.g. from plasma-wall interaction can also lead to excessive radiation losses.

The particle transport has been historically described in the framework of a Fickian diffusion model [8] where the particle flux Γ is driven by the density gradient $\Gamma = -D\nabla n$ with a proportionality coefficient D characterizing the diffusion process. From a microscopic random walk argument the diffusion coefficient is assumed to be given by $D = (\Delta l)^2/\tau_c$ where Δl is the characteristic spatial step and τ_c the characteristic time between steps.

In the classical theory of tokamak plasma transport the characteristic time was taken to be the time between collisions (meant in the statistical sense of particle trajectories deviating beyond 90°) and the characteristic spatial step size as the (ion) gyroradius, because collisions cause particles to gyrate on a different orbit. As theory progressed into what is now called neoclassical

[1] Various sources and articles use different definitions of the plasma energy depending on the context and phenomena being discussed, e.g. the energy might be separated in that of thermal particles and fast/supra-thermal particles, ions, different ion species and electrons, etc.

transport theory, additional effects were taken into account, making the spatial step larger due to banana orbits of trapped particles and effective collision frequencies. However, even such refinements couldn't account for the actual diffusion coefficients measured in the experiments in the order of $D \sim 1\,\mathrm{m}^2/\mathrm{s}$, several orders of magnitude beyond the most refined neoclassical predictions.

Throughout most tokamak fusion-relevant experiments the effective diffusion coefficient estimated from experimental measurements as $D \approx -\Gamma/\nabla n$ is typically found to be in the same order of magnitude of $D \sim 1\,\mathrm{m}^2/\mathrm{s}$ [7]. Employing the simple random-walk argument of a core particle taking N steps to escape (and equating particle with energy loss for simplicity) over a characteristic time $\tau_E = N\tau_c$, the escaping particle is displaced up to the minor radius $a \sim \sqrt{\langle(\Delta l)^2\rangle}/N$. Therefore, the diffusion coefficient can be expected to scale as $D \approx a^2/\tau_E$. This scaling explains why progress in achieving greater confinement time on the road towards fusion has been mostly due to the steady increase in machine size, because the effective diffusion coefficient has remained mostly the same in all experiments.

The observations of the effective diffusion being several orders of magnitude faster than predicted by theory were initially called "anomalous" diffusion, but later were attributed to turbulent transport. This type of transport does not fit into the Fickian diffusion framework anymore, because it features small volumes of the plasma being transported in coherent structures due to their internal fields. Therefore, this transport is nearly ballistic (displacement is proportional to time of flight), non-markovian (structures carry information from the past - their origin) and non-local (not dependent only on local gradients).

These properties are all at odds with the simple Fickian diffusion model and also contribute to this being a generally very complex problem with no known general solution in the scope of classical physics. This motivates the investigation of turbulent spectra and other statistical properties of turbulent plasma time-series in the framework of multi-fractal analysis [9]. Such models predict and explain several trends in observed fluctuation spectra and other statistical properties. However, there are also much simpler models based on uncorrelated stochastic processes of typically Lorentzian [10] of exponential [11] pulses which can explain such spectral characteristics as well. The main issue appears to be the difficulty in distinguishing exponential from powerlaw trends in spectra in the log-log scale over a wide range of frequencies.

Nevertheless, it has been shown that even such ballistic transport can lead to an effective diffusion constant which can be derived under assumptions of exponentially correlated, ballistic blobs escaping with a typical velocity and and correlation time [12]. This "diffusion limit" offers hope that simplified transport modeling based on diffusion as used many codes such as SOLPS-ITER [13] and EDGE2D [14] is still meaningful.

1.1.1 Scaling laws

The very basic arguments for τ_E scalings above could be refined by detailed and complex simulations of the whole plasma volume. However, at the time of the initial design of the ITER prototype reactor [15] even the largest available simulations typically were not able to capture the full scope of plasma physics throughout the whole plasma volume at sufficiently long time scales, mostly due to limitations in processing and memory capacities. Furthermore, the predictive power of the codes was limited. For these reasons the scientific community chose to develop empirical prediction formulas called "scaling laws".

Their name stems from the fact that many equations in plasma physics (especially magneto-hydrodynamics) are invariant to the change of (the combination of) certain scales. For this reason certain phenomena have been found to depend on non-dimensional parameters which may be invariant to a change of specific (e.g. spatial) scales, or at least limits the number and the kind of parameters that have an influence. This property of plasma physics is assumed to be behind the existence of very similar observations of various phenomena and behavior across a wide range of machine sizes and even different equilibrium configurations.

The discovery of formulas relating special parameters to quantities of interest then enables one to predict the values of sought quantities for larger future devices by appropriately "scaling up" the parameters. This approach is similar to the one used in wind tunnels where an appropriate ratio of wind speed and the size of a reduced airplane model can simulate hydrodynamic behavior at real, larger scales.

1.1.2 Confinement time scaling

One of the scaling laws sought in the past decades was that for the confinement time τ_E in order to determine the scale and other global parameters necessary for achieving τ_E sufficient for thermonuclear fusion power generation. On of the main drivers for the development of scaling laws was the design phase of the ITER tokamak. Powerlaw regression was used for this purpose as will be outlined in section 2.2. The regression was performed on datasets gathered from many tokamaks within the world-wide community and resulted in the notorious IPB98(y,2) [7] scaling for τ_E in the ELMy H-mode regime, the reference ITER enhanced confinement regime further described in section 1.2. This international effort continues to this day, adding data from new experiments to the database and refining previous analyses [16, 17]. A similar endeavor was also undertaken for stellarators which resulted in the ISS04 scaling [18] for τ_E in stellarators.

The IPB98(y,2) scaling predicts a trend of the form

$$\tau_{E,IPB98(y,2)} = 0.0562 I^{0.93} B^{0.15} P^{-0.69} n^{0.41} M^{0.19} R^{1.97} \epsilon^{0.58} \kappa_a^{0.78} \tag{1.1}$$

where the confinement time τ_E [s] increases with increasing plasma current

I [MA], magnetic field B [T], plasma density n [$10^{19}\mathrm{m}^{-3}$], main species mass M [m_u], major radius R [m], inverse aspect ratio ϵ and elongation κ_a. Only the input power P [MW] leads to a decrease of the confinement time, implying that the minimum possible power should be used in future reactors in order to prevent confinement degradation. This scaling law predicts $\tau_E \approx 4.9$ s for ITER. The strong, nearly quadratic scaling with the machine major radius $\sim R^2$ is consistent with the simplified random walk notion discussed in section 1.1.

Because the IPB98(y,2) scaling is considered the baseline scenario for future reactors such as ITER, confinement is generally compared to it as the $H_{98} = \tau_E/\tau_{E,98(y,2)}$ confinement improvement factor. A standard H-mode would achieve $H_{98} \sim 1$ and a standard L-mode only $H_{98} \sim 0.5$. This confinement improvement factor appears to be critical for the design of future reactors, because the fusion power gain Q is predicted to increase with the third power of H_{98} in [19]. Therefore, even a slight increase of H_{98} by optimizing the confinement regime could significantly reduce the input power required in future reactors. Such improvements can be achieved for instance by combining an H-mode regime with and internal transport barrier due to an optimized current profile or by discovering and optimizing other confinement regimes.

Recent progress in further analyzing the updated scaling datasets led to a the Kardaun 06 scaling [20] which attempts to take into account confinement time saturation at higher Greenwald fractions $\hat{n} := n_e/n_{GW}$ [21] as the density limit is approached. This is done by including a quadratic polynomial in the logarithmic scale $\alpha \log \hat{n} + \beta \log^2 \hat{n}$. This corresponds to a term $\hat{n}^{\alpha+\beta \log \hat{n}}$ which is hard to explain from a physics standpoint. This scaling is now sometimes used to define a H_{06} factor. Recent regression analysis using robust geodesic distance regression on an updated and carefully selected dataset [17] resulted in an updated scaling law which captures the confinement saturation with $\hat{n}$ for high, low and mixed proton number wall materials. Recently this scaling was further refined and compared with regression on dimensionless parameters [22]. This scaling demonstrated a clear increase of the confinement time with effective ion species mass. The better confinement in Deuterium with respect to Hydrogen has been seen already in early experiments [23] and along with other physics influenced by the ion mass is often referred to as the "isotope effect" [24].

1.2 L-H transition and H-mode

The H-mode (high confinement mode) was discovered nearly accidentally by applying large amount of heating power in the form of neutral beam injection (NBI) in the ASDEX tokamak [25], upon which the plasma suddenly and unexpectedly transitioned to a different regime, where the confinement time and confined energy doubled in comparison to the standard L-mode (low

confinement mode) before the transition[2]. This regime underwent rigorous and systematic research at the ASDEX and ASDEX Upgrade tokamaks [23] and over time was achieved also in other tokamaks across the world. Over time, it was established that the improved confinement is due to a transport barrier at the edge of the plasma (ETB - edge transport barrier) just inside the last closed flux surface (LCFS) in which the transport was reduced to neoclassical levels. This barrier was found to be comprised of a layer of sheared flows which shear turbulent structures apart, effectively stopping them from contributing to transport.

It was established that the sheared flow layer is maintained by the steep pressure gradient in the ETB through the radial force balance

$$E_r = \frac{\nabla_r p_i}{Z e n_i} + u_t B_p - u_p B_t \tag{1.2}$$

which relates the radial electric field E_r with the radial ion pressure p_i gradient and ion density n_i of Z-charged ions with the additional terms representing the cross product $u \times B$ of the poloidal and toroidal components of the ion fluid velocity u and the magnetic field B. The radially localized pressure gradient leads to a so-called "well' in the radial profile of E_r. This shape of the profile in turn leads through the associated poloidal $E \times B$ velocity to the shear layer. An example of such an E_r profile measured by several diagnostics in the JET tokamak is shown in Figure 1.1.

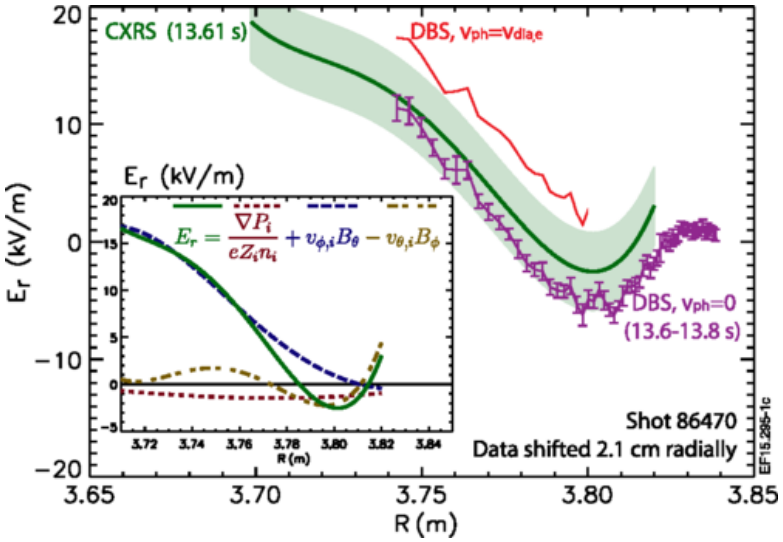

Figure 1.1: Example of the radial electric filed profile E_r measured by charge exchange recombination spectroscopy (CXRS) and Doppler back-scattering (DBS) reflectometry. Reproduced from [26] according to the CC BY 3.0 license.

The relatively narrow gradient region effectively shifts the pressure profile further inside upwards, as if placed on a "pedestal" as sketched in Figure 1.2 which has become the designation for this region and its properties. However,

[2]Up to this point standard L-mode scalings of τ_E predicted degradation with increasing heating power, offering little hope of achieving fusion power at a power plant level.

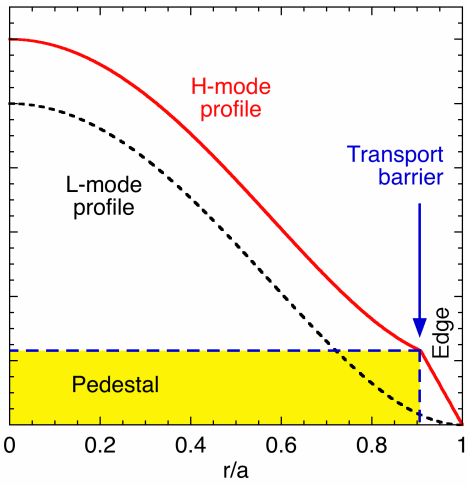

Figure 1.2: Sketch of a the pressure pedestal in the (normalized) radial profile formed in the H-mode with respect to L-mode by the edge transport barrier. Reproduced from [27].

to this day the origin and development of this sheared flow layer which then leads to the formation of the pedestal is not fully understood. Some of the most promising models which attempt to explain the observed the L-H transition are described in later sections.

In a wide range of global parameters the H-mode is accompanied by plasma instabilities called edge-localized modes (ELMs), which lead to periodic collapses of the ETB and the pedestal and releases of edge plasma (often tens of % of the stored thermal energy), presenting a danger of melting plasma facing components in future reactors such as DEMO [28] or ITER [29] if they are not suppressed or mitigated. The released edge plasma is typically observed to break up into filaments [30]. In earlier phenomenological works ELMs were categorized according to the change in their (quasi-periodic) frequency with increasing heating/loss power [31]. Type-III ELMs are typically found at marginal power and decrease their frequency, i.e typically start off as smaller, fast bursts after the L-H transition and gradually become less frequent and larger as the power increases. Type-I ELMs are comparatively even larger and increase their frequency with increasing power.

However, this categorization is not experimentally very easy, because it is often confounded by changes in other global parameters such as density which also affect the frequency. It is now widely accepted that ELMs are ideal magneto-hydrodynamic modes, driven unstable by pressure (ballooning modes), current (peeling modes) or their combination (peeling-ballooning modes) [32]. Due to these modes the pedestal (and thus the pressure gradient) can grow until it hits the ideal MHD stability limit and collapses, setting the maximum achievable pedestal parameters for a the given global conditions of a particular H-mode. The pedestal parameters have been most successfully predicted by the EPED stability code in a wide range of parameters for Type-I ELMs [33].

1.2.1 L-H power threshold scaling laws

Early empirical evidence pointed to the existence of a threshold in the loss power P_{loss} which when exceeded (i.e. for $P_{loss} > P_{LH}$ where P_{LH} is the threshold for the given plasma conditions) leads to a spontaneous transition to the H-mode regime. From an experimental standpoint the loss power is mostly controlled by the input heating power P_{heat}, because from the power balance $\mathrm{d}W/\mathrm{d}t = P_{heat} - P_{loss}$ rapid (compared to the τ_E time scale) changes in the heating power will be balanced by similar changes in the loss power, since the plasma energy W typically changes at slow time scales comparable with τ_E. Here the loss power includes both radiation losses and escaping thermal particles. Fast (i.e. supra-thermal) particle losses P_{Floss} are not included (i.e. are subtracted when their estimate is known), because such fast particles lost for instance due to charge exchange processes do not contribute towards the development of pressure gradients connected with the shearing flows. Radiation losses also do not contribute, however, the limited availability of a reliable radiation loss power P_{rad} estimate meant they were included in P_{loss} for this analysis. Some subsequent analyses such as [34] do subtract P_{rad} which is often called the power crossing the separatrix in particle losses P_{sep}.

One of the first attempt at creating a scaling law were done by Y. Martin in [35] based on a large ITPA database gathered from many tokamaks capable of achieving H-mode at that time. The resulting scaling law for the threshold loss power

$$P_{LH}[\mathrm{MW}] = 0.0488 n_e^{0.717} B^{0.803} S^{0.941} \tag{1.3}$$

which predicts a rising tendency with the density n $[10^{19} m^{-3}]$, magnetic field strength B [T] and plasma boundary surface S [m^2]. The nearly linear scaling with the surface suggests that the actual quantity of interest is the power normalized to the plasma surface, i.e. the average power flux P_{LH}/S. However, due to convenience for predictions towards future reactors, the absolute required power was investigated which is more relevant from an engineering standpoint. The scaling law predicts that the necessary heating power will generally increase for future reactors which are expected to achieve higher densities at high magnetic fields and generally larger plasma volume (hence also surface). For the standard ITER scenario $n \approx 5 \cdot 10^{19}\,\mathrm{m}^{-3}$ in deuterium this scaling predicts $P_{LH} \in (28, 96)$ MW, i.e. a necessary P_{heat} of at least ~ 50 MW, but with quite large uncertainty, which called for further refinement. Furthermore, this basic scaling does not capture various other factors influencing the threshold, such as the main ion species mass and charge and the existence of a non-monotonic density dependence observed in experiments covered in more detail in subsection 1.2.4 and subsection 1.2.2, respectively. This study by Martin focused exclusively the "high-density branch" of the power threshold dependence.

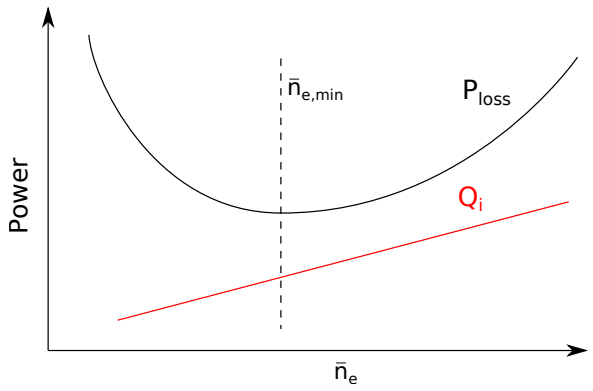

Figure 1.3: Sketch of a the typical loss power P_{loss} at the L-H transition versus the line-averaged electron density $\bar{n}_e$ and the ion heat flux Q_i component of P_{loss} as described in the methodology of [36].

1.2.2 Ion heat flux and density dependence

In many tokamaks a U-shaped non-monotonic dependence of P_{LH} on the line averaged electron density $\bar{n}_e$ was observed with a broad, yet distinct minimum [36, 37, 34, 38] as sketched in Figure 1.3. A more detailed study focusing on the power threshold with different heating systems and different plasma densities obtained evidence for the ion heat flux Q_i component of P_{loss} across the plasma boundary being the actual controlling parameter [36]. The study found that at low densities where the ion and electron heat fluxes are effectively decoupled the heating systems heating dominantly the ions such as NBI are more efficient. Conversely, systems dominantly heating the electrons such as electron cyclotron resonance heating (ECRH) required higher levels of heating power and thus resulted also in a higher total loss power, which lead to a "low-density branch" dependence with P_{LH} sharply increasing towards lower densities while Q_i depends on density linearly as sketched in Figure 1.3. This explanation is also consistent with observations in other devices where ECRH or purely ohmic heating was often used at lower densities, likely due to the unavailability of NBI or excessive NBI shine-through losses at such high densities.

The argument of the ion and electron heat channel coupling was also used to determine a scaling law for the density $n_{e,min}$ at which the power threshold minimum occurs. The scaling law was obtained by combining the L-mode scaling of τ_E and the empirical knowledge that at the density minimum the electron-to-ion energy transfer time is about 9 times larger than τ_E.

More detailed analysis of the profiles using transport codes and cross-machine comparison of ASDEX Upgrade and Alcator C-mod discharges resulted in a scaling law for the threshold ion heat flux required for the transition to occur [39]. A nearly linear dependence on the plasma boundary surface was found, indicating that the heat flux normalized to the surface is the controlling parameter. The interpretation in terms of the transport model is that the ion heat flux determines the ion pressure profile which in turn

through its gradient at the edge determines the mean sheared flow which then de-correlates turbulent structures and this forms a barrier for the turbulent transport.

There is also a different theory for the minimum of the threshold density dependence [40] which derives the existence of the minimum from the differences in the edge temperature behavior between conduction-limited and sheath-limited regimes in the SOL which are mostly determined by collisionality and in turn by the edge density. The theory is based in part on the idea that the L-H transition is determined by the equivalence of the parallel Alfvénic and perpendicular thermal transport time scales.

1.2.3 Divertor configuration and X-point dependence

Since the early experiments on the ASDEX tokamak [41] the divertor configuration has been considered nearly a necessity for entering the H-mode. This configuration diverts edge field lines by a toroidal coil with a co-plasma-current into a well controlled defined region of the first wall called the divertor which is typically actively pumped and contains elements designed for withstanding high heat loads at minimal material sputtering. The field lines are topologically separated into those closed within the chamber and open (i.e. closing beyond the chamber) by a manifold called the separatrix which includes the last closed flux surface (LCFS), the X-point singularity and divertor legs stemming from the X-point to the strike lines on the divertor. The plasma outside the LCFS is called the scrape-off layer (SOL).

The main benefit of the divertor configuration is the reduced contact of the main confined plasma with the first wall, offering better control of the plasma purity which turned out to have a significant impact on the L-H power threshold. For instance, higher impurity concentrations and/or desorption of particles from the first wall may increase radiation losses or provide additional particle sources, respectively. These may in turns hinder the development of the pedestal. Impurities such as carbon can also affect the electric field profile through their radial force balance. A nearly 30% reduction in the power threshold was observed when the ASDEX Upgrade tokamak moved [42] from a carbon first wall to a tungsten one and the JET tokamak to a Beryllium/Tungsten one [43].

The location of the X-point and divertor legs relative to the divertor are known to significantly affect the power threshold. For instance, in the JET tokamak different divertor leg configurations can change the threshold by several MW [43]. In the DIII-D tokamak a decrease of the X-point height above the divertor was seen to reduce P_{LH} [37]. EDGE2D-EIRENE simulations for such JET discharges [44] revealed that this behavior is likely because of differences in SOL conditions as shown in Figure 1.4. Due to the smoothness of the electric field and temperature profiles the SOL conditions were found to also affect conditions inside the LCFS. Therefore, studying the interplay between SOL and inner electric fields as the divertor configuration is changed might shed light on this behavior.

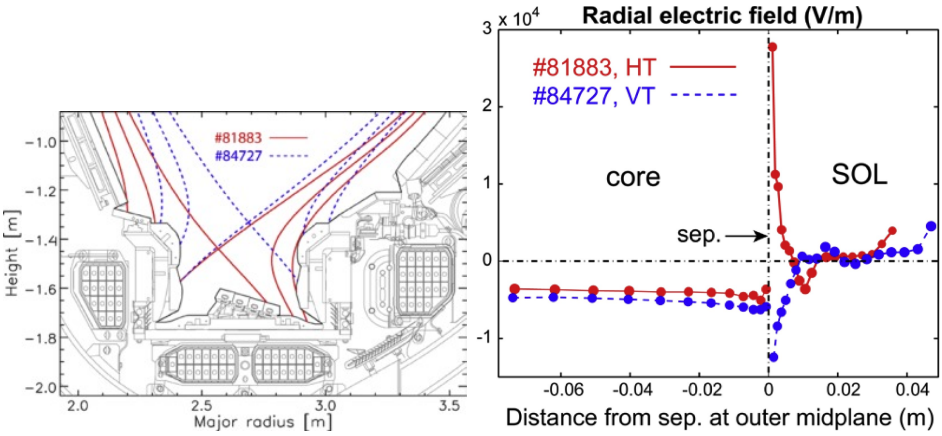

Figure 1.4: Comparison of the radial electric field E_r profiles in the Vertical and Horizontal Target configurations in JET simulated by EDGE2D-EIRENE. Reproduced from [44] according to the CC BY NC ND 4.0 license.

1.2.4 Isotope dependence

Among the various "isotopic effects" often observed is the impact of the main ion species on the L-H power threshold. It has been known since isotope studies in ASDEX that the P_{LH} is about double in Hydrogen in comparison to Deuterium [23, 24]. similar studies in JET with Tritium and Deuterium-Tritium mixtures confirmed a general inverse scaling $\sim 1/\bar{A}$ with the average ion mass number $\bar{A}$ [45]. Newer studies in ASDEX Upgrade reproduced the difference between Hydrogen And Deuterium, and furthermore showed that the density minimum $n_{e,min}$ and the ion heat flux is higher in Hydrogen as well [46].

The unfavorable increase of P_{LH} in Hydrogen posed an issue for the initial non-nuclear (i.e. without Deuterium) pre-fusion power operation of the ITER tokamak. Therefore, operation in Helium is planned as well [47], because for instance in ASDEX Upgrade P_{LH} was found to be nearly the same in Helium as in Deuterium [48] and only $\sim 40\%$ larger than in Deuterium in JET [49], though DIII-D reported possibly even larger difference [37]. Some uncertainty remains in terms of the non-linearity of the Hydrogen-Helium mixture ratio observed in JET [50], where only 10% "doping" of Helium in Hydrogen plasmas can strongly impact P_{LH}. However, this effect was not reproduced in a similar study in ASDEX Upgrade [51]. Resent experiments in Helium in JET found that the whole $P_{LH}(\bar{n}_e)$ dependence appears to shift to higher densities [52], though there the resulting slightly higher average P_{LH} is still comparable to the prediction by (1.3) at such densities.

1.2.5 Zonal flows and limit cycle oscillations

Another model for the formation of the edge shear flow layer is based on the coupling of turbulence and so called zonal flows (ZF). Zonal flows are toroidally and poloidally symmetric sheared flow bands/modes which are generated by

the transfer of momentum and energy [53] from the turbulence by the Reynolds stress [54]. A radial gradient in the radial-poloidal component of the Reynolds stress (RS) tensor $-\nabla_r \langle \tilde{v_r} \tilde{v_p} \rangle$ acts like negative viscosity and can accelerate the mean poloidal flow $\langle v_p \rangle$, where the Reynolds stress decomposition assumes a decomposition of the velocity field into its mean component $\langle v_i \rangle$ balanced by the pressure profile and the fluctuating component $\tilde{v_i}$ which represents turbulent structures. The following turbulence suppression criterion was formulated and verified in experiments [55]

$$P > \gamma_{\text{eff}} E_t \tag{1.4}$$

where $P = \langle \tilde{v_r} \tilde{v_p} \rangle \partial_p \langle \tilde{v_p} \rangle$ is the energy transfer rate from the turbulence into the mean flow [53] and γ_{eff} is an effective growth rate which includes both gradient drive and non-linear effects and E_t the turbulence energy. This criterion essentially states that for turbulence to be suppressed, energy must flow faster from turbulence into the mean flow than it is put into turbulence by driving and other mechanisms.

An often employed assumption is that the edge turbulence is dominantly electrostatic and the velocities are dominantly determined by the $E \times B$ drift. Therefore, it is necessary to measure electric fields in the edge plasma. In many tokamaks and in particular those of modest parameters such as COMPASS, electrostatic probes can be used for measuring the electric fields directly. However, Langmuir probes do not measure directly the plasma potential. Because they are also strongly affected by electron temperature, they measure a so-called floating potential V_{fl} offset from the true plasma potential ϕ by a factor proportional to the electron temperature T_e. Unfortunately, this can strongly influence the estimation of the Reynolds stress [56]. The ball-pen probe [57, 58], an alternative design, is affected by the electron temperature much less in comparison.

One of the most promising models [59, 60] of the L-H transition predicts that as the pressure gradient increases due to increased heating, turbulent fluctuations intensity rises due to the free energy in the pressure gradient, which through enhanced transport limits the pressure gradient from growing further. The strong turbulent state generates ZF which act as harmless energy sink and de-correlate the turbulent structures, reducing the transport and allowing the pressure gradient to grow. But due to collisional damping and lack of turbulent energy source the ZF dissipate and turbulence can grow again. Due to this predator-prey-like coupling between turbulence and sheared zonal flows the system process periodically transitions between a state of high and quenched turbulent transport. This phenomena is called limit cycle oscillations (LCO) and is characterized by the ZF being delayed by a $\pi/2$ phase shift behind the turbulence intensity. On the background of LCO the pressure gradient can gradually grow as power is increased until the mean sheared flow balanced by the pressure gradient is sufficiently strong to de-correlate turbulent structures on its own.

Since the generation of zonal flows is considered to be one of the leading candidates for quenching turbulence in general and possibly during the L-

H transition as well, this LCO phenomena offers a promising opportunity to further study the dynamics of the L-H transition in greater detail, and therefore, has been studied in many tokamaks across the world [61, 62, 63, 64, 65, 66].

However, the characteristics of the observed LCO differ between tokamaks. Some experiments found that turbulence suppression by flow generation appears strong enough to trigger a transition into the H-mode [67]. Others do not [68] and rather observe a behavior closer to type-III edge localized modes (ELMs) where the pressure gradient quasi-periodically relaxes upon reaching a critical threshold [69].

1.2.6 Separatrix operational space

Very recently a new theory of the L-H transition boundary based on the energy transfer from turbulence to mean flows was developed and compared with separatrix Thomson scattering profiles in the ASDEX Upgrade tokamak [70]. The theory further proposes also other boundaries in the operational space for the density limit and ideal ballooning limit. This model was motivated by the re-examination of past work which focused on the characterization of interchange [71] and drift-Alfvén wave turbulence [72]. The former pointed out the importance of the interchange growth rate and spatial scale for the L-mode density limit, while the latter also showed the importance of the parallel Alfvénic dynamics for the turbulence structure.

However, in the past these theories were apparently discarded based on the comparison with T_e, n_e data close to the pedestal top [73]. The new analysis was based on values evaluated close to the separatrix which was estimated using a conduction-limited-simplified two-point model balance. The analysis showed the importance of the transition between drift-Alfvén wave and interchange-dominated turbulence regimes for the scaling of the pressure gradient fall-off/length scales [74]. The scaling was augmented by regression of the turbulence parameter $\alpha_t = 3 \cdot 10^{-18} R q^2 n Z_{eff} T^{-2}$ representing normalized collisionality which characterizes the transition between the turbulence regimes. The new theory [70] built further on this work to derive the L-H transition boundary in the T_e, n_e space and derive scalings of the power threshold. However, the theory and analysis was limited only to rather pure Deuterium discharges and made use of the pressure gradient length $\lambda_{p_e} = -p_e \partial_r p_e$ scaling so far verified only for ASDEX Upgrade [74]

$$\lambda_{p_e}(m) = 1.2(1 + 3.6\alpha_t^1.9)\rho_{s,pol} \tag{1.5}$$

with the gyroradius calculated with the averaged poloidal magnetic field $\rho_{s,pol} = \sqrt{m_i T_e}/eB_p$. The assumption of $L_\perp = \lambda_{p_e}$ for the DALF model described in section 2.3 led to the development of a boundary described by the relation below only in terms of T_e, n_e and enabled the estimation of the corresponding loss power without radiation crossing the separatrix. The following condition for the sustainment of H-mode is essentially an approximation of (1.4)

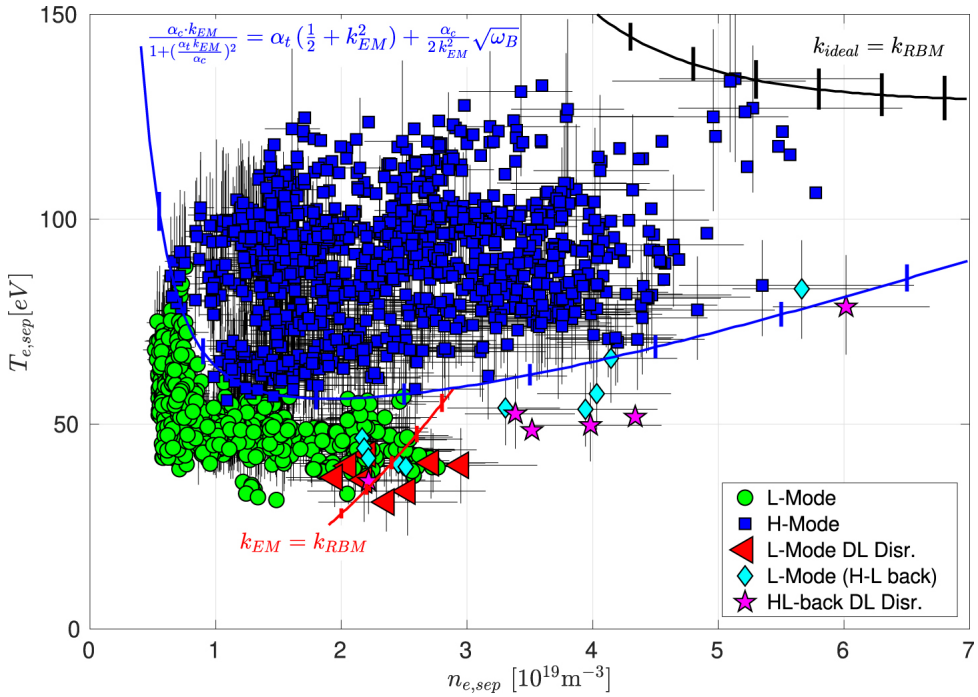

Figure 1.5: Comparison of the H-mode turbulence suppression (blue line) criterion according to (1.6), L-mode density limit (red line) and ideal ballooning mode limit (black line with the experimental separatrix electron density n_e and temperature T_e in ASDEX Upgrade Deuterium discharges. Reproduced from [70] according to the CC BY 3.0 license.

$$\frac{\alpha_\mathrm{c} k_\mathrm{EM}}{1+(\frac{\alpha_\mathrm{t}}{\alpha_\mathrm{c}} k_\mathrm{EM})^2} > \alpha_\mathrm{t}\left(\frac{1}{2} + k_\mathrm{EM}^2\right) + \frac{1}{2}\frac{\alpha_\mathrm{c}}{k_\mathrm{EM}^2}\sqrt{\omega_\mathrm{B}} > 0 \tag{1.6}$$

where on the left the energy transfer rate from turbulence to the mean flow P from (1.4) is approximated by the a typical wavenumber k_EM of the drift-Alfvén wave turbulence which is proportional to pressure and a critical ideal ballooning limit α_c set by shaping. The denominator approximates the reduced efficiency of the transfer at low adiabacity. The terms on the right approximate the various sources of turbulent energy coming from the kinetic, electron and ion channels. The α_t parameter describes the transition from drift-Alfvén wave to interchange-dominated turbulence. The ω_B parameter is a normalized curvature radius and represents the interchange growth rate. This formula already assumes the local equivalence of the ion and electron temperature profiles (including gradient fall-off lengths) which is apparently the case for most of the discharges in the paper where such measurements are available. Very good agreement between the threshold predicted by this formula and experimental separatrix data measured in ASDEX Upgrade is shown in Figure 1.5.

It remains to be seen how this theory compares with the ion heat flux theory described in subsection 1.2.2 or whether one theory explains the other. The non-monotonic dependence of P_{loss} as sketched in Figure 1.3 is qualitatively

similar to the dependence of T_e in Figure 1.5, though the correspondence is not direct, because in addition to the power balance in the electron channel determining T_e the ion heat flux has to be included as well. This has been estimated using the pressure gradient length scaling (1.5) and neoclassical considerations as explained in [70]. Further studies on the role of electrons and ions and their temperature profiles in such a model is planned for the next AUG campaign in 2021-2022. In order to be fully predictive for future reactors, this model will require the development of a formula or scaling like (1.5) of the electron and ion pressure gradient length scales that will work even for other tokamaks.

1.3 Type-I ELM-free confinement regimes

While the H-mode is the most widely explored enhanced confinement regime, other possibly reactor-relevant regimes have been discovered in recent decades. The main advantage of these modes is the absence of ELM crashes, which otherwise present a significant threat for the plasma-facing components of the device. These "natural no-ELM" regimes typically have some mode (less dangerous than ELMs) present which quasi-periodically enhances edge transport preventing density and impurity accumulation in the core plasma and hitting ideal MHD limits.

These regimes are achieved "naturally" in specific plasma parameters and discharge settings, in contrast to scenarios with the application of resonant magnetic perturbations (RMP) generated by external coils which can also lead to ELM mitigation or suppression [75]. Using RMP is still considered to be one of the strategies to limit the harmful impact of ELMs on the future divertor in ITER [76].

One such possibly reactor-relevant regime is the I-mode regime [77, 78, 79] originally studied in the Alcator C-mod tokamak. The main difference with respect to the H-mode regime is that it has a pedestal only in temperature while particle confinement and the density profile remains at L-mode parameters, preventing impurity and density accumulation. The typical relative difference in profile shapes is shown in Figure 1.6.

The relatively low particle confinement in I-mode is thought to be due to the presence of a weakly-coherent mode (WCM) spanning a broad spectrum of fluctuation frequencies (typically 50-200 kHz at ASDEX Upgrade). The transition from L-mode to I-mode (L-I transition) is typically found at P_{loss} below that of the L-H transition. For the L-I transition to occur, the presence of the geodesic acoustic mode (GAM) and its interaction with the WCM appear to be required in some devices. The GAM is a type of an oscillating ZF with a poloidally asymmetric density modulation and it is the non-linear energy transfer from turbulence to the GAM that appears to be key to the L-I transition [80].

The power threshold for entering the I-mode was found to scale as $P_{LI} \propto B^{0.2}nS$ and in comparison with (1.3) the operational window to enter the I-mode without entering the H-mode first was found to "open up" only at

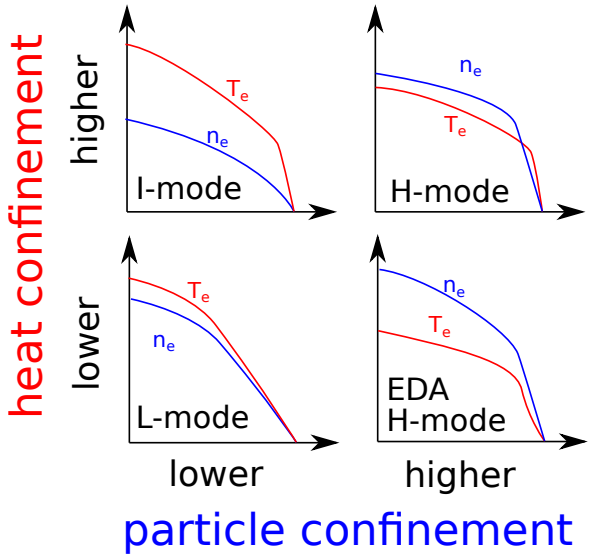

Figure 1.6: "Magic quadrant"-style sketch of the various electron density n_e and temperature T_e radial profile shapes in various enhanced confinement regimes. The sketched shapes represent profiles normalized to a common total pressure in order to highlight the relative differences and the presence or absence of a pedestal. In absolute terms such profiles may be reached in very different discharge conditions (e.g. the L-mode vs H-mode profiles) or their difference may not be so large (e.g. the T_e pedestal in H-mode, EDA H-mode and I-mode may not be very different).

high magnetic fields and/or when the ion ∇B drift is oriented away from the X-point where P_{LH} is usually doubled [78]. I-modes were obtained in Alcator C-mod even with the "standard" ion ∇B drift orientation towards the active X-point, though they were less robust regimes due to the close proximity to the transition to H-mode [81]. Later the I-mode regime was also obtained in ASDEX Upgrade [79]. While the I-mode does not feature large Type-I ELM crashes, it can feature intermittent bursts of expelled plasma carrying significant heat loads, though several time smaller than for Type-I ELMs. These pressure relaxation events (PREs) are typically observed close to the transition to H-mode [82].

A recent theory based on gyro-fluid simulations proposed that the I-mode regime is accessible under specific conditions just inside the separatrix [83]. One of the ingredients is that ion-temperature gradient (ITG) mode drive must be reduced, therefore, the ion temperature gradient must be smaller than the electron temperature gradient. At the same time, the ion temperature needs to be larger than the electron temperature. This was proposed to be achievable at low collisionality where the ion and electron temperatures are decoupled. However, this argument was based only on simulation results featured in [84]. This leads to the broadband turbulence being dominated mainly by electron modes. Furthermore, the regime is accessed at higher electron pressure which causes large-scale modes to be scattered by magnetic fluctuations. Small-scale modes are also suppressed by finite-Larmor-radius

effects. the resulting "middle ground" of the remaining broadband turbulence spectra is then observed as the WCM. In this theory the GAM was not found to be needed for the access to this regime.

Another candidate regime is the quiescent H-mode (QH-mode) [85] studied DIII-D where the pedestal is held at a stable gradient by periodic edge instabilities called edge harmonic oscillations (EHO). The name stems from their typical signature on magnetic (and other) spectra, where they typically have several clear higher harmonics due to their sharp, crash-like temporal characteristics. This regime requires high values of edge velocity shear and low densities, making it attainable only in a limited range of operational parameters. Current research focuses on expanding this range towards future reactors [86]. The main challenge of current research in ASDEX Upgrade is to obtain a stationary QH-mode in the full-metal first wall which as of writing this thesis has not been successful. In comparison clear and stationary QH-mode regimes were obtained in ASDEX Upgrade with the previous Carbon wall.

Last but not least, the enhanced D-alpha (EDA) H-mode regime [87] originally discovered in Alcator C-mod has a confinement time similar to that of H-mode, but a markedly higher level of D-alpha emission (hence the name). In comparison to an ELMy H-mode the density pedestal is typically even higher. The mode thought to be responsible for regulating the transport is the so-called quasi-coherent mode (QCM) at the plasma edge. Studies on Alcator C-Mod showed that the QCM is located in the close vicinity of the LCFS and has a typical frequency $\sim$100 kHz and is likely caused by electromagnetic electron drift-waves with interchange contributions [88]. Recently a similar mode was discovered in ASDEX Upgrade electron cyclotron resonance heating (ECRH) discharges [89].

More recently, this group of regimes was further redefined and renamed to "Type-I ELM-free" regimes to signify that such regimes do not feature large ELM crashes which would be far beyond the capabilities of planned mitigation strategies in future reactors. This enabled the inclusion of the so-called quasi-continuous exhaust regime (QCE) [90], previously named "small ELMs" [91]. Because these "type-I ELM-free‘ regimes still feature crash-like bursts of various kinds and associated heat fluxes, successful and stable detachment and a radiating edge is considered a necessary qualification for any such regime to be considered reactor relevant. Therefore, in addition to extending the operational parameter space of such regimes towards reactor-relevant values as outlined in [86] the compatibility of such regimes with seeding is an active area of research. Previous attempts at detachment of the I-mode in Alcator C-mod suggested this may not be entirely straight-forward [92]. The EDA-like regime in as well as RMP-induced ELM-free H-mode in ASDEX Upgrade generally shows compatibility with Argon seeding, though the scenarios require further development to reactor-relevant parameters [93].

Chapter 2

Experimental and theoretical analysis methods

This chapter describes the experimental and theoretical background used to study the phenomena described in chapter 1 which led to the results in chapter 3.

2.1 Tokamaks

All the experimental data were obtained in experiments performed in several tokamaks of varying sizes, magnetic fields and heating methods. In the following their properties are briefly described and compared from the perspective relevant to the thesis. Their important global parameters relevant to the experiments used in this thesis are summarized in Table 2.1.

The majority of the work done in the scope of this thesis was performed in the COMPASS tokamak [94]. While it is not officially included in the "medium-sized tokamak" (MST) EUROfusion work package, it comparable in size and other parameters with the TCV tokamak [95] included in the MST list. It was originally constructed in the United Kingdom and named COMPASS-D where it was operated mainly with electron cyclotron resonance heating (ECRH) as the primary auxiliary heating method [96]. After being transferred to the Czech Academy of Sciences [97] it was renamed to COMPASS to differentiate the new facility. From then on it was operated mainly with neutral beam injection (NBI) auxiliary heating instead of ECRH. However, it is possible to access the H-mode even only with pure ohmic heating. One of the most developed and for this thesis essential diagnostics is the Thomson Scattering (TS) diagnostic. It provides calibrated electron temperature T_e and density n_e profiles with a spatial resolution of below 4 mm and a laser repetition rate of up to 120 Hz after a recent upgrade [98]. The modest temperatures typically achieved in the edge plasma make it possible to measure with electrostatic probes even slightly inside the separatrix. An in-house developed ball-pen probe technique [99, 57, 58] makes it possible to estimate T_e in combination with a standard Langmuir probe and generally measures a floating potential quite close to the true electrostatic plasma potential. Finally. the COMPASS tokamak is equipped with a wide array of magnetic pick-up coils which

	JET	ASDEX Upgrade	COMPASS	Globus-M
R [m]	2.96	1.65	0.56	0.4
B_t [T]	1.5-2.5	1.4-3	1.15	0.5
q_{95}	3.6-5	3.8-8.6	2.7-3.5	2.3
working gas	H, D, T, He	H, D, He	D,	D
auxiliary heating	ICRH, NBI	NBI, ECRH	none	NBI

Table 2.1: Summary of global parameters of the experiments performed in the tokamaks and/or analyzed in the scope of this thesis. Note that the full capabilities of the tokamaks extend further than those reported in the table which only summarizes a subset of experiments.

enable the spectral analysis. All the experiments described in this thesis were preformed in Deuterium as a working gas, though experimental campaigns in Hydrogen and Helium were also performed in the past.

The ASDEX Upgrade (AUG) tokamak [100] is nearly 3 times larger than COMPASS in linear dimensions and routinely operates with both ECRH and NBI auxiliary heating, which is typically necessary for H-mode access. Ion cyclotron resonance heating (ICRH) heating is also available, but was not used in experiments relevant to this thesis. The possibility of reaching high magnetic fields up to 3 T also in the unfavorable ∇B drift direction makes it possible to access the I-mode regime with auxiliary heating as well. There are many diagnostic systems actively maintained and operated. From those, of greatest importance to the work in this thesis are the TS systems which have independent core and edge systems and the poloidal correlation reflectometry for edge turbulence characterization [101]. Similarly to COMPASS, it can use Hydrogen, Deuterium or Helium as a working gas.

The Join European torus (JET) [102] is the largest operating tokamak in existence at the time of this thesis being written. It is about double the size of ASDEX Upgrade in linear dimensions, but its magnetic field capabilities aren't much different. It most commonly uses NBI and ICRH as auxiliary heating methods. Another big difference with respect to all the other tokamaks currently operating is that in addition to Hydrogen, Deuterium and Helium it can also use Tritium as a working gas. This capability makes it very useful for isotope effect studies as well as studying and demonstrating actual D-T fusion-relevant physics.

On the opposite side of the size spectrum is the smallest device contributing data to this thesis: Globus-M [103]. It is one of the smallest tokamaks capable of accessing H-mode with NBI heating. It also has a high aspect ratio which places it into family of spherical tokamaks. Its magnetic field capabilities $B_t < 0.4$ T are rather modest even in comparison to COMPASS, though it is being upgraded to 1 T capability as the Globus-M2 project. Experiments are routinely performed in Deuterium as the working gas. The main diagnostics providing data for this thesis is the Thomson Scattering system as well as magnetic pick up coils.

2.2 Powerlaw scaling regression analysis

The properties of scaling laws described in subsection 1.1.1 do not directly prescribe the form of these scaling laws on their own. For practical and partly physical reasons powerlaw formulas $f = Cn^{\alpha}B^{\beta}R^{\gamma}a^{\delta}\ldots$ are typically chosen as the form of scaling laws. Here f is the quantity to be extrapolated, C is a proportionality constant (often taking care of a mismatch in physical dimensions and/or scales) and n could be the plasma density, B the toroidal magnetic field strength, R and a the major and minor tokamak torus radii, respectively. The free parameters that are fitted are $\alpha, \beta\, \gamma, \delta, \ldots$.

The physical motivation behind this choice is that with such a form one can easily use dimensional and scale invariance arguments to reduce the number of parameters or at least the degrees of freedom in the formula exponents. One can also use dimensionless quantities such as the kinetic to magnetic poloidal field pressures β_p, ion gyro radius normalized to the minor radius $\rho_* = \rho_i/a$ instead of engineering parameters such as R, a, B in order to capture the scale invariance implicitly [17].

This was realized early on by B. Kadomtsev [104] which led to the naming "Kadomtsev constraints". Conversely, one can also test the predicted constraints in experiments, verifying the underlying theories. Another argument for using powerlaw formulas is that many of the scaling formulas derived from basic theory are of that form and this is further supported by empirically observed trends which are often stronger than linear.

From a more practical perspective powerlaw formulas are (seemingly) convenient for the application of fitting routines to estimate the (perhaps partially) unknown exponents. The common approach used in many scaling studies is to take the logarithm of the whole formula (and the measured quantities), transforming it into a simple linear problem $\log f = \log C + \alpha \log n + \beta \log B + \gamma \log R + \delta \log a \ldots$. This logarithmic transformation is enabled by the fact that most of the global parameters (or at least their magnitudes) to be extrapolated to future devices are typically strictly positive.

However, this transformation comes at the price of changing the meaning of the uncertainties associated with the measured quantities and residual errors between the fit and measured values. Standard fitting routines based on minimizing the sum of residuals squared (known as least squares fitting) assume a probabilistic model where uncertainties in the exogenous (independent) variables and the errors/residuals in the endogenous/dependent/predicted quantities are all Normal-distributed (Gaussian). Before the logarithmic transformation the uncertainties may indeed represent Normal distributions because they are typically a sum of several intermediate calculations or measurements with (mostly) independent, typically close to Gaussian errors. However, after the logarithmic transformation the distributions would be Lognormal which is at odds with the Normal assumptions of typically applied least squares fitting routines. Their application then minimizes the following objective function $\sum \ln^2(f_{meas}/f_{pred})$ which effectively minimizes relative errors (multiplicative factor differences) instead of absolute errors.

This inconsistency may lead to biased estimates both of the parameters and their uncertainties as reported in [105].

A solution of this particular issue can be to use Generalized Linear Models (GLM) [106] which permit the usage of several likelihoods (including Gaussian) while using a so-called link function specific to the problem. Therefore, one can sill use the linear model for the predictor variables in the logarithmic domain as before, but using a logarithmic link function and Gaussian likelihood the problem minimizes the actual sum of squared (absolute) errors. This can be expressed as

$$\begin{aligned} f &\sim \mathcal{N}(\mu, \sigma^2) \\ g(\mu) = \ln(\mu) &= \log C + \alpha \log n + \beta \log B + \gamma \log R + \delta \log a \dots \end{aligned} \tag{2.1}$$

with the link function $g = \ln$ relating the predicted mean μ of the measurement f observation Gaussian likelihood $\mathcal{N}(\mu, \sigma^2)$ with variance σ^2 (estimated or taken from measurement uncertainties).

Since such models are a very well established and standard statistical technique, many tried and tested software implementations with accompanying diagnostics and statistical test routines exist in several programming languages. The author chose the implementation in the Python Statsmodels library [107] which uses the iteratively reweighed least squares fitting algorithm. To the knowledge of the author GLMs have not been used before in the fusion community for scaling regression, even though it requires only very little extra effort with respect to the ordinary log-linear regression and solving some of its issues.

Recently there have been developments in the area of scaling regression to address some of these inadequacies and more robust regression methods based on geodesic distances between distributions have been applied to previously analyzed data [108, 17]. Such more advanced approaches are gradually gaining traction in the community, but the older methods are still in use, partly because there is now easily accessible implementation of these more advanced methods.

There have also been attempts to use non-powerlaw forms to develop scaling laws which can explain non-monotonic behaviors and saturation effects, for instance general polynomial regression and other machine-learning methods [109]. Another issue is selecting the quantities to use in the (powerlaw) regressions. This issue has been investigated by employing genetic programming to dynamically create and evaluate symbolic expressions [110].

More complicated trends with saturation effects and/or transitions or bifurcations in behavior could be also explained by applying powerlaw formulas to quantities separately for the ion and electron channel and using their sum in later calculations as suggested in [111]. For instance, the ion and electron heat flux conductivity χ_i and χ_e may have different powerlaw behaviors, but the total heat conductivity $\chi = \chi_i + \chi_e$ may play a role in determining other quantities. Other quantities such as the thermal energy, loss power and confinement time are separable in a similar manner. Through such

constructions more sophisticated rational functions of powerlaw formulas may be derived. These complicated formulas also have the capacity to describe a bifurcation in the trends, opening up the possibility of using such formulas for capturing confinement enhancement during transitions into enhanced confinement regimes.

2.2.1 Causal graphical models

In recent decades the field of applied statistics has rejuvenated the topic of causality, led by J. Pearl [112]. The mantra "correlation does not imply causation" has been transformed into "no correlation without causation" and focus was shifted to the determination when one can infer actual causal relationships, direct and indirect effects, etc. The issues of spurious correlations between quantities due to their common cause(s) has been formalized and methods for detecting and averting the effect of such confounding (common cause) variables have been developed, namely the so called back-door and front-door adjustment formulas using conditioning on specific variables. The origin of spurious correlations due to conditioning on a common effect was also formalized.

The framework used for this formalization is the language of causal graphical models (CGM) which encode (conditional) independence relationships into easy-to-read graphs with nodes representing measured quantities and arrows (if oriented) representing causal effect directions, i.e. dependencies. When the functional form of the causal dependencies is known, a structural model can be formed and counterfactual (what-if questions) can be answered, leading to the separation of direct and indirect effects. Algorithms for automatic identification of graphical models from data and conditions necessary for their use have also been developed [113].

To the knowledge of the author causal models have not been routinely used in the statistical works applied to fusion data and scalings to this date. This methodology may offer enhancements to future analyses by identifying root causes which could reduce and the number of or select the variables used in regressions. At the very least, the display of the assumed CGM can succinctly yet clearly summarize the assumed relationships and dependencies or lack thereof in a given analysis. The use of graphical models could also explain some spurious correlations either by the existence of confounding quantities or experimental conditioning on some quantities. For instance, many experiments hold the edge safety factor q_{95} and/or the Greenwald fraction [21] n_e/n_{GW} at a given value while other parameters are changed.

A simple CGM representing some assumptions underlying power threshold P analyses in chapter 3 is shown in Figure 2.1. Typically experiments are performed in a constrained range of q_{95} in order to stay clear of disruptive instabilities and yet often attempt to minimize q_{95} to claim relevance to future reactors or maximize I_p to obtain good confinement as indicated by (1.1). Since $q_{95} \propto B/I_p$ is dominantly determined by the magnetic field B and the plasma current I_p, it represents a so-called"collider" quantity between these root causes. If one conditions (regresses) on such a collider, the otherwise

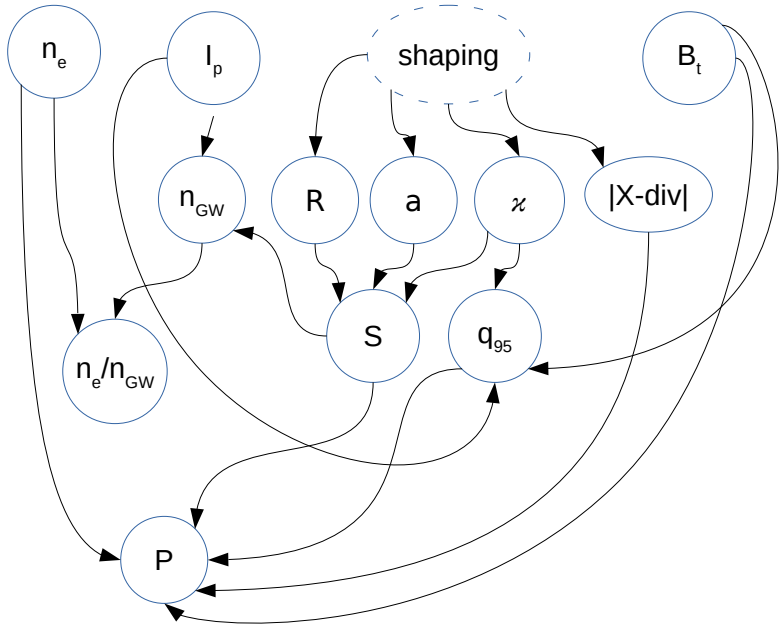

Figure 2.1: Causal graphical model representing assumed conditional (in)dependencies between quantities of interest in the analyses of various transition power thresholds in chapter 3. The arrows represent assumed direct effects between the quantities power threshold P, root causes the toroidal magnetic field strength B_t, plasma current I_p, plasma shaping (dashed-unobserved as single quantity) and (line-averaged electron) density n_e. Intermediary quantities are the Greenwald density n_{GW} and its fraction relative to the electron density n_e/n_{GW} and the various quantities set by shaping such as elongation κ, the distance of the X-point above the divertor $|\mathrm{X}-\mathrm{div}|$, LCFS surface area S and the plasma major and minor radii a and R, respectively.

independent root causes may appear correlated and such a co-linearity may reduce the predictive power of any regression results. Furthermore, simple B and I_p scans cannot directly distinguish the impact of q_{95}, B, I_p on physical phenomena. The q_{95} dependence could be scanned at constant B, I_p by elongation κ set by shaping since $q_{95} \propto (1+\kappa^2)$, provided the impact of the resulting change of the total LCFS boundary area S can be assumed to have no direct impact on P itself. n P could be compensated by different shaping, e.g. by adjusting the major or minor plasma radii R and a, respectively. Of course, this can only work if R and a do not have any other direct or indirect effects on P.

A similar case can be made for the Greenwald fraction n_e/n_{GW} determined by the electron density n_e and the plasma current I_p through $n_{GW} = I_p/\pi S_p$ with the poloidal cross-section surface area S_p (correlated with S). Since most experiments aim at good confinement and stay clear of the degradation with increased n_e/n_{GW}, they effectively constrain n_e/n_{GW} which creates a spurious correlation between I_p and n_e. Since S_p also depends on κ, the requirement of holding n_e/n_{GW} the while avoiding a spurious correlation of I_p and n_e could be again partly mitigating by compensations in shaping.

Graphical models may guide the way in selecting the right quantities to condition on or constrain in the experiment and/or the subsequent analysis in order to prevent or mitigate correlations. In combination with explicit formulas for various quantities derived from theory or previous scaling studies, structural causal models can be developed from a CGM for the identification of direct effects which could in turn point towards specific physical mechanisms. For instance, assuming the scaling (1.3) holds, the dependence of P on n_e, B_t and S for L-H transitions in the high density branch could be exploited by constructing "counter-factual" estimates of P at the given parameters and normalizing the observed P and thereby focusing only on the remaining direct causes leading to P.

2.3 DALF model of edge plasma turbulence

The drift-Alfvén wave turbulence model DALF [114, 115, 116] developed by B. Scott was used to study several aspects of turbulence in the edge plasma layer of tokamaks [72]. It is a simplified fluid model based on Braginski equations with variables chosen to describe the drift-Alfvén and interchange turbulence. It uses a simplified tokamak geometry with a circular cross-section, and therefore, cannot faithfully describe some physical mechanisms dependent on plasma shaping such as the impact of the X-point. However, the chosen normalization constants depend on a safety factor q through the parallel field line length estimate $\sim qR$. Therefore, the model can be still applied to non-circular plasmas when parallel dynamics are dominant if the edge magnetic equilibrium reconstruction safety factor q_{95} is used to give an accurate estimate of the actual field-line length.

The DALF model as used in the thesis and written in [117] consists of 4 equations for the vorticity Ω, electron pressure p_e, parallel current $J_\parallel$ and parallel ion flow $u_\parallel$

$$\frac{\mathrm{d}\tilde{\Omega}}{\mathrm{d}t} = B\nabla_\parallel \frac{\tilde{J}_\parallel}{B} - (1+\tau_i)\mathcal{K}(\tilde{p}_e) \tag{2.2}$$

$$\frac{\mathrm{d}\tilde{p}_e}{\mathrm{d}t} + \tilde{v}_E \nabla p_e = B\nabla_\parallel \frac{\tilde{J}_\parallel - \tilde{u}_\parallel}{B} + \mathcal{K}(\tilde{\phi} - \tilde{p}_e) \tag{2.3}$$

$$\hat{\beta}\frac{\partial \tilde{A}_\parallel}{\partial t} + \hat{\mu}\frac{\mathrm{d}\tilde{J}_\parallel}{\mathrm{d}t} = \nabla_\parallel \left(p_e + \tilde{p}_e - \tilde{\phi}\right) - C\tilde{J}_\parallel \tag{2.4}$$

$$\hat{\epsilon}\frac{\mathrm{d}\tilde{u}_\parallel}{\mathrm{d}t} = -(1+\tau_i)\nabla_\parallel \left(p_e + \tilde{p}_e\right) + \mu_\parallel \nabla_\parallel^2 \tilde{u}_\parallel \tag{2.5}$$

with the normalized magnetic field strength $B = 1$. The model uses shear-slab Hamada coordinates (x, y, s) representing in order the radial, bi-normal (close to poloidal) and ballooning angle (equivalent to the straight-field-line angle θ^* for analytical purposes) coordinates. Magnetic shear is included implicitly in the numeric scheme. The ion pressure is held fixed relative to the reference electron pressure by $\tau_i = T_i/T_e$, producing a "scaled-isothermal"

model. The vorticity is defined as $\Omega = (1/B^2)\nabla_\perp^2 W$ with the so-called total ion flow stream function $W = \phi + \tau_i p_e$. The spatial derivatives of W give the $E \times B$ (from the electrostatic potential ϕ) and the diamagnetic (from the ion pressure gradient) drift velocities. The total time derivative $\mathrm{d}/\mathrm{d}t = \partial/\partial t + v_E \nabla$ includes the $E \times B$ velocity v_E advection non-linearity. The parallel electron flow is decomposed into the parallel current and ion flow $v_\parallel = u_\parallel - J_\parallel$. The simplified curvature operator $\mathcal{K} = \omega_\mathrm{B}(\sin s\partial_x + \cos s\partial_y)$ is composed of the geodesic and normal components, respectively. Parallel scales are normalized to a field line connection length scale qR with the reference safety factor q an major radius R, which normalized a parallel wavenumber $k_\parallel = 2\pi/L_\parallel$ of a rational $n = 1$ mode with $L_\parallel = 2\pi qR$ to 1. Perpendicular scales are normalized to the hybrid gyroradius $\rho_s = \sqrt{T_e m_i}/eB$ with reference values of the electron temperature T_e, ion mass m_i and on-axis magnetic field strength B. Additionally, all fluctuating quantities marked with a tilde are normalized by a smallness parameter $\delta = \rho_s/L_\perp$ where $L_\perp$ is a reference background profile gradient length typically chosen a $L_\perp = -p_e/\nabla_x p_e$.

The following dimensionless parameters scale the impact of the various terms in the equations above.

$$\hat{\epsilon} = \left(\frac{c_s/L_\perp}{c_s/qR}\right)^2 \quad \hat{\beta} = \left(\frac{c_s/L_\perp}{v_A/qR}\right)^2 \quad \hat{\mu} = \left(\frac{c_s/L_\perp}{v_e/qR}\right)^2 \quad C = 0.51\hat{\mu}\frac{L_\perp}{c_s}\nu_{ei} \tag{2.6}$$

which represent in order the squared ratio of the perpendicular and parallel sound transit frequencies, the squared ratio of the perpendicular sound and parallel Alfvén transit frequencies, the squared ratio of the perpendicular sound and parallel thermal electron transit frequencies and the normalized electron-ion collision frequency ν_{ei} representing current resistivity. The curvature operator is scaled by a normalized curvature radius $\omega_\mathrm{B} = 2L_\perp/R$. The cold-ion sound speed $c_s = \sqrt{T_e/m_i}$ is used in the parameters, warm-ion effects are included by $(1 + \tau_i)$ factors. The definitions of the Alfvén and thermal electron velocities are $v_A = B\sqrt{\mu_0 n_e m_i}$ and $v_e = \sqrt{T_e/m_e}$.

There are also related extended models known as DALFTE [115] which separates the electron pressure into separate density and temperature variables. The DALFTI model [115] then further separates the ion from the electron temperature. Nearly all of the DALF-related articles by B. Scott focused on singly-charged ion with an ion charge number $Z = 1$. The only known exception is the section 16.2 in [24] where the cold ion sound speed $c_s = \sqrt{ZT_e/m_i}$ is used in DALF-like transport considerations.

The cleverly chosen variables and scaling constants in DALF make the model amenable to analytic treatment. For instance, the model can be used to derive the frequency of a Geodesic Acoustic Mode (GAM) as in [118] based on simple, linear sideband balance. A similar argument was used to derive an initial scaling for limit cycle oscillations near the L-H transition [117]. More recently, the DALF model was the basis for the separatrix operational space model described in subsection 1.2.6.

Chapter 3

Results

This chapter gives an overview of results obtained in the scope of this thesis. Where possible, results are presented in the form of introductory commentary and subsequent publications or drafts to be submitted with high confidence of eventual acceptance with introductory remarks. Other supplemental materials and results of ongoing analyses are also included.

3.1 L-H transition in the COMPASS tokamak

The COMPASS tokamak is able to reach H-mode using even only ohmic heating power thanks to its modest size and parameters [94]. Additional Neutral beam injection heating is also available, but the ohmic heating controlled mainly by the plasma current is much easier to accurately quantify and control. For this reason in all of the experiments described in this section only purely ohmic heating was used.

3.1.1 Limit cycle oscillations measurements

The limit cycle oscillations described in subsection 1.2.5 are routinely observed in the COMPASS tokamak. Several dedicated campaigns led and analyzed primarily by the author focused on their characterization and resulted in a first-author publication [63] at the end of this section. The experiments used primarily a multi-pin probe head (featuring both Langmuir and ball-pen probes, a modification of the probe head used for Reynolds stress measurements [56]) on a reciprocating manipulator in order to capture the behavior of various edge plasma quantities (such as density, temperature, velocity and their fluctuation power) throughout a limit cycle oscillation over a relatively wide radial range covering both the SOL and the region inside the LCFS.

The measured data were conditionally averaged based on the phase of the oscillation observed on magnetic pick-up coils and on the radial location of the probe measurements. This resulted in 2D-like average radial profile evolution of various quantities. The magnetic component was originally thought to be m=1 left-right asymmetric, but ongoing analysis shows that is may be actually up-down asymmetric with an additional m=2 component in agreement with the theory in [117].

Overall it was found that the pressure and velocity shear profile degradation inside the separatrix slightly precedes the phase with the greatest turbulent fluctuation intensity as can be seen in Figure 3.1. This behavior points to a pressure-drive ballooning-like profile degradation and subsequent transport, rather than to zonal flows being generated by turbulence. Furthermore, the Reynolds stress drive was found to be insufficient to explain the growth of the velocity.

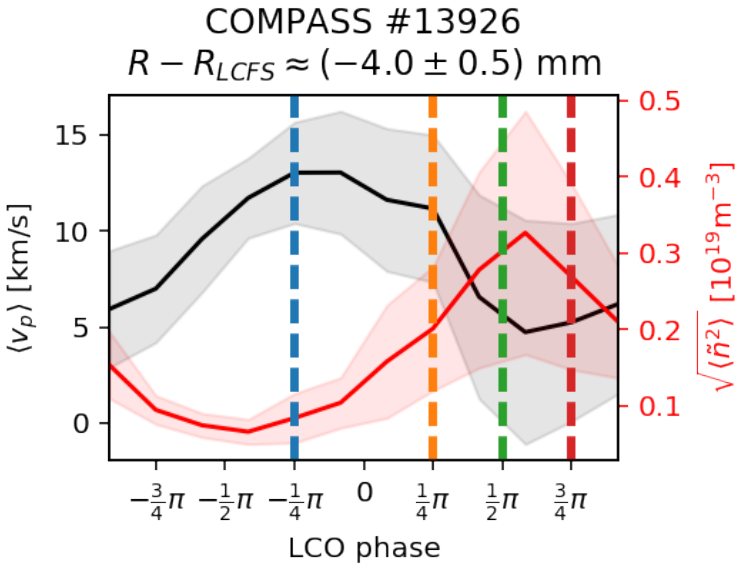

Figure 3.1: Average evolution of poloidal velocity and turbulent fluctuations intensity during a conditionally averaged limit cycle oscillation observed in the COMPASS tokamak using a reciprocating multi-pin probe head. Not part of the original publication [63].

However, the conditionally averaged density profile from Lithium beam emission spectroscopy showed that the steepest gradient region during the "quiescent" phase of the cycle is deeper inside than where the reciprocating probe head was able to measure. Therefore, it is possible that there is some zonal flow activity involved in the LCO dynamics, but was not observed by the reciprocating probe measurements.

Nevertheless, the temporal ordering points towards a ballooning, ELM-like dynamic late in the I-phase which has been observed also in other tokamaks [119]. Since the LCO on COMPASS are typically strongly influenced by saw-tooth crashes, it is possible that the heat pulse delivered by the crashes moves the dynamics closer to the late part of the I-phase, closer to type-III ELMs. The incompatibility of the measurements in COMPASS and other tokamaks with the zonal flow predator-prey model motivated the extension of the LCO model in [117] as shown in section 3.2.

IOP Publishing | International Atomic Energy Agency Nuclear Fusion

Nucl. Fusion **58** (2018) 112010 (12pp) https://doi.org/10.1088/1741-4326/aabb19

Limit cycle oscillations measurements with Langmuir and ball-pen probes on COMPASS

O. Grover[1,2], J. Seidl[1], D. Refy[3], J. Adamek[1], P. Vondracek[1,4], M. Tomes[1,4], P. Junek[1], P. Hacek[1,4], J. Krbec[1,2], V. Weinzettl[1], M. Hron[1], S. Zoletnik[3] and The COMPASS Team[1]

[1] Institute of Plasma Physics of the Czech Academy of Sciences, Prague, Czech Republic
[2] Faculty of Nuclear Sciences and Physical Engineering, Czech Technical University in Prague, Czech Republic
[3] Wigner RCP, Budapest, Hungary
[4] Faculty of Mathematics and Physics, Charles University, Prague, Czech Republic

E-mail: grover@ipp.cas.cz

Received 16 January 2018, revised 9 March 2018
Accepted for publication 3 April 2018
Published 3 October 2018

Abstract

This contribution presents the experimentally observed edge plasma evolution during limit cycle oscillations (LCO) measured with a new Langmuir and ball-pen multi-pin probe head at the COMPASS tokamak. The observed LCO regime modulates the intensity of density fluctuations δn_e, radial electric field E_r and intensity of D_α emission with a frequency 3–5 kHz. The density fluctuations grow after E_r decreases in strength which appears to be strongly correlated with the evolution of the pressure gradient $\partial_r p$. The magnetic signature of the LCO shows a left–right asymmetry with propagation from the low to high field side. High-frequency (above 100 kHz) precursor-like oscillations are observed as well.

Keywords: magnetic confinement, tokamak, L-H transition, limit-cycle oscillations, edge-localized modes

(Some figures may appear in colour only in the online journal)

1. Introduction

The high confinement mode (H-mode) [1] is a key operating regime for future fusion reactors due to the reduction of turbulent transport in the plasma edge and the consequent improvement in confinement. While the observation of this mode in many devices has resulted in a quite robust description of the edge transport barrier maintained by strong sheared flows responsible for the quenching of turbulent transport [2], a robust model of the dynamical process leading to the emergence of such a barrier is still missing. Such a model is of great interest for predictive modeling of the power threshold for the so called L-H transition from the L-mode (low confinement) to the H-mode, because designs of future reactors such as ITER and DEMO are currently based on empirical scalings of the threshold with large uncertainties [3].

The phenomenon of limit-cycle oscillations (LCO) a.k.a. the I-phase (intermediary phase) observed on many devices [4] during 'gradual' L-H transitions offers an opportunity to study the dynamics of the L-H transition, specifically the interplay between turbulence and sheared flows. The LCO were already predicted by a 0D reduced predator-prey-like model of the L-H transition [5]. In this model and its 1D extensions [6] the turbulence acts as the prey, while the zonal sheared flow [7] with a finite but smaller-than-pressure-gradient radial scale decorrelates the turbulence structures as the predator. The poloidal zonal flow is accelerated by the radial gradient of the perpendicular Reynolds stress (RS) $\langle \tilde{v}_p \tilde{v}_r \rangle$ [8, 9] resulting from the covariance of the poloidal $\tilde{v}_p$ and radial $\tilde{v}_r$ velocities of the turbulent structures. The process was also cast as a transfer of energy between zonal flows and turbulence [10] through the Reynolds power per unit mass $\langle \tilde{v}_p \tilde{v}_r \rangle \partial_r \langle v_p \rangle$ with the velocity shear $\partial_r \langle v_p \rangle$. The energy can be also transported by turbulence spreading, therefore, in experiments with point measurements (not zonally averaged) such as [11] the quantity $\partial_r \langle \tilde{v}_p \tilde{v}_r \rangle \langle v_p \rangle$ including the energy transport is used instead. In the model the zonal flows dissipate in the absence of turbulent drive due to collisional and other damping, thereby locking

in a state of oscillation between states of high and low turbulence with the zonal flow intensity lagging by a phase shift of $\pi/2$ typical of LCO in predator-prey models [5]. Meanwhile, with enough external power input the pressure gradient gradually develops over the low turbulence periods until it results in a mean sheared flow sufficient to decorrelate turbulence continuously.

However, experiments on different devices show a different dominant influence of either zonal flows generated by turbulence, or the mean sheared flow balanced by the pressure gradient at the plasma edge [4, 12]. On the one hand, there were observations of zonal flows coupled with turbulence in TJ-II [13], axisymetric zonal flows during LCO [14] in DIII-D and geodesic acoustic mode (GAM) activity connected with the L-H transition on ASDEX Upgrade [15] and zonal flow production by turbulent Reynolds stress in Alcator C-Mod [16]. On the other hand, in other experiments on JFT-2M [17] and recently ASDEX Upgrade [18] a negligible role of zonal flows was observed and the role of the mean sheared flow was highlighted. In particular, the observations differ by the time ordering of the radial electric field (absolute intensity) E_r and the turbulence intensity. While in experiments with zonal flow activity the electric field intensity maximum lags the turbulence intensity maximum, the order is reversed in experiments where the electric field is controlled mainly by the pressure gradient. In HL-2A both kinds of evolution were observed [19] with so called type-Y LCO featuring turbulence-generated zonal flows and type-J LCO controlled mainly by the pressure gradient. The type-Y LCO after the L-I transition progresses into the type-J oscillation and an I-H transition is observed only after a type-J oscillation.

Recent analyses of the I-phase on ASDEX Upgrade [20] and EAST [21] also noted the magnetic signature of the LCO. A likely related phenomenon in terms of the magnetic signature is the M-mode on JET which also features such a periodic modulation of the pedestal profile and the outward flux [22]. In these devices an up–down poloidally asymmetrical magnetic low-frequency oscillation associated with the modulation was observed. Such an up–down asymmetry was theoretically interpreted as the result of ballooning transport on the midplane [23]. In addition to the low frequency magnetic oscillations precursor oscillations were also observed on ASDEX Upgrade, highlighting the similarity between the observed LCO and type-III ELMs [20].

This study concentrates on oscillation phenomena routinely observed during the L-H (and also H-L) transition in COMPASS discharges. These oscillations have a typical frequency of 3–5 kHz. They can be easily observed on D_α emission as well as on other diagnostics, e.g. magnetic pickup coils, probes, etc. These oscillations were initially thought to be ELMs due to the similarity in D_α emission traces. However, they significantly differ from ELMs routinely observed during ELMy H-mode discharges at least in two main aspects: Their amplitude in D_α emission and the power of magnetic and probe-measured fluctuations is (at least in the initial phases) significantly lower, and they do not reliably follow the frequency scaling with the power through the separatrix reported in [24]. The latter point was the original reason which brought focus to this phenomena.

For these reasons alternative explanations were sought. One possibility is that these are LCO observed on other devices during the L-H transition. In order to investigate whether these are LCO it was necessary to resolve the temporal interplay between turbulence and flows in the plasma edge. Due to the modest typical edge temperature of ~50 eV in the COMPASS tokamak [24] it is possible to directly measure $E \times B$ velocities with probes up to ~0.5 cm inside the last closed flux surface (LCFS).

Arrays of Langmuir probes have been already used in HL-2A [19] and EAST [11, 25] for the investigation of LCO. However, such Langmuir probe measurements may be influenced by fluctuations of the electron temperature which may play an important role in fluctuation-based quantities, such as the RS as was shown in [26]. In order to prevent the contamination of measurements by temperature fluctuations and to be able to measure them during the LCO as well, a probe head equipped with both Langmuir (LP) and ball-pen (BPP) [27] probes in similar geometric configurations was developed and used for these experiments. The COMPASS tokamak has also plenty of magnetic Mirnov (pickup) coils for the study of magnetic modes.

The rest of this article is structured as follows: in section 2 the diagnostic and experimental setup is described, in particular the multi-pin probe head design. The results of measurements in a gradual L-I-H transition are reported in section 3.1 and those in a stationary LCO regime in section 3.2. Finally, the article is concluded with key observations and their discussion and future experimental plans in section 4.

2. Methods

2.1. Discharge parameters

All the results presented in this article come from discharges performed in the COMPASS tokamak ($R = 0.56$ m, $a = 0.2$ m) [24]. These were deuterium discharges in a lower single-null diverted configuration with an elongation of 1.78, lower and upper triangularity 0.2 and 0.54 at the LCFS, respectively. The ion ∇B drift direction was in the favourable direction (towards the X-point). The X-point height was quite small in order to prevent contamination of the experiment by modes of a yet-unknown origin with comparable frequencies (~6–7 kHz) often observed with a high X-point close to the L-H transition. Chamber conditioning procedures were used, but with no direct Z_{eff} measurement the isotope purity cannot be fully guaranteed. The line-averaged densities were kept in the range of $5-7 \cdot 10^{19}$ m^{-3} and the toroidal on-axis magnetic field was $B_\phi = 1.15$ T. All the discharges were purely ohmic. In the steady-state oscillation scenario in discharges #13925 and #13926 the plasma current was $I_{\mathrm{pl}} \approx 190$ kA. In the current-ramp scenario in discharges #13963 and #13960 the plasma current was ramped up (after shaping) from 200 kA to 250 kA in order to induce a slow L-H transition. Oscillations with similar characteristics such as those reported in this article also often appear in other discharges within a quite wide

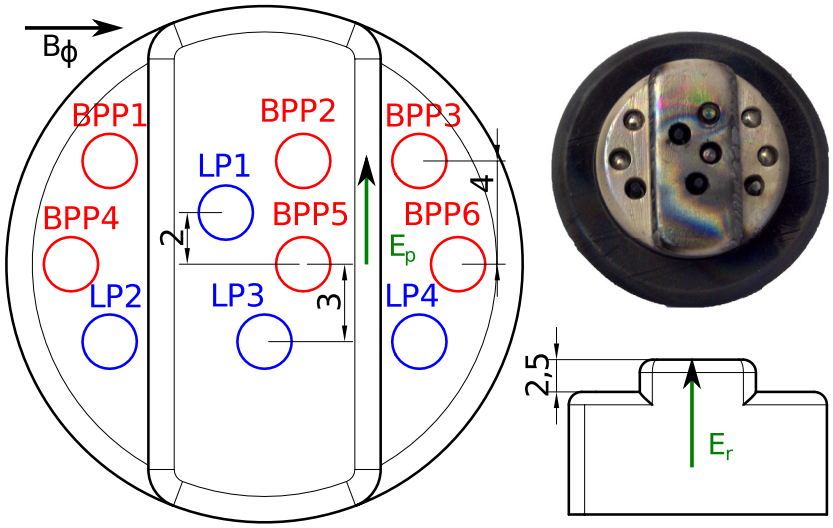

Figure 1. Schematics and a picture of the modfied Reynolds stress probe head containing Langmuir (LP, blue) and ball-pen (BPP, red) probes. All dimensions are in mm. The directions of the toroidal magnetic field B_ϕ, the radial E_r and poloidal electric field E_p are also displayed.

range of operational parameters. However, the discharges presented in this article constitute the currently best selection in terms of the optimized scenario and simultaneously working diagnostics capable of measuring quantities of interest at the plasma edge with sufficient temporal resolution.

2.2. Probe and other diagnostics

The temporal interplay between turbulence and flows during the oscillations under investigation was measured by ball-pen (BPP) and Langmuir probes (LP) in a special, compact geometric configuration on a horizontally reciprocating probe head on the outer midplane. This configuration enables fast (5 MS s^{-1}), simultaneous, multi-point measurements of key quantities such as the floating potential V_{fl}, the plasma potential ϕ, electron temperature T_e, density n (from the ion saturation current I_{sat}^{+}), poloidal and radial electric fields E_p and E_r. The unique combination of BPPs and LPs enables direct measurement of the plasma potential and the electron temperature (in electronvolts) through the formula $V_{fl} = \phi - \alpha T_e$ where the coefficient α is the logarithm of the ratio of the electron and ion saturated currents and is different for each probe type.

The probe head used in this study is a modification of a similar configuration previously used to investigate the effect of electron temperature fluctuations on the measurement of Reynolds stress with Langmuir and ball-pen probes as reported in [26]. A detailed description of the original probe head geometry and an assessment of its measurement properties, e.g. the α coefficient of the 2 mm BPPs used, electric field measurement properties, can be found in [26] as well.

The main differences between the modified and original designs are the addition of probes `BPP4` and `BPP6` in the new modified design and the use of boron nitride (BN) material with greater purity for its construction. The former change enables the calculation of both the electric fields with BPPs at the same virtual point, removing the risk on any phase shift between separated measurement points. The latter change resulted in almost no plasma cooling or perturbation in comparison to the original probe head which significantly cooled the plasma and often led to disruptions as was reported in [26]. The construction from a BN support in which the probes are directly embedded removed the need for extra shielding, and in conjunction with the triangle-mesh-like placement enables placing probes very close to each other.

Figure 1 shows the schematic of the modified probe head design. The radial separation between the probes is 2.5 mm and the poloidal separation is ~4 mm. The radial E_r and poloidal E_p electric fields can be calculated from differences of floating or plasma potentials measured by neighboring LPs or BPPs, respectively. For the datasets presented in this article all the electric fields calculated from differences of plasma potentials of appropriately positioned BPPs were averaged into one virtual point located approximately at the 'center of mass' of these BPPs. This procedure should mitigate any effect of a possible time lag between electric fields measured at different positions, which could affect the calculation of the Reynolds stress. The averaging also removes a symmetrical (in terms of polarity and magnitude) stationary offset on the partially shadowed probes on the sides with respect to the probes in the middle at an equivalent radial location. This offset does not affect the fluctuation characteristics. For details see [26]. `LP1` was set to ion saturated current measurement mode in order to measure density fluctuations. The electron temperature T_e in eV units was calculated from the difference of potentials measured by `BPP5` and `LP3` as $T_e(\mathrm{eV}) \approx (\phi^{\mathrm{BPP5}} - V_{fl}^{\mathrm{LP3}})/2.2$, for details on this method see [27]. The density n (assuming local quasineutrality) was estimated from the ion saturated current under the assumptions of the ion temperature being about double T_e for the sound velocity estimation and using the effective collection area of the probe pin. The probe pin is a graphite cylinder with height 1.5 mm and diameter 0.9 mm. Its effective collection area was assumed to be its rectangular cross section and its top base. The correction proportional to $\sqrt{T_e}$ (from the sound velocity)

removes the temperature fluctuations from the ion saturated signal, i.e. the resulting density signal has significantly different fluctuation characteristics with respect to the raw ion saturation signal. Due to the applied assumptions, the density estimate is correct only up to a multiplicative numerical factor, but the estimate is expected to be correct in terms of the order of magnitude and fluctuation characteristics. Finally, the electron pressure p_e was estimated from the product nT_e. Because there were no diagnostics capable of measuring the ion temperature with sufficient temporal and spatial resolution available, the electron temperature is from here on taken as an estimate of the ion temperature (and the electron pressure for the ion pressure) evolution as well. The poloidal v_p and radial v_r velocities were obtained as the $E \times B$ velocities calculated from the radial E_r and poloidal E_p electric fields divided by the local toroidal magnetic field B_ϕ ($\sim$0.9 T around the LCFS in the presented discharges), respectively.

Because this probe head cannot directly measure the radial derivative of the electric field and related quantities (e.g. RS), it is necessary to employ conditional averaging or aggregation of measurements at different radial reciprocation positions for the calculation of higher order radial derivatives. The averaging can be done over the radial reciprocation trajectory within one discharge or over a set of highly repeatable discharges. Due to the limited experimental time and repeatability of discharges the former approach was taken in the presented experiments.

The radial reciprocation trajectories were simple in-out plunges with an average velocity $\sim$1 mm ms^{-1}, reaching at most $\sim$5 mm inside of the LCFS. The reciprocation velocity is not constant, because the probe slows down to 0 mm ms^{-1} at the point of the trajectory reversal, i.e. the deepest reciprocation. Beyond the reciprocation depth of $\sim$5 mm inside the LCFS the probe head starts to affect the plasma through the release of impurities from its BN body. Beyond $\sim$0.5 cm outside the LCFS the dynamics are mostly determined by the SOL transport of structures from the edge and hence not relevant for the studies here. For these reasons the measurements were executed only up to $\sim$0.5 cm inside the LCFS and the study concentrated on the symmetrical region of up to $\sim \pm$0.5 cm outside the LCFS.

All radial coordinates in this article are situated on the outer midplane (OMP) and shown with respect to the radial OMP LCFS position. The radial OMP LCFS position obtained from the magnetic reconstruction has a systematic error of $\sim$1–2 cm as indicated by the associated velocity shear layer (VSL) and the temperature pedestal in diverted plasmas [26, 27]. Fortunately, this systematic offset remains roughly constant during the whole flat-top. For each discharge it was determined as the radial reciprocation position with respect to the magnetic reconstruction LCFS where $\langle E_r \rangle = 0$, i.e. the VSL, and was subtracted before plotting any radial coordinates. Altogether, the uncertainty precision of the radial position with respect of the LCFS is about 1 mm when taking into account the precision of the position measurement, the offset correction and the averaging done in the following sections.

The magnetic signature of the mode associated with the oscillations under study was investigated with two arrays named A and C of magnetic (Mirnov) pickup coils. The arrays are separated by a toroidal angle of $\Delta\phi = 3\pi/4$. Each coil array features 24 coil triplets (measuring all three magnetic field derivative components when connected) approximately uniformly distributed in the poloidal angle [28]. From the A array the coils measuring the components of the magnetic field time derivative locally perpendicular (normal) $\dot{B}_r$ and parallel (tangential) $\dot{B}_\theta$ to the vessel wall were used. From the C array only selected $\dot{B}_\theta$ coils connected to the same data acquisition system were used for the determination of the toroidal mode structure.

The Lithium Beam Emission Spectroscopy (Li-BES) system [29] installed on COMPASS was used to measure density profiles up to the pedestal top in fast chopping mode with 10 μs temporal resolution. Fast chopping mode means that the beam is turned on and off with 100 kHz frequency in order to be able to distinguish between the background and the beam light emission. This is crucial since the LCO modulates the background emission as well.The radial resolution of the system is $\sim$1 cm. The system measures profiles approximately on the outer midplane.

3. Results

The gradual L-I-H transition described in the following subsection with intermittent I-phases of several LCOs offers an opportunity to characterize and investigate the L-I transition and the first LCO cycle. The gradual progression from L-mode through I-phases to H-mode was also used to compare the density profiles of these different confinement regimes.

The stationary LCO regime was then used to characterize the LCO cycle with greater temporal and radial resolution in section 3.2.

3.1. Slow L-H transition

Figure 2 shows a temporal evolution from L-mode to H-mode through intermittent I-phases with LCO as indicated by the D_α emission intensity in the COMPASS discharge #13963. It is clear that the early L-I transitions as well as later I-H transitions follow the saw-teeth crashes as indicated by the SXR signal from the core. It is not entirely clear whether the later periods of oscillations between prolonged states with an H-mode-like D_α level are still regimes with LCO or small type-III ELMs, because the typical H-mode confinement time $\sim$25 ms in COMPASS is longer than the duration of these phases. The LCO have a distinct signature (negative spikes) in the integrated B_θ signals measured by coil `MA20` below the divertor close to the outer strike-point. These signatures are typically the strongest in the signal from this coil, but other coils at different poloidal locations also measure a clear magnetic signature. The structure of this associated magnetic mode is studied in greater detail in section 3.2. Since the D_α evolution is expected to be the result of a complicated process involving SOL transport and edge density fluctuations, and the diagnostic's field of view includes both the edge and the divertor regions, the magnetic signature on the coil MA20 was chosen as the reference LCO phase signal for conditional

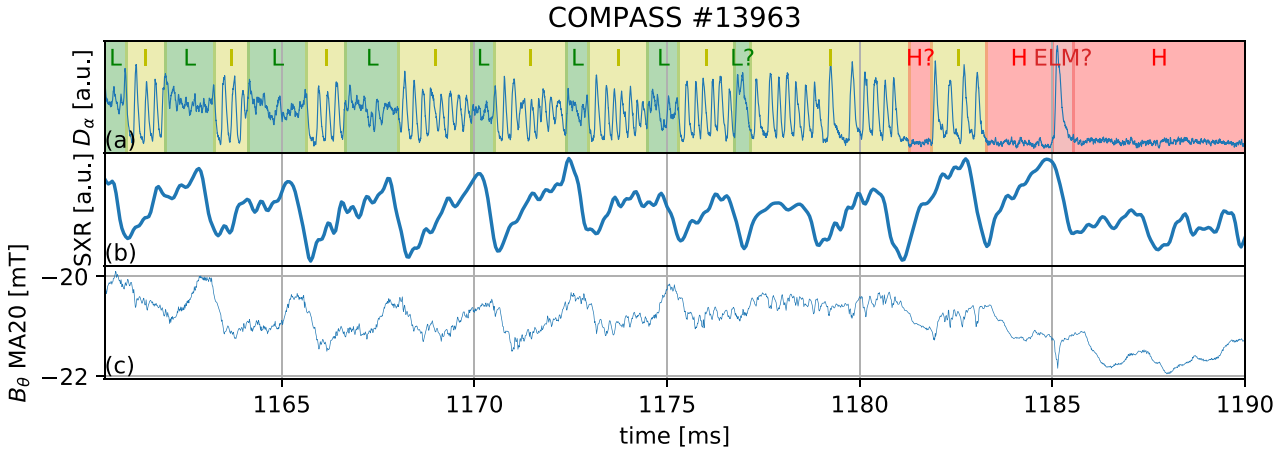

Figure 2. Temporal evolution of selected quantities in the COMPASS discharge #13963, from L-mode through intermittent intermediate phases (I-phase) to the H-mode. The time traces of the (*a*) D_α emission, (*b*) core soft x-ray emission, (*c*) tangential (to vessel) magnetic field measured by Mirnov coil MA20 below the divertor.

averaging purposes. The MA20 signal signature is typically by $\sim 40\,\mu$s delayed with respect to the probe measurements on the OMP. This delay was not observed to change in the presented discharges where the global and edge parameters were held constant, but it could change under different discharge conditions. The delay is related to the phase propagation of the magnetic signature described in greater detail section 3.2. The signature of these oscillations in magnetic, D_α and probe measurements becomes stronger as the discharge gradually progresses towards H-mode. There is no clear difference or transition between the early, small oscillations in the L-I-L phases and the oscillations closer to the H-mode which gradually become similar to regular type-III ELMs.

During the observed I-phases close to the L-H transition no significant GAM activity was observed. While some activity in the frequency band 25–35 kHz typical for GAMs on COMPASS as reported in [30] was observed, the activity is very weak in comparison to L-mode levels and only intermittent. The suppression of GAM activity is similar to that observed in H-mode. The GAM appears to recover during the intermittent L-mode phases.

The data measured by the probes in the first three L-I transitions in figure 2 were conditionally aligned in time according to the instantaneous phase of the B_θ `MA20` signal. The phase was obtained from the analytic signal calculated with the Hilbert transform over a 3.7–5.5 kHz bandpassed version of the signal. This phase-alignment was necessary since the frequency slightly changed throughout the discharge, mostly as a result of slow density fluctuations on the scale of several ms. The oscillation frequency appears to be sensitive to these slow density fluctuations during the flat-top. Typically, the LCO frequency decreases with increasing density, but no systematic scaling analysis has been done yet. Since the probe was reciprocating inwards with an average speed of ~ 0.4 mm ms^{-1} the measurements were separated by roughly a millimeter. This enables the calculation of approximate radial derivatives from the radially separated measurements conditioned on the MA20 B_θ phase.

The separation of scales into average and fluctuating components was done by time-domain filters as was done in [11]. The separation frequency cutoff was chosen as 13 kHz in order to capture higher harmonics of the base LCO frequency.

The 3 aligned traces of the L-I transitions are shown in figure 3. The relative time $t_\mathrm{r} = 0\,\mu$s corresponds to the π phase of the reference phase signal, i.e. roughly the minimum of the negative spike in the B_θ MA20 signal as can be seen in figure 3(*e*). The phase signal was converted to time units by dividing the unwrapped phase by the frequency of 4.5 kHz. The position of the probe during these periods was such that the traces in order correspond to the evolution about 1 mm outside the LCFS, around the LCFS and about 1 mm inside the LCFS.

The evolution can be split into several distinct stages: The preceding L-mode terminated by a saw-tooth crash up to $t_\mathrm{r} \approx -250\,\mu$s, the subsequent turbulence suppression period up to $t_\mathrm{r} \approx -100\,\mu$s and then the turbulent phase of the LCO up to $t_\mathrm{r} \approx 0\,\mu$s and the following turbulence suppression.

The saw-tooth crash identified by the fall of the core SXR signal occurs around $t_\mathrm{r} = -500\,\mu$s. Due to the typical travel time of several 100 μs of the heat pulse to the edge [30] several quantities are strongly modulated just before $t_\mathrm{r} = -300\,\mu$s quantities, e.g. there is a negative spike in the $E_\mathrm{r} \times B_\phi$ velocity, and its shear $\partial_\mathrm{r} v_\mathrm{p}$ is quite high, and the pressure gradient is modulated. While the turbulence is subsequently gradually suppressed the Reynolds stress and its gradient is rather small. This indicates that the initial turbulence suppression is due to the saw-tooth crash changing the core turbulence.

During the turbulence suppression period the pressure gradient inside the LCFS remains relatively high and so does the velocity shear while outside the LCFS the velocity shear is very low. Several tens of μs later both quantities begin to decrease inside the LCFS and the turbulence intensity rises as seen in the density fluctuations in the frequency range 150–300 kHz, shown in an inset plot. Precursor-like fluctuations at similar frequencies are seen also in the magnetic field derivative $\dot{B}_\theta$ (shown in an inset plot), but are delayed by $\sim 40\,\mu$s with respect to density fluctuations. This delay is studied in greater detail in section 3.2. Meanwhile, the pressure gradient inside the LCFS decreases, while it increases outside the LCFS.

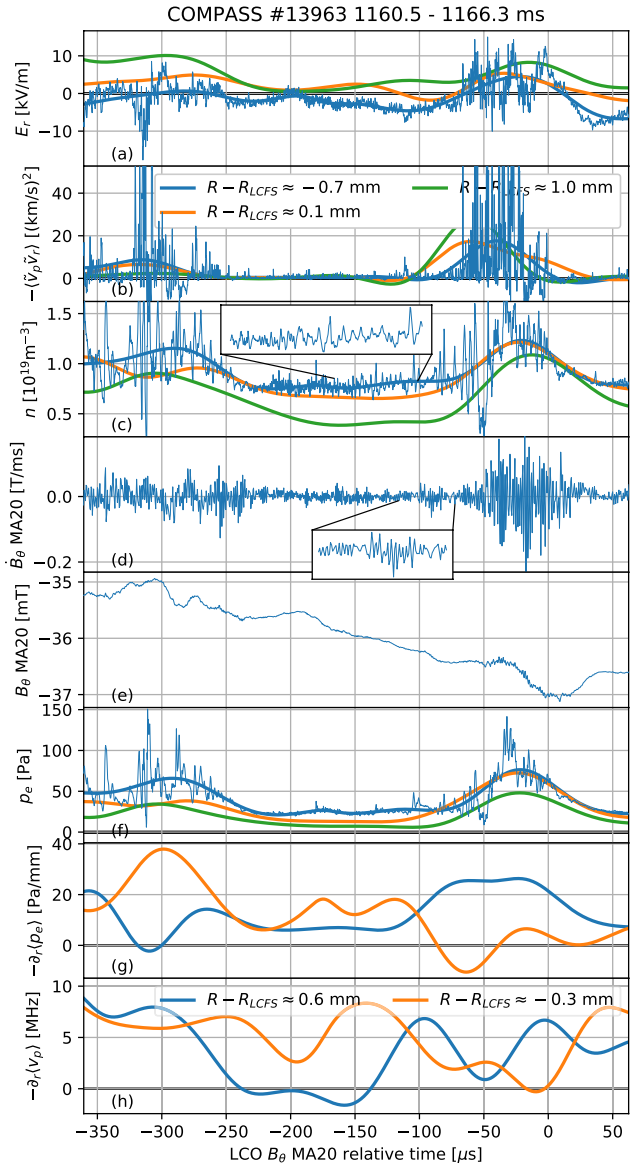

Figure 3. Traces of the first three L-I transitions in the COMPASS discharge #13963. The raw data and low-frequency components (<13 kHz) of (*a*) the radial electric field E_r, (*b*) the negative of the Reynolds stress $-\langle\tilde{v}_p\tilde{v}_r\rangle$, (*c*) the density n, (*d*) the magnetic field derivative $\dot{B}_\theta$ measured by tangential coil MA20, (*e*) the integrated field B_θ, (*f*) the electron pressure p_e, (*g*) its gradient, (*h*) the poloidal velocity shear $-\partial_r\langle v_p\rangle$ are shown in order for different radial positions of the reciprocating probe.

The fluctuation energy in both E_r and p_e gradually increases. The E_r fluctuations are likely due to coherent structures moving past the probe. These structures exhibit a cross-phase between density and potential fluctuations close to $\pi/2$, suggesting that they have a ballooning character. During the most turbulent phase the velocity shear remains low and E_r drops to levels outside the LCFS. The Reynolds stress increases during the turbulent phase, but the Reynolds power is very small since the velocity shear is small at that time. Once the turbulence dies away, the velocity shear and the pressure gradient begin to recover.

While the alignment is undoubtedly imperfect and the statistics of only 3 traces is insufficient for straight-forward conclusions, it shows the general ordering of the LCO cycle observed in all the discharges where the probes were measuring.

Figure 4 shows a detailed slice of the density and magnetic fluctuation traces along with their wavelet spectrograms in a typical LCO cycle later in the discharge. The precursor-like density oscillations start at ~1177.75 ms in the displayed cycle and typically have a frequency in the range 150–300 kHz. The power of these oscillations is quite low, but they occur systematically. Later they evolve into stronger and more regular fluctuations, typically in the frequency range 100–200 kHz. The magnetic signature also features coherent fluctuations in similar frequency ranges and temporal ordering, but delayed by ~40 μs.

The density profiles measured by the Li-BES system in discharge #13960 (similar to #13963 in terms of the gradual L-I-H evolution) conditioned on the phase of the L-I-H transition are shown in figure 5. The radial coordinate of the density profiles is mapped to the same coordinates as those used with the probe data. However, the VSL position correction comes from the E_r profile measured by the probes. The high/low turbulence intensity conditioning phase of the LCO cycle was obtained as the high/low level of the 2–6 kHz bandpassed envelope of fluctuations in the frequency range 100–250 kHz on a Li-BES channel just inside the separatrix. The usage of the reference MA20 B_θ phase signal was not possible, because the Li-BES system clock was not properly synchronized with other COMPASS diagnostics. This reference signal choice makes it possible to relate the Li-BES data to the turbulence intensity evolution during an LCO cycle.

The profiles during the phase of high turbulence intensity in the LCO cycle are only marginally steeper deeper inside the LCFS than in the preceding L-mode. However, closer to the LCFS the density is higher than in L-mode and the profile is flattened and extends further into the SOL. The profiles during the phase of low turbulence intensity (quiescent) in the LCO cycle are substantially steeper than in the high turbulence phase, particularly just inside the LCFS. In fact, the largest gradient in the pedestal region is almost as steep as the gradient of the pedestal in the ELM-free H-mode closely after the I-H transition. However, the pedestal is much wider in the H-mode profile, resulting in much higher densities deeper inside the LCFS. Altogether, these results suggest that the LCO regime has at least slightly enhanced particle confinement in comparison to L-mode, although it is not at the level of confinement in a fully developed H-mode. The flattening and extension of the profile in the turbulent LCO phase suggests that there is a large flux of particles across the LCFS in this phase.

3.2. Stationary oscillation regime

The discharge scenario with nearly stationary LCO throughout the whole flat-top offers an opportunity to study the LCO evolution with greater radial resolution.

For this purpose the data measured by the reciprocating probe in the range about ±3 mm from the LCFS were

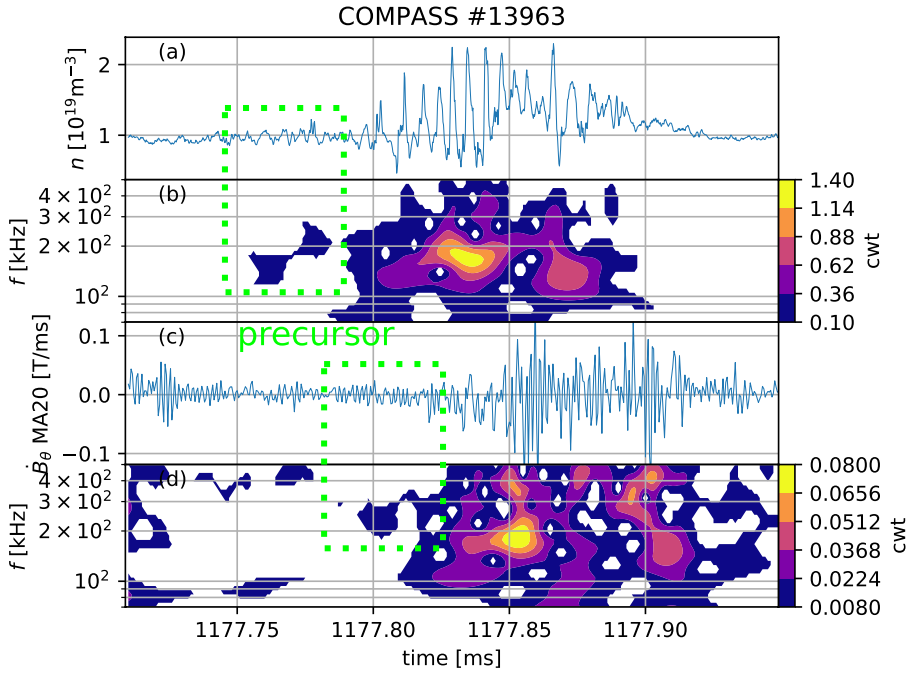

Figure 4. A short segment of (a) the density n trace and (b) its wavelet spectrogram and (c) the magnetic field derivative $\dot{B}_\theta$ MA20 trace and (d) its wavelet spectrogram showing the evolution of the density and magnetic fluctuations during a typical LCO cycle.

conditionally averaged. This average encompassed about 180 LCO cycles. The conditional trigger was again the instantaneous phase of the MA20 B_θ coil signal. The probe data were decimated (lowpassed to Nyquist and downsampled) to a sampling frequency of 1 MHz since no important fluctuations are expected beyond 500 kHz and it reduced the noise in the conditional average. Each data point measured by the probes with a given reciprocation position (again relative to the LCFS up to an offset) and a given MA20 phase was then assigned into a bin in a 2D-histogram-like algorithm which computed the mean and standard deviation of each bin. The resulting 2D map was plotted as contours in figure 6 for the COMPASS discharge #13926. The result in the discharge #13925 is similar. The radial derivative evolution of plotted quantities can be deduced from the density of contour lines. For better clarity several radial profiles from the same dataset are also plotted in figure 7. The radial width of each bin is almost 1 mm, but the corresponding horizontal errorbars are not shown for the sake of clarity. The dashed trends are linear splines with a knot at $R - R_{\mathrm{LCFS}} = 0$ mm (except for low density fluctuations where the trend is more complicated). The evolution of means and/or gradients of selected quantities inside and outside the LCFS are plotted as Lissajous curves in figure 8. Since the LCO frequency was about ∼4.5 kHz, the conditional oscillation phase covers about a 220 μs long window.

Since the density gradient evolution with respect to the turbulence phase qualitatively agrees with the Li-BES profiles shown in the previous subsection, the profiles measured by the probes are assumed to give a good estimate of the general steepening or flattening of the broader edge profile.

The conditionally averaged evolution is similar to that described in section 3.1. The temporal evolution can again

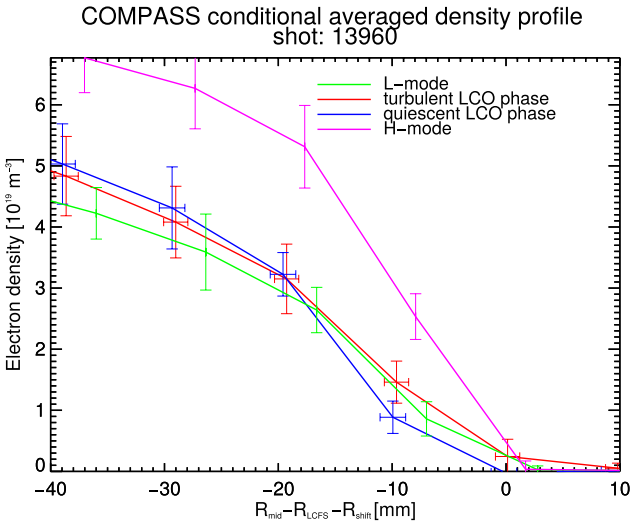

Figure 5. Li-BES density profiles of the edge plasma in the COMPASS discharge #13960. The radial coordinate on the x-axis is the distance from the outer midplane LCFS position with the probe-based VSL correction. Displayed are conditionally averaged profiles in L-mode, LCO phase with high (turbulent) and low (quiescent) turbulence intensity and in H-mode closely after the I-phase. The errorbars represent the standard deviation of the samples in the conditional average.

be split into several stages: The recovery of the pressure and velocity profile from the LCO phase $-\pi$ to $-\pi/4$, its gradual degradation and the rise in turbulence intensity up to $\pi/4$, the rapid velocity decrease and turbulence intensity increase around $\pi/2$ and the pressure profile flattening and ejection around $3\pi/4$.

When the poloidal velocity (and its shear) inside the LCFS reach their maximum around the $-\pi/4$ phase, the electron pressure profile is the steepest (inside the LCFS) and there

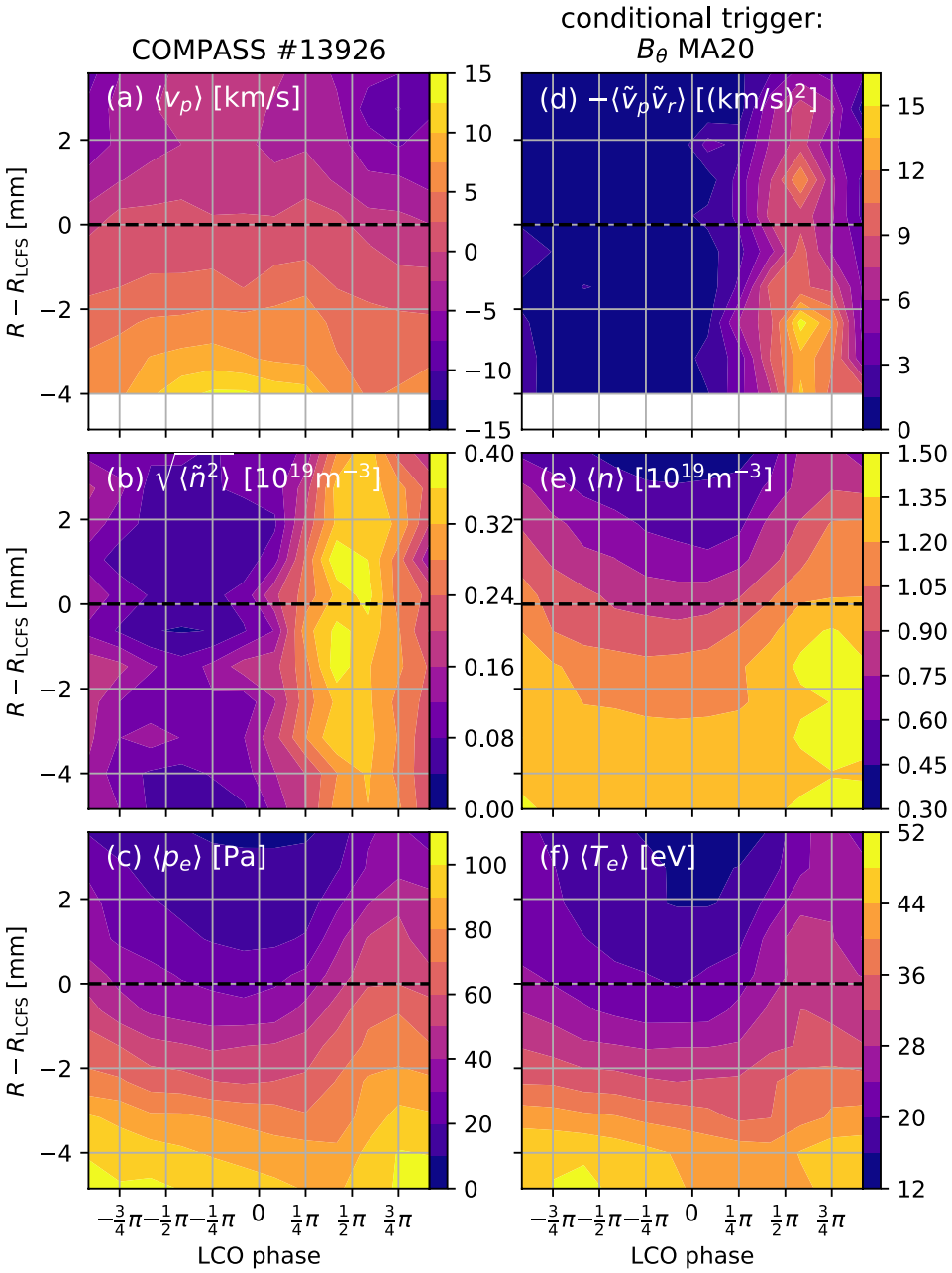

Figure 6. Conditionally averaged evolution of (*a*) the poloidal velocity $\langle v_\mathrm{p} \rangle$, (*b*) the RMS of density fluctuations $\sqrt{\langle \tilde{n}^2 \rangle}$, (*c*) the electron pressure $\langle p_\mathrm{e} \rangle$, (*d*) the negative of the Reynolds stress $\langle \tilde{v}_\mathrm{p} \tilde{v}_\mathrm{r} \rangle$, (*e*) the density $\langle n \rangle$ and (*f*) the electron temperature $\langle T_\mathrm{e} \rangle$ during an average LCO cycle measured by the Reynolds stress probe head in the discharge #13926.

is very little turbulence intensity as indicated by the RMS of density fluctuations $\sqrt{\langle \tilde{n}^2 \rangle}$. Outside the LCFS the turbulence intensity is also very low, but the velocity shear and the pressure gradient are small.

The subsequent, gradual turbulence intensity rise is correlated with the rise in the (negative of the) Reynolds stress $-\langle \tilde{v}_\mathrm{p} \tilde{v}_\mathrm{r} \rangle$ and the radial turbulent transport $\langle \tilde{v}_\mathrm{r} \tilde{n} \rangle$. The direction of the average radial turbulent transport is outwards through the LCFS to the SOL. Meanwhile, the pressure profile flattens inside the LCFS and 'extends' into the SOL. A similar evolution is visible on the velocity and its shear inside the LCFS. However, outside the LCFS the pressure gradient and the velocity shear slightly increase.

As $\pi/2$ is approached, the turbulence intensity continues to rapidly increase while the velocity and its shear rapidly decrease inside the LCFS. However, the velocity shear and the pressure gradient slightly increase outside the LCFS.

Once the turbulence intensity and correlated quantities peak around $\pi/2$ the pressure profile is 'ejected' through the LCFS and is generally flattened. The velocity profile is also flattened. While the flattening and 'ejection' of the pressure profile peaks the turbulence intensity is already decreasing.

Afterwards, the pressure profile begins to recover and so does the velocity. It is worth noting that the pressure profile steepness is mostly determined by the temperature profile, the density profile is much flatter inside the LCFS in comparison.

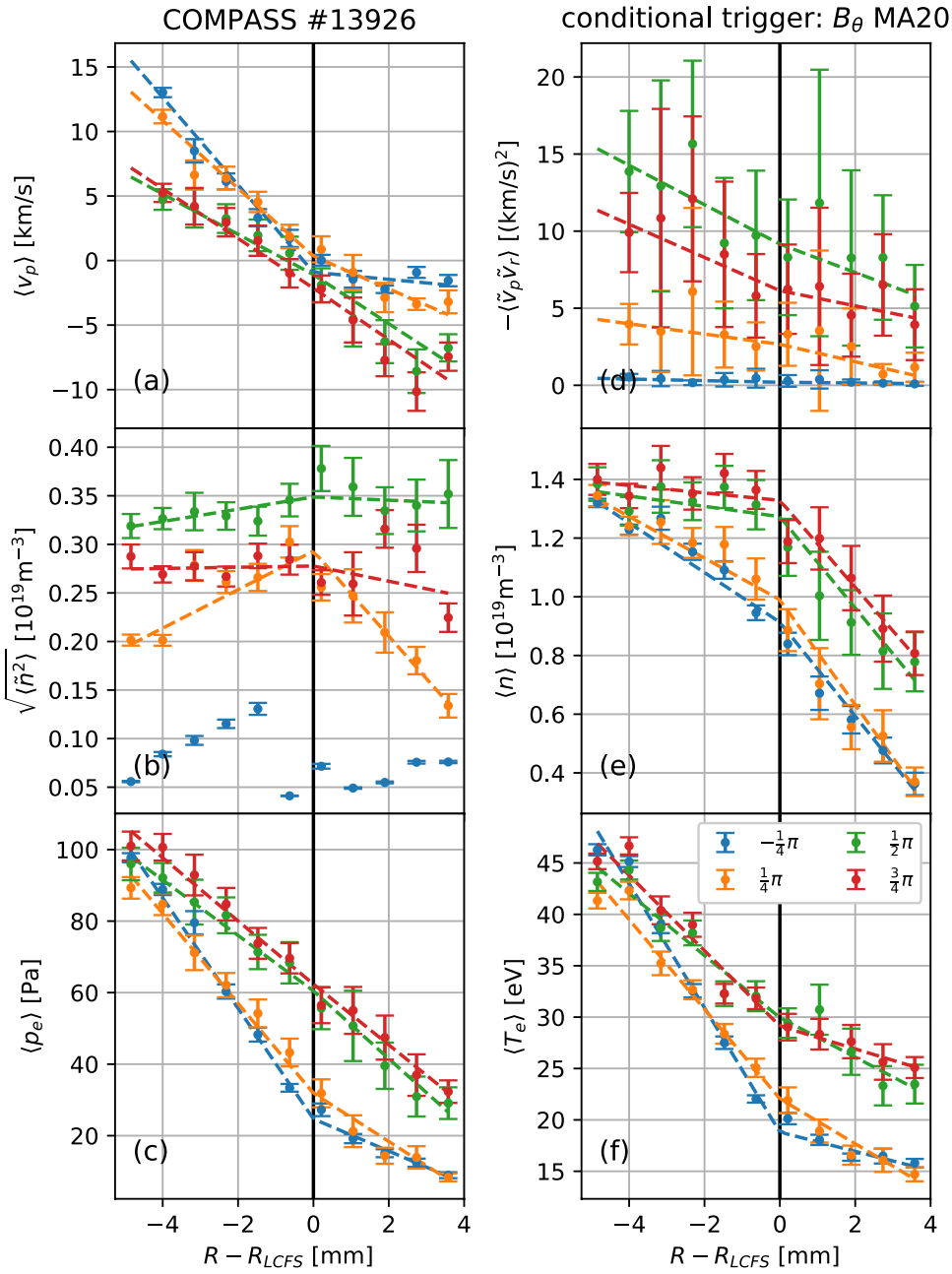

Figure 7. Conditionally averaged radial profiles of (*a*) the poloidal velocity $\langle v_\mathrm{p} \rangle$, (*b*) the RMS of density fluctuations $\sqrt{\langle \tilde{n}^2 \rangle}$, (*c*) the electron pressure $\langle p_\mathrm{e} \rangle$, (*d*) the negative of the Reynolds stress $\langle \tilde{v}_\mathrm{p} \tilde{v}_\mathrm{r} \rangle$, (*e*) the density $\langle n \rangle$ and (*f*) the electron temperature $\langle T_\mathrm{e} \rangle$ during selected phases of an average LCO cycle measured by the Reynolds stress probe head in the discharge #13926. The dashed trends are linear splines with a knot at $R - R_\mathrm{LCFS} = 0$ mm.

The Reynolds power per unit mass normalized by the effective turbulent energy production $\gamma_\mathrm{eff} \langle v_\perp^2 \rangle$ is negligible throughout the cycle, and reaches only up to ~10% close to the LCFS during the most turbulent phase. The effective turbulence growth rate $\gamma_\mathrm{eff} \approx 50\,\mu$s was estimated for the average turbulence energy $1/e$ rise time. The apparently negligible role of the Reynolds stress power is mostly due to the velocity (and its shear) inside the LCFS and the Reynolds stress being almost in counter phase.

The Lissajous curves in figure 8 show that the inside the LCFS the curves of the velocity, its shear and the pressure gradient with respect to the turbulence intensity rotate counter-clockwise, i.e. the velocity and its shear intensity leads the turbulence intensity. It is also interesting to note, that the velocity shear has a more complicated behavior—nearly a reversal of the curve direction—during the phase of the maximum turbulence intensity which is not so clearly seen on the velocity evolution itself. Outside the LCFS the evolution is reversed in terms of the cycle curve direction with respect to the direction inside the LCFS.

The magnetic signature of the LCO was studied in the discharge #13925 (similar to #13926 but with a more coherent magnetic signature). The evolution of the time derivative of the magnetic field $\dot{B}_\theta$ measured by the Mirnov coil MA20

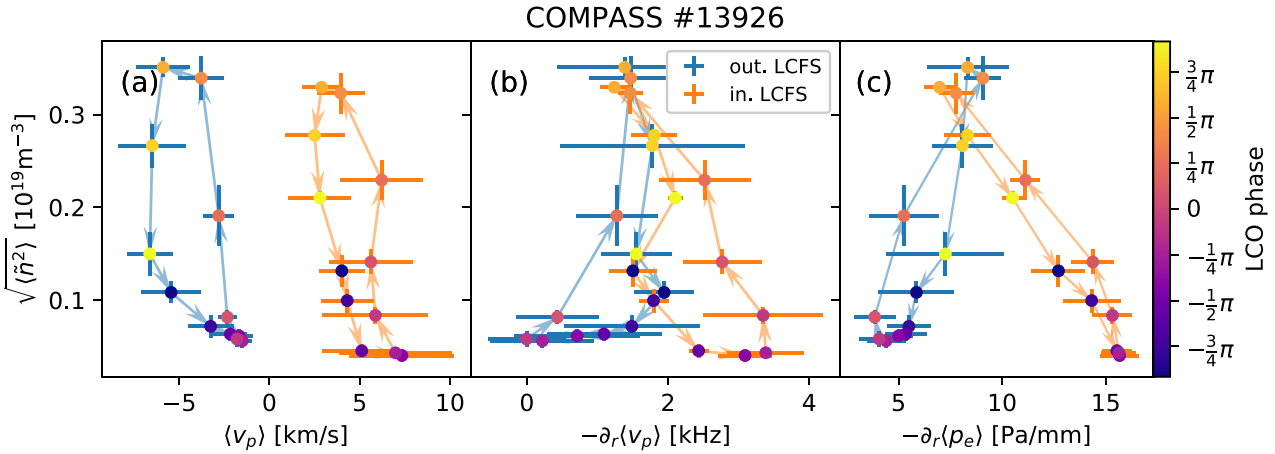

Figure 8. Lissajous curves of conditionally averaged evolution of the RMS of density fluctuations $\sqrt{\langle\tilde{n}^2\rangle}$ with respect to (*a*) the the poloidal velocity $\langle v_\mathrm{p}\rangle$, (*b*) the poloidal velocity shear $-\partial_\mathrm{r}\langle v_\mathrm{p}\rangle$, (*c*) the negative of the pressure gradient $-\partial_\mathrm{r}\langle p_\mathrm{e}\rangle$ during an average LCO cycle measured by the Reynolds stress probe head in the discharge #13926. Blue and orange points represent the average and/or gradient of selected quantities inside and outside the LCFS, respectively.

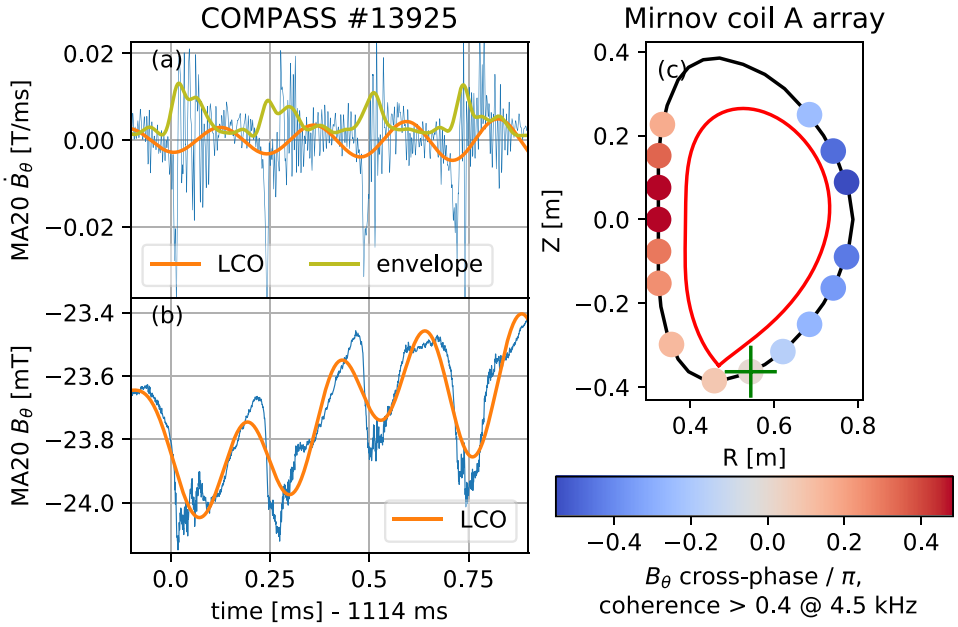

Figure 9. Typical signature of LCO in (*a*) $\dot{B}_\theta$ and (*b*) integrated B_θ for the coil MA20. (*c*) Cross-phase with coherency >0.4 between fields measured by tangential magnetic pickup coils in array A with respect to the coil MA20 (green cross). The red contour shows the LCFS from the magnetic reconstruction.

and also the integrated field B_θ during several LCO periods is shown in figures 9(*a*) and (*b*). The orange curve shows the LCO frequency component in the range up to 5 kHz (and from ∼3.7 kHz in the case of the time derivative). The dark yellow curve shows the low-frequency (lowpassed to 20 kHz) envelope of the fluctuation power in the range 20–500 kHz. The fluctuation power is seen to slightly rise (there is a small bump) just before the large burst of fluctuation energy and the large jump in the integrated field. This behavior suggests the presence of precursor-like oscillations.

The cross-coherence of the fields measured by other Mirnov coils in the A array with respect to the the MA20 coil was investigated in 40 ms time window where the LCO frequency was the most stable. The measured $\dot{B}_\theta$ fields exhibit a clear $m, n = 0, 0$ symmetric structure of the envelope of the high-frequency oscillations during the LCOs. The component at the LCO frequency, although weaker, exhibits a left–right asymmetry in the cross-phase as seen in figure 9(*c*), propagating from the LFS to the HFS. The coherence between coils in the A and C array points to an $n = 0$ mode structure.

The measured B_θ fields at the LCO frequency are systematically stronger than the B_r fields even in the divertor region where the measured mean (equilibrium) fields have strong radial components near the strike points. This suggests that the magnetic activity associated with the LCO is likely located on a closed field line inside the LCFS.

4. Discussion and conclusions

The oscillation phenomena routinely observed during slow L-H transitions in the COMPASS tokamak was investigated with both ball-pen and Langmuir probes for the first time, offering a direct measurement of the radial electric field without the significant influence of the electron temperature gradient and other fluctuating quantities with high temporal resolution.

The temporal ordering of LCO oscillations on COMPASS and the associated radial electric field and the turbulence intensity is consistent with the type-J LCO observed on HL-2A [19]. The apparent lack of Reynolds-stress-related velocity generation and high correlation of the velocity profile with the pressure profile in the close vicinity of the LCFS is also consistent with the HL-2A type-J observations. In the state of suppressed turbulence the pressure gradient builds up until some instability leads to its collapse and subsequent ejection of plasma. The turbulence does not recover to L-mode levels, but is suppressed again. The key questions for future studies are which instability triggers the collapse and which mechanism prevents the recovery of L-mode turbulence. It is also important to note that the measured pressure evolution captured only the electron pressure and may not fully reflect the evolution of the ion pressure.

As seen in figure 6, the temporal evolution of a LCO cycle also indicates that there may be several different time scales at play, e.g. the fast velocity slow-down, turbulence rise and the profile ejection are faster than the time scale of the gradual pressure and velocity profile recovery and deterioration in the state of low turbulence. The evolution of the shear is also seen to be slightly different from that of the the average velocity. This result suggests that the usage of the poloidal velocity instead of its shear in [19] may not be completely valid and likely does not show the whole picture.

A significant difference from the HL-2A observations is that the type-J-like oscillation is observed right after the L-I transition induced by a saw-tooth crash without any preceding type-Y oscillation with significant zonal flow activity in the vicinity of the LCFS as was the case in HL-2A [19].

However, the presented and fully diagnosed discharges represent only a small set within a larger range of parameters where such oscillations are routinely observed. Therefore, other types of dynamics in different COMPASS scenarios cannot be ruled out. It is also possible that such probe measurements only several mm inside the LCFS do not capture important flow dynamics. This point is supported by the Li-BES density profile showing the largest gradient during the LCO cycle several centimeters inside the LCFS.

In a broader sense the results of type-J LCO measurements on HL-2A [19] have been reproduced on COMPASS with the advantage of using ball-pen probes instead of Langmuir probes in order to better separate the electron temperature from the plasma potential. The presented Li-BES profile results also show that further investigations deeper inside the LCFS in the region of the greatest pressure gradient are needed in order to assess the dominant role of either the pressure gradient or zonal flows. This observation of a deep radial extent of the LCO also agrees with the HL-2A results from reflectometry [31]. Finally, these results from a significantly smaller device than HL-2A could be the basis for future scaling analyses.

The magnetic signature observed during the LCO features an asymmetry, but one in the left-to-right direction, whereas on EAST [21], ASDEX Upgrade [20] and the M-mode on JET [22] an up–down asymmetry was observed. The LCO signature in COMPASS appears to be weaker than in ASDEX Upgrade and EAST, but that is likely due to the quite different machine size and correspondingly different density and pressure profiles. The left–right asymmetry should correspond to a pressure gradient modulation according to [23], which further supports the notion that the LCO is controlled by the pressure gradient.

A more detailed analysis in the future including the localization of the magnetic perturbations on a specific flux surface and possibly the tomographic reconstruction of the corresponding current perturbation could offer more insight.

The presence of precursor-like high-frequency oscillations just before the large LCO-frequency modulation suggests that these oscillations may have some physical mechanisms in common with type-III ELMs. Similar 200–300 kHz precursor-like oscillations are commonly observed in regular type-III ELMs on COMPASS [32] and in ASDEX Upgrade [33]. The larger regular density spikes could be a pre-crash rotating mode such as observed on MAST [34]. Unfortunately, the present measurements do not offer sufficient radial resolution for mode structure and movement analysis. The similarity between these LCO and type-III ELMs was also the general conclusion from ASDEX Upgrade [20].

This similarity with type-III ELMs is further supported by the evolution of the density (and pressure) profiles observed by both probes and Li-BES. A slight pedestal is formed in the LCO regime. The collapse of the gradient during the most turbulent phase of the LCO is followed by a fast ‘ejection’ of the profile into the SOL. The density (and pressure) profile evolution observed by Li-BES and probes qualitatively agree in this regard. The I-phase pedestal appears to be smaller than the one in H-mode, which could explain why the observed LCO have a weaker signature in most signals in comparison to routinely observed type-III ELMs. Therefore, the analysis of profile stability might offer additional insights into the triggering mechanism of the oscillations. However, for such an analysis additional discharges are necessary in order to obtain a sufficiently large dataset of Thomson scattering pressure profiles. The recent installation of 2 additional lasers [35] will also favor the collection of such a dataset.

While the modified Reynolds stress probe head offers the possibility to directly measure electric fields, it cannot directly measure the radial derivates of these fields and derived quantities of interest (such as the Reynolds stress power). Therefore, a different rake probe head design capable of such measurements is envisioned for future campaigns.

The conditionally-averged Li-BES profile evolution qualitatively agrees with that observed by the probes. However, a more detailed study and comparison of the dynamics observed by both diagnostics is still ongoing and will be the subject of a future publication. It will also focus on the frequency scaling

of the LCO, particularly with respect to the edge density measured by the Li-BES system.

The continuing investigation of this phenomena in the COMPASS tokamak and particularly the extension of the radial range of the analysis and the dependence on various parameters such as the plasma shape, density, proximity to the L-H threshold, etc is planned as part of the dedicated L-H transition experiments in the year 2018.

Acknowledgments

We thank Carlos Hidalgo for valuable discussions on the probe head design and Istvan Cziegler for detailed discussions on LCO physics and Peter Manz for discussion on the LCO magnetic component. This work received funding from the Czech Science Foundation projects GA16-25074S and GA15-10723S, MEYS projects 8D15001 and LM2015045 and grant no. SGS17/138/OHK4/2T/14 of the Grant Agency of the Czech Technical University in Prague. This work has been carried out within the framework of the EUROfusion Consortium and has received funding from the Euratom research and training programme 2014–2018 under grant agreement No 633053. The views and opinions expressed herein do not necessarily reflect those of the European Commission.

ORCID iDs

O. Grover https://orcid.org/0000-0002-7695-8050
J. Krbec https://orcid.org/0000-0002-3780-6257

References

[1] Wagner F. *et al* 1982 *Phys. Rev. Lett.* **49** 1408–12
[2] Wagner F. 2007 *Plasma Phys. Control. Fusion* **49** B1
[3] Doyle E.J. *et al* 2007 *Nucl. Fusion* **47** S18
[4] Itoh K., Itoh S.I. and Fujisawa A. 2013 *Plasma Fusion Res.* **8** 1102168
[5] Kim E.J. and Diamond P.H. 2003 *Phys. Rev. Lett.* **90** 185006
[6] Miki K., Diamond P.H., Gürcan O.D., Tynan G.R., Estrada T., Schmitz L. and Xu G.S. 2012 *Phys. Plasmas* **19** 092306
[7] Diamond P.H., Itoh S.I., Itoh K. and Hahm T.S. 2005 *Plasma Phys. Control. Fusion* **47** R35
[8] Diamond P.H. and Kim Y.B. 1991 *Phys. Fluids* B **3** 1626–33
[9] Hidalgo C. *et al* 2000 *Plasma Phys. Control. Fusion* **42** A153
[10] Manz P., Xu M., Fedorczak N., Thakur S.C. and Tynan G.R. 2012 *Phys. Plasmas* **19** 012309
[11] Tynan G. *et al* 2013 *Nucl. Fusion* **53** 073053
[12] Schmitz L. 2017 *Nucl. Fusion* **57** 025003
[13] Estrada T., Happel T., Hidalgo C., Ascasíbar E. and Blanco E. 2010 *Europhys. Lett.* **92** 35001
[14] Schmitz L., Zeng L., Rhodes T.L., Hillesheim J.C., Doyle E.J., Groebner R.J., Peebles W.A., Burrell K.H. and Wang G. 2012 *Phys. Rev. Lett.* **108** 155002
[15] Conway G.D., Angioni C., Ryter F., Sauter P. and Vicente J. 2011 *Phys. Rev. Lett.* **106** 065001
[16] Cziegler I., Tynan G.R., Diamond P.H., Hubbard A.E., Hughes J.W., Irby J. and Terry J.L. 2014 *Plasma Phys. Control. Fusion* **56** 075013
[17] Kobayashi T. *et al* 2014 *Nucl. Fusion* **54** 073017
[18] Cavedon M., Pütterich T., Viezzer E., Birkenmeier G., Happel T., Laggner F.M., Manz P., Ryter F., Stroth U. and The ASDEX Upgrade Team 2017 *Nucl. Fusion* **57** 014002
[19] Xu Y. *et al* 2015 *Plasma Phys. Control. Fusion* **57** 014028
[20] Birkenmeier G. *et al* 2016 *Nucl. Fusion* **56** 086009
[21] Xu G. *et al* 2014 *Nucl. Fusion* **54** 103002
[22] Solano E.R. *et al* 2017 *Nucl. Fusion* **57** 022021
[23] Manz P. *et al* (The ASDEX Ugrade Team) 2016 *Phys. Plasmas* **23** 052302
[24] Pánek R. *et al* 2016 *Plasma Phys. Control. Fusion* **58** 014015
[25] Xu G.S. *et al* 2011 *Phys. Rev. Lett.* **107** 125001
[26] Grover O., Adamek J., Seidl J., Devitre A., Sos M., Vondracek P., Bilkova P. and Hron M. 2017 *Rev. Sci. Instrum.* **88** 063501
[27] Adámek J. *et al* 2016 *Rev. Sci. Instrum.* **87** 043510
[28] Weinzettl V. *et al* 2011 *Fusion Eng. Des.* **86** 1227–31
[29] Anda G. *et al* 2016 *Fusion Eng. Des.* **108** 1–6
[30] Seidl J. *et al* 2017 *Nucl. Fusion* **57** 126048
[31] Cheng J. *et al* 2014 *Nucl. Fusion* **54** 114004
[32] Seidl J., Vanovac B., Adamek J., Horacek J., Dejarnac R., Vondracek P., Hron M. and The COMPASS Team 2014 *41st EPS Conference on Plasma Physics* (*Europhysics Conf. Abstracts* vol 38F) (Mulhouse: European Physical Society) (http://ocs.ciemat.es/EPS2014PAP/pdf/P5.059.pdf)
[33] Mink F., Wolfrum E., Maraschek M., Zohm H., Horváth L., Laggner F.M., Manz P., Viezzer E., Stroth U. and The ASDEX Upgrade Team 2016 *Plasma Phys. Control. Fusion* **58** 125013
[34] Kirk A., Dunai D., Dunne M., Huijsmans G., Pamela S., Becoulet M., Harrison J., Hillesheim J., Roach C. and Saarelma S. 2014 *Nucl. Fusion* **54** 114012
[35] Weinzettl V. *et al* 2017 *J. Instrum.* **12** C12015

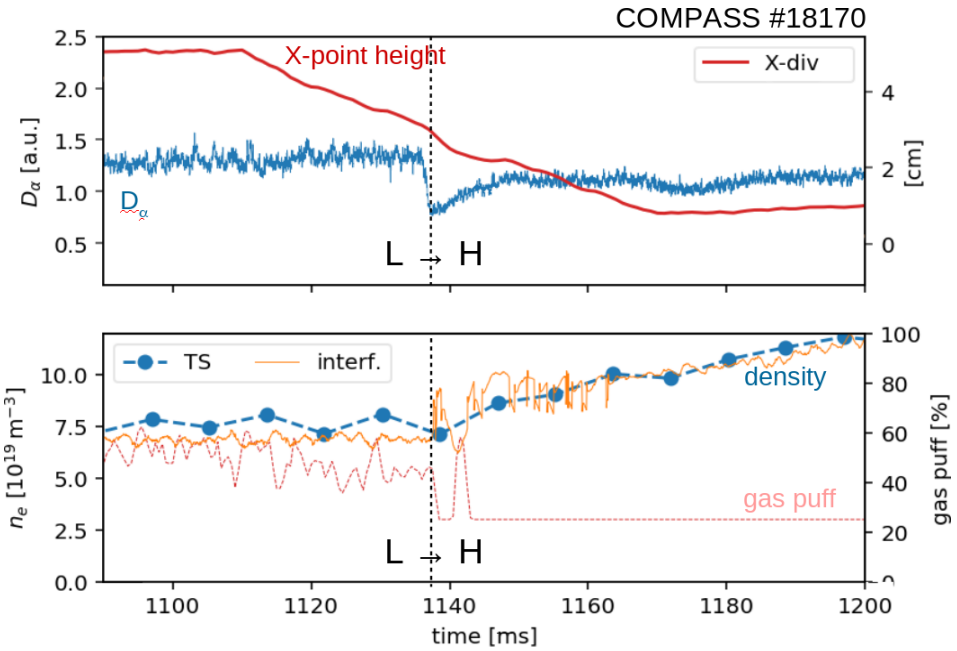

Figure 3.2: Temporal evolution of the X-point height above the divertor, D_α line emission, line-averaged electron density measured by Thomson Scattering (TS) and interferometry and gas puff level in COMPASS discharge #18170. The discharge was performed with a constant plasma current $I_p = 210$ kA and on axis toroidal magnetic field strength $B_t = 1.15$ T.

3.1.2 Dependence on the X-point position

The author contributed to the planning, execution and subsequent analysis of the dependence of P_{LH} on the X-point position in the scope of the wider grant focusing on the impact of high-file-side error field on enhanced confinement. The strong dependence of P_{LH} on the X-point height above the divertor has been known for some time [120]. The author focused on carefully investigating the dependence by performing discharges with the X-point position being ramped from a high position to a lower one at constant plasma current. A typical evolution of such a discharge is shown in Figure 3.2 where at a constant plasma current (and thereby roughly constant ohmic heating) the X-point height above the divertor was ramped down until an L-H transition occurred. The transition can be clearly seen from the drop in D_α line emission and also a steep increase in density to which the feedback system reacts by stopping gas puffing. The plasma current was scanned discharge-by-discharge in the range from 170 to 230 kA at a magnetic field of 1.15 T at densities around $7 \cdot 10^{19}\,\mathrm{m}^{-3}$. This resulted in a scan of ohmic heating power since no NBI was used.

The scan revealed a significant linear dependence with a slope of about 45 kW additional loss power required for an increase of 1 cm in the X-point height above the divertor. The observed P_{LH} was corrected for density variation by normalizing the values by the density dependence in (1.3) discussed in subsection 2.2.1, because these densities in COMPASS correspond to the

high density branch. Unexpectedly, a series of discharges at higher currents appeared to have a similar trend but with a significant offset. Later it was discovered that these discharges had $q_{95} \approx 3$ suggesting that a (perhaps intrinsic) resonant perturbation or tearing mode may be degrading the gradients forming in the pedestal region, therefore, requiring greater loss power to achieve the sufficient gradients.

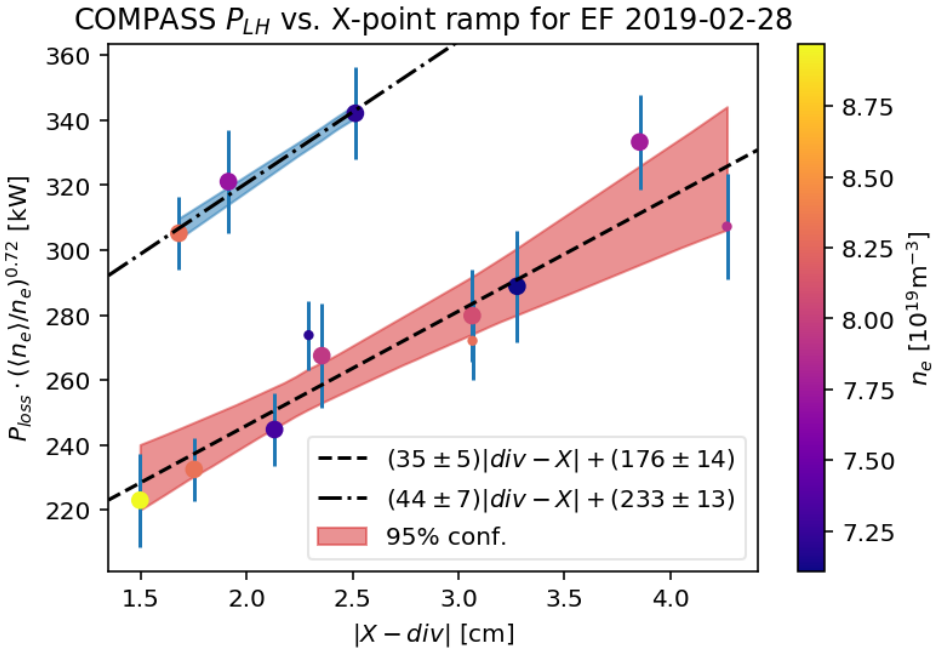

Figure 3.3: L-H power threshold dependence (normalized by the density density dependence in the high-density branch) on the (closest) X-point distance to the divertor. The discharges with greater offset in the trend have $q_{95} \approx 3$.

A series of discharges with different, constant X-point heights at the same ohmic heating power and densities were performed on order to capture the changes in the radial electric field with the changing X-point height above the divertor. The results shown in Figure 3.4 revealed that the poloidal velocity shear increases as the X-point comes closer to the divertor. The increased shear would make the L-H transition easier, which could explain the power threshold at lower X-point heights observed in Figure 3.3. The shear inside and outside the LCFS is also strongly correlated, suggesting that the SOL determines the inner shear, because the core parameters remained the same. These observations are generally in line with the theoretical EDGE2D-EIRENE simulations [44] discussed in subsection 3.1.2. However, additional modeling using codes such as SOLPS or EDGE2D-EIRENE of these COMPASS discharges is required to explain the difference in the SOL parameters in response to the change in the X-point geometry.

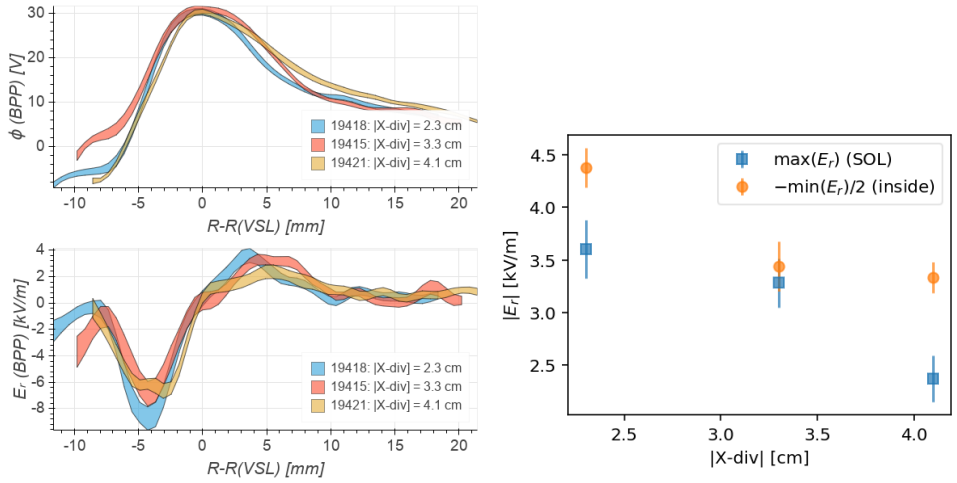

Figure 3.4: Electric potential and radial electric field E_r profiles measured by a reciprocating ball-pen (BPP) probe in discharges with the same hating power and density but different X-point heights above the divertor. It can be clearly seen that the E_r (and therefore also poloidal velocity) shear increases as the X-point comes closer to the divertor.

3.2 First-principles model of pressure relaxation LCO in tokamaks

The large body of research which observes ballooning-like LCO motivated the international effort to develop a scaling for this type of LCO spearheaded by the author of this thesis. While this type of LCO cannot shed light on the role of zonal flows in the L-H transition, it was hoped that the development of a physical model for such LCO could present a way to further differentiate them from the other zonal-flow LCO kind and possibly to offer insights into other mechanisms impacting the L-H transition.

The scaling presented in the article draft to be submitted to Physical Review Letters at the end of this section is based on the extension of the theory in [117] for the LCO frequency and magnetic signature. The original theory over-predicted the observed frequencies and had the opposite (i.e. proportional to) temperature dependence that that observed (inverse) in the experiment [69]. Furthermore, there was no inverse density dependence as observed in the experiments [69, 65].

The final formula derived from a first-principle system of equations based on the DALF system described in section 2.3 systematically predicts the frequency of late limit cycle oscillations with an up-down toroidal current asymmetry. The frequency scaling shows a strong dependence on the machine size, adding further to the evidence that these kinds of limit cycle oscillations are not due to a predator-prey coupling of turbulence with zonal flows but simply the result of a periodic relaxation of the pressure gradient with the time scale determined by the parallel sound speed over the connection length between the inboard and outboard edge plasma with additional coupling to

the Alfvé wave spectrum.

Furthermore, the generalization of the DALF scaling parameters (2.6) to arbitrary ion mass number A and charge Z allowed the author to also describe the scaling for Helium discharges. This generalization was then exploited for the L-H transition model described in subsection 1.2.6 as is further explained in section 3.3.

Experimentally corroborated model of pressure relaxation limit cycle oscillations in the vicinity of the transition to high confinement in tokamaks

O. Grover,[1,2,*] P. Manz,[3,4] A. Y. Yashin,[5] D. I. Réfy,[6] J. Seidl,[1] N. Vianello,[7] G. Birkenmeier,[4] E. R. Solano,[8] M. Sos,[1,2] P. Bohm,[1] P. Bilkova,[1] M. Hron,[1] R. Panek,[1] ASDEX Upgrade Team,[9] COMPASS Team,[10] Globus-M Team,[11] and JET Contributors[12]

[1]*Institute of Plasma Physics, The Czech Academy of Sciences, Prague, Czech Republic*

[2]*Faculty of Nuclear Sciences and Engineering, Czech Technical University in Prague, Czech Republic*

[3]*Institute of Physics, University of Greifswald, Felix-Hausdorff-Str. 6, 17489 Greifswald, Germany*

[4]*Max-Planck-Institute for Plasma Physics, Boltzmannstr. 2, D-85748 Garching, Germany*

[5]*Peter the Great St. Petersburg Polytechnic University, St. Petersburg, Russian Federation*

[6]*Centre for Energy Research, Budapest, Hungary*

[7]*Consorzio RFX, Padova, Italy*

[8]*Laboratorio Nacional de Fusión, CIEMAT, Madrid, Spain*

[9]*See author list of "H. Meyer et al., Nucl. Fusion **59** (2019) 112014"*

[10]*See the author list of "'Overview of the COMPASS results' by M. Hron et al. to be published in Nuclear Fusion Special issue: Overview and Summary Papers from the 28th Fusion Energy Conference (Nice, France, 10-15 May 2021)"*

[11]*See the author list of "'Overview of Globus-M2 spherical tokamak results at the enhanced values of magnetic field and plasma current' by Yu. V. Petrov et al. to be published in Nuclear Fusion Special issue: Overview and Summary Papers from the 28th Fusion Energy Conference (Nice, France, 10-15 May 2021)"*

[12]*See the author list of "'Overview of JET results for optimising ITER operation' by J. Mailloux et al. to be published in Nuclear Fusion Special issue: Overview and Summary Papers from the 28th Fusion Energy Conference (Nice, France, 10-15 May 2021)"*

(Dated: August 11, 2021)

Abstract

An analytical formula systematically predicts the observed frequency of pressure relaxation limit cycle oscillations in the vicinity of the transition to high confinement in 4 tokamaks (JET, ASDEX Upgrade, COMPASS, Globus-M). The experimental dataset spans the widest available range of frequencies, machine sizes and plasma ion species. The machine size dependence is explained by the connection length scale of plasma flows parallel to the magnetic field. The model also explains the observed up-down poloidal current asymmetry and the impact of the plasma ion species mass and charge.

Turbulent transport in magnetized plasmas is considered to be responsible for most of the energy loss in present-day tokamaks on the quest towards a thermonuclear fusion energy source. Therefore, the transition to the High confinement mode (H-mode) [1, 2] in tokamak plasma is a key factor for achieving thermonuclear fusion in future reactors, such as the ITER prototype experimental reactor. However, the conditions necessary for accessing the H-mode are known only empirically with a limited degree of certainty. Therefore, the so called L-H transition to H-mode from the Low confinement mode (L-mode) is an active area of research, focusing on developing a physics model of the transition capable of delivering predictions for ITER and other future reactors.

The L-H transition is characterized by the quenching of turbulent transport due to the formation of a transport barrier in the edge layer of the plasma, leading to reduced losses in comparison to L-mode with severe turbulent transport across the edge layer [2]. However, this quenching process is not always abrupt and under certain conditions may be gradual, accompanied by the phenomena of limit cycle oscillations (LCO) periodically transitioning between a state of strong and quenched turbulent transport [3]. This leads to the typical observations of oscillations in many measured quantities, such as spectral line emissions, edge temperature and density (pressure) and others. One of the most promising models [4, 5] of the L-H transition predicts these oscillations to be the result of a predator-prey-like coupling between turbulence and zonal flows generated by the transfer of momentum and energy [6] from the turbulence by the Reynolds stress [7]. Since the generation of zonal flows is considered to be one of the leading candidates for quenching turbulence in general and possibly during the L-H transition as well, this LCO phenomena offers a promising opportunity to further study the dynamics of the L-H transition in greater detail, and

therefore, has been studied in many tokamaks across the world [8–13].

However, the characteristics of the observed LCO differ between tokamaks. Some experiments found that turbulence suppression by flow generation appears strong enough to trigger a transition into the H-mode [14–17]. Others do not [10, 18**?** –21] and rather observe a behavior closer to type-III edge localized modes (ELMs) where the pressure gradient quasi-periodically relaxes upon reaching a critical threshold [22]. Furthermore, these pressure relaxation LCO are often accompanied by an up-down asymmetric magnetic signature [12, 22–24] and generally exhibit many similar characteristics in JET and ASDEX Upgrade (AUG) [25]. This article only considers the LCO of the second kind, which are typically observed in the "late" stage of the LCO phase close to pure H-mode if both kinds of LCO are observed during a single discharge evolution. Therefore, this Latter aims to provide a model explaining the behavior of these late, pressure relaxation LCO capable of predicting their frequency and magnetic signature, offering a way to further distinguish the late LCO from the "early" LCO possibly dominated by zonal flows.

In the following Letter firstly the model is derived from first-principles-based equations. Subsequently, the eigenfrequency of the model is compared with experimental observations and the underlying dataset described. To put the results into context, the predicted frequency is then compared with a scaling regression and other proposed scalings. Finally, future work and possible improvements to the model are discussed.

The model presented herein extends the theory outlined in [23] which was inspired by the geodesic acoustic mode sideband derivation in the drift-Alfvén wave turbulence (DALF) model [26]. The fundamental model is a linearization of the full DALF model [26, 27], and therefore, represents only the main coupling terms of the limit cycle present in the full model, but does not describe the growth of the underlying instability, though it assumes its presence. This is motivated by the fact that the limit cycle oscillation period of the corresponding square-root Voterra-like predator-prey model [23] is dominated by the coupling terms [28] and coincides with the eigenfrequency of the linearized equations described below.

The model starts with the description of the state of a layer in the edge plasma where an in-out asymmetry in the electron pressure develops after a large transport event on the outer midplane. The asymmetry is described by the term $\langle \tilde{p}_e \cos\theta^* \rangle$ where θ^* is a straight-field-line angle (roughly equivalent to the poloidal angle but accounting for a varying magnetic pitch angle) and $\langle \dots \rangle = \oint \oint \mathrm{d}y \mathrm{d}\theta^*$ signifies a zonal average over the θ^* angle and the binormal

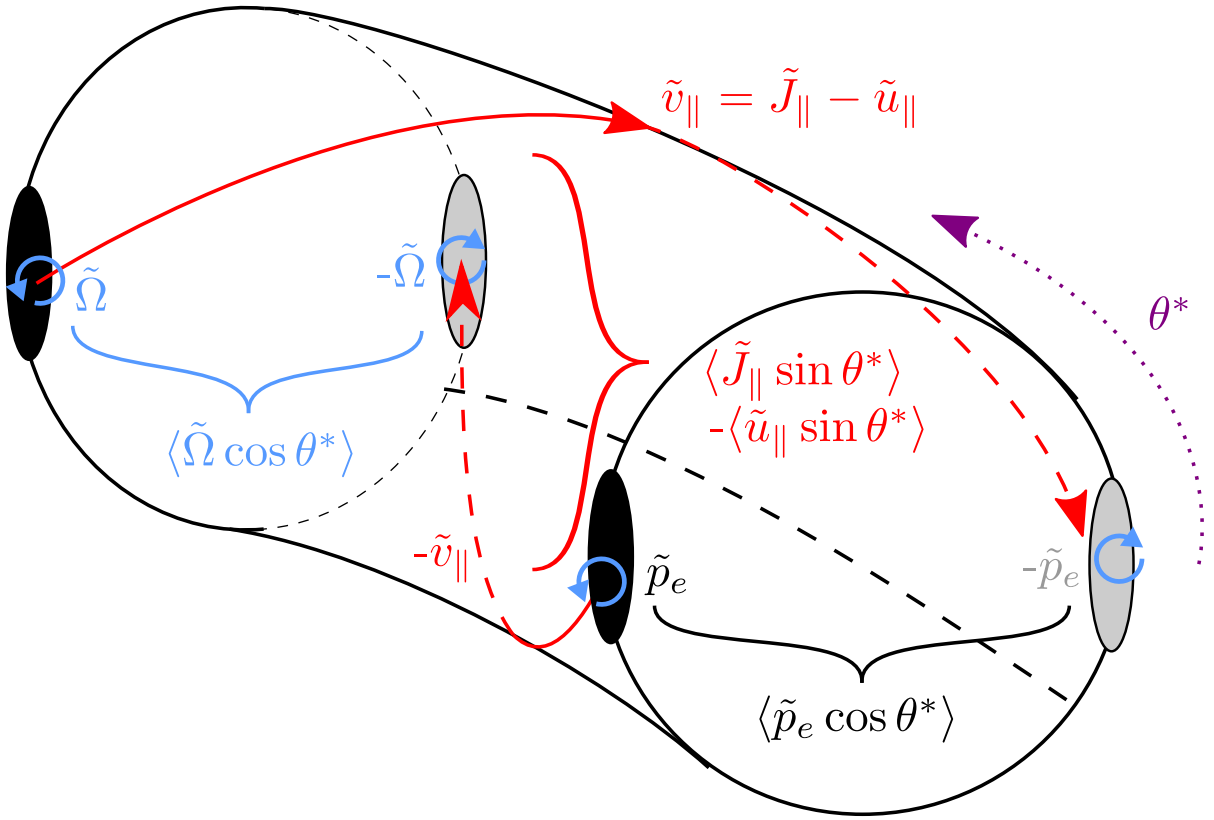

FIG. 1. Sketch of the electron pressure $\tilde{p}_e$ in-out asymmetry being replenished by the up-down asymmetric parallel electron flow $\tilde{v}_\parallel$ decomposed into the ion flow $\tilde{u}_\parallel$ and parallel current $\tilde{J}_\parallel$ up-down asymmetries and the vorticity $\tilde{\Omega}$ asymmetry due to the $\tilde{J}_\parallel$ asymmetry. The asymmetries are represented by sidebands zonally averaged over the straight field line angle θ^* relative to the outer mid-plane.

coordinate y within the layer. The tilde in $\tilde{p}_e$ represents the deviation from the average $\langle p_e \rangle$. Neglecting second-order and curvature terms in Eq. 14 in [23] (as is done also in the other equations below), the evolution of this asymmetry can be described as

$$\frac{\partial}{\partial t}\langle \tilde{p}_e \cos\theta^* \rangle = \langle \tilde{J}_\parallel \sin\theta^* \rangle - \langle \tilde{u}_\parallel \sin\theta^* \rangle \tag{1}$$

where the terms $\langle \tilde{J}_\parallel \sin\theta^* \rangle$ and $\langle \tilde{u}_\parallel \sin\theta^* \rangle$ are the up-down asymmetry in the parallel current and ion flow, respectively. The equation describes the reduction of the electron pressure asymmetry by the replenishing parallel electron flow $\tilde{v}_\parallel$ decomposed into the ion flow $\tilde{u}_\parallel$ and parallel current $\tilde{J}_\parallel$ as sketched in Fig. 1. The estimate in [23] was obtained by

considering only the contribution from the parallel ion flow evolving according to

$$\hat{\epsilon}\frac{\partial}{\partial t}\langle\tilde{u}_\parallel \sin\theta^*\rangle = (1+\tau_i)\langle\tilde{p}_e\cos\theta^*\rangle \tag{2}$$

where $\tau_i = p_i/p_e = T_i/ZT_e$ is the fixed ratio of the ion to electron background pressures with quasineutrality $n_e = Zn_i$ of Z-charged ions and $\hat{\epsilon} = (c_s/L_\perp)^2/(c_s/qR)^2$ is the ratio of the perpendicular and parallel sound transit frequencies with the cold-ion sound speed $c_s = \sqrt{ZT_e/m_i}$ with ion mass m_i and electron temperature T_e in electronvolts, reference safety factor q, major radius R and gradient length-scale $L_\perp$. The coupling of the two equations leads to an up-down asymmetric ion flow driven by the in-out asymmetry in the total pressure. This ion flow reduces the asymmetry, while external heating and fueling is assumed to replenish the average pressure $\langle p_e\rangle$ as well. This results in the original state which is unstable and the ballooning transport creates the asymmetry again. The eigenfrequency of the system of equations (1) and (2) is $\omega_{\mathrm{SSU}} = \sqrt{(1+\tau_i)/\hat{\epsilon}}$ normalized to the perpendicular time scale $L_\perp/c_s$. However, this mechanism also known as the Stringer spin-up (SSU) used in [23] overpredicted the frequency by up to a factor 2 and had a $\sim\sqrt{T_e}$ dependence incompatible with experimental observations, therefore, additional mechanisms which would slow down this dynamic were sought.

One possibility is to include the parallel current term in (1). Neglecting resistivity which has little impact on the result, the parallel current evolves as

$$\frac{\partial}{\partial t}\langle(\hat{\beta}\tilde{A}_\parallel + \hat{\mu}\tilde{J}_\parallel)\sin\theta^*\rangle = -\langle\tilde{p}_e\cos\theta^*\rangle + \langle\tilde{\phi}\cos\theta^*\rangle \tag{3}$$

$$= -(1+\tau_i)\langle\tilde{p}_e\cos\theta^*\rangle + \langle\tilde{W}\cos\theta^*\rangle \tag{4}$$

where the magnetic potential is tied to the parallel current by Ampére's law of induction $-\nabla_\perp^2\tilde{A}_\parallel = \tilde{J}_\parallel$. The first term on the left-hand side represents the current induction and is scaled by the ratio of the perpendicular sound and parallel Alfvén transit frequencies $\hat{\beta} = (c_s/L_\perp)^2/(v_A/qR)^2$ with the Alfvén speed $v_A = B/\sqrt{\mu_0 n_i m_i}$ and the reference on-axis magnetic field strength B. The second term represents electron inertia and is scaled by the ratio of the perpendicular sound and parallel thermal electron transit frequencies $\hat{\mu} = (c_s/L_\perp)^2/(v_e/qR)^2$ with the electron thermal speed $v_e = \sqrt{T_e/m_e}$. The right-hand side represents the difference between the electron pressure and electrostatic potential ϕ which can be also written using the total pressure and the ion flow stream function $W = \phi + p_i$.

However, the easily obtainable coupling of the electron pressure to the current via the electron inertia term also hinted at in [23] only leads to an increase of the resulting frequency into the range of several 100 kHz, far beyond experimental observations. Furthermore, the scaling observed in JET [12] correlated with the poloidal Alfvénic speed which ultimately scales as $\propto 1/\sqrt{\hat{\beta}}$ motivated the focus also on the induction term and the following coupling to an Alfvénic-like wave. The Alfvénic wave arises from the polarization by the parallel current resulting in vorticty $\tilde{\Omega}$ which evolves according to

$$\frac{\partial}{\partial t}\langle\tilde{\Omega}\cos\theta^*\rangle = \langle\tilde{J}_\parallel \sin\theta^*\rangle \tag{5}$$

with the total vorticity defined as $\Omega = (\nabla_\perp^2 W)/B^2$ with the normalized magnetic field strength $B = 1$. The largest contribution in the flux-surface average of the vorticity sideband $\langle\Omega\cos\theta^*\rangle$ is likely to come from the highest perpendicular wavenumber. At the same time, the wavenumber should be below the threshold scale at which the induction is overcome by electron inertia [27] $\rho_s k_{\mathrm{EM}} = \sqrt{\hat{\beta}/\hat{\mu}}$ with the normalization drift scale $\rho_s = c_s/\Omega_i$ and the ion gyrofrequency $\Omega_i = ZeB/m_i$. Additionally, k_{EM} was recently successfully used also to describe the L-H transition in ASDEX Upgrade [29]. Therefore, in the following $k_\perp := k_{\mathrm{EM}}$ is used to approximate the typical Alfvén wave scale present in the model and the Ampere's law is approximated as $A_\parallel \approx J_\parallel/k_{\mathrm{EM}}^2$ and the vorticity as $\Omega \approx -k_{\mathrm{EM}}^2 W$. With these approximations and assumptions the current evolution becomes

$$\frac{\partial}{\partial t}\langle\tilde{J}_\parallel \sin\theta^*\rangle = -\frac{1+\tau_i}{2\hat{\mu}}\langle\tilde{p}_e\cos\theta^*\rangle - \frac{1}{2\hat{\beta}}\langle\tilde{\Omega}\cos\theta^*\rangle \tag{6}$$

If one couples only the current and vorticity in (6) and (5), the eigenfrequency is $\omega_A = 1/\sqrt{2\hat{\beta}}$ in normalized units, which represents and Alfvén wave with $k_\perp = k_{\mathrm{EM}}$ and $qRk_\parallel = 1$. The linear system of equations (1), (2), (6) and (5) has two distinct (in absolute value) eigenfrequencies. For typical experimental values one is in the $\sim$ 100 kHz range, the other in the several kHz range. The low frequency oscillation representing the LCO can be approximated with very high accuracy for typical experimental values as $\omega_{\mathrm{LCO}} = \sqrt{1+\tau_i}/\sqrt{\hat{\epsilon}(1+(1+\tau_i)\hat{\beta}/\hat{\mu})} = \omega_{\mathrm{SSU}}/\sqrt{1+(1+\tau_i)k_{\mathrm{EM}}^2}$ in normalized units. In SI units the predicted frequency is

$$f_{\mathrm{LCO}} = \frac{\sqrt{1+\tau_i}c_s}{2\pi qR\sqrt{1+(1+\tau_i)\frac{m_i}{Zm_e}\beta_e}} \tag{7}$$

with the local dynamic electron plasma beta $\beta_e = \mu_0 n_e T_e / B^2$. There is no $L_\perp$ dependence as it is canceled by the time scale $L_\perp / c_s$ normalization. This formula can be interpreted as the time scale at which the ions equilibrate the asymmetry with the warm-ion sound speed $c_{si} = \sqrt{1+\tau_i} c_s$ over the parallel connection length $L_\parallel \approx \pi q R$ in both directions as in the Stringer spin-up mechanism, but are slowed down by the coupling to the Alfvénic wave represented by $\sqrt{1+(1+\tau_i)k_{\rm EM}^2}$.

The LCO frequency features an isotope-mass dependence between $\sim \sqrt{Z/m_i}$ and $\sim Z/m_i$, its effective power depending on β_e and τ_i. Part of the dependence $\sim \sqrt{Z/m_i}$ originates in c_s, the rest in $k_{\rm EM}$.

The measured LCO frequency $f_{\rm LCO,meas}$ observed in several tokamaks covering a full decade in the frequency range and a wide range of machine sizes as well is shown in Fig. 2 with respect to the frequency predicted $f_{\rm LCO,pred}$ by formula (7). The RMSE with respect to the prediction is 0.48 kHz and $R^2 = 0.79$.

The dominant ordering comes from the strong machine size dependence in in (7). The $\sim 1/m_i$ dependence in (7) explains why Hydrogen discharges have nearly double the LCO frequency in comparison to Deuterium discharges at comparable parameters. Similarly the frequency in tritium discharges is lower than in Deuterium. The $\sim n_e/Z = n_i$ dependence of $k_{\rm EM}$ explains why in Helium the LCO are observed in double the n_e (i.e. the same n_i) yet with comparable frequency to that in Deuterium because of the similar m_i/Z ratio.

In the following the experimental data from each machine are described in more detail. The selected radial locations at which T_e, n_e and q are estimated correspond roughly to the pedestal top where the largest changes during the cycles are observed.

The JET ($R = 2.96$ m) dataset is a subset of the one reported in [12] and uses Thomson scattering data interpolated to $\psi_N \approx 0.95$ where ψ_N is the normalized poloidal flux. The majority of the dataset from ASDEX Upgrade ($R = 1.65$ m) is the same one as previously reported in [22, 23] and represents values of T_e, n_e, q at $\sqrt{\psi_N} \approx 0.95$. Additional discharges representing H and He discharges were added using integrated data analysis [30]. The dataset from COMPASS ($R = 0.56$ m) uses T_e, n_e from the Thomson scattering system [31] and q from the magnetic reconstruction evaluated at $\psi_N \approx 0.95$. The dataset is based on discharges either previously reported in [10] or similar ones. While in [10] a simple up-down asymmetry in the magnetic signature was not found, recently a more complicated signature was discovered. It was found to be a combination of an up-down and $m = 2$

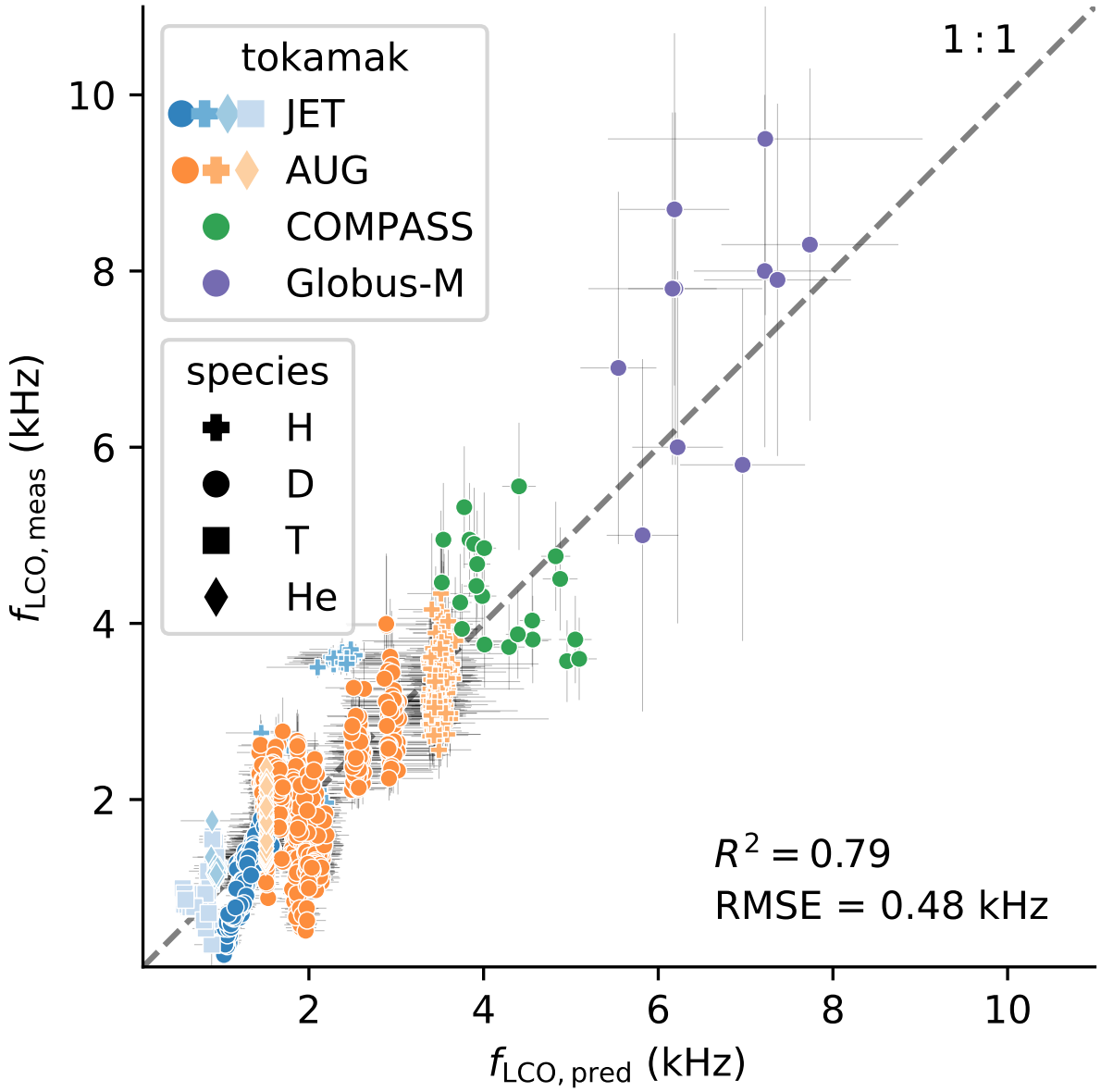

FIG. 2. Experimental pressure relaxation LCO frequency in JET, ASDEX Upgrade (AUG), COMPASS and Globus-M versus the frequency predicted by formula (7). The formula systematically orders the observed frequencies according to the machine size and the main plasma species mass and charge.

asymmetry which has no significant impact on the frequency scaling and will be the subject of a separate publication. The Globus-M ($R = 0.4$ m) dataset is based on Thomson scattering measurements at $r/a = 0.8$ where the fluctuations have the largest amplitude as reported in [11].

The displayed prediction uncertainties correspond to $\sim 95\%$ confidence (i.e. 2 standard deviations) and are based on the uncertainties in the electron temperature and density which are believed to be the dominant source of uncertainty. The uncertainty in the magnetic equilibrium reconstruction is not taken into account. In all cases where τ_i is not known it is assumed to be $\tau_i := 1$. This is the case for the majority of the dataset, with the exception of some ASDEX Upgrade discharges with $\tau_i \sim 1$. Impact of impurities and partial ionization is not considered in the calculation of m_i and Z. However, the uncertainty in all these assumptions is believed to not exceed the displayed uncertainties.

The DALF model upon which this linearized model is based describes only plasmas with a circular cross section, therefore, the model does not explicitly take into account possible effects of plasma shaping. However, using the safety factor q_{95} obtained from magnetic reconstruction as an effective safety factor implicitly includes the impact of elongation and triangularity on the effective connection length.

A powerlaw regression of the dataset in Fig. 2 for R [m], T_e [eV], n_e [$10^{19}\mathrm{m}^{-3}$], B [T], $A = m_i/m_u$ and Z using a generalized linear model (GLM) with Gaussian likelihood and the logarithmic link function results in

$$\begin{aligned} f_{\mathrm{LCO,GLM}} = &\exp(4.3 \pm 0.1) R^{-1.02\pm0.02} B^{1.01\pm0.04} q^{-1.15\pm0.04} \\ &\cdot T_e^{-0.15\pm0.02} n_e^{-0.64\pm0.03} A^{-1.36\pm0.03} Z^{2.2\pm0.1} \end{aligned}$$

with $R^2 = 0.85$ and RMSE=0.41 kHz which is only a marginal improvement over (7). This regression is in very good agreement with (7) which scales for large β_e as

$$f_{\mathrm{LCO,pred}} \propto R^{-1} B^1 q^{-1} T_e^0 n_e^{-0.5} A^{-1} Z^1$$

The difference in the A and Z scaling may come from the comparably small fraction non-Deuterium discharges in the dataset or may represent a hidden $L_\perp$ dependence. The advantage of using a GLM is the minimization of the actual sum of squared errors with respect to the measured values instead of the sum of squared logarithms of the relative errors as with the more common ordinary least squares linear fit in the logarithmic domain. The latter underfits the larger and overfits the smaller frequencies (in R^2 sense) as for them a given relative error permits larger and smaller deviations, respectively. Comparison of the GLM results with other more advanced methods such as geodesic least squares [32] will be the subject of future work.

Finally, the model can be compared with other LCO models and scalings. In the model of limit cycle oscillations induced by a predator-prey coupling of turbulence with zonal flows as in [4] it is not clear how such a strong R dependence would arise.

In comparison to the previously proposed scalings in [22] and [12] which were only empirical and used arbitrary proportionality constants limited to a single machine, the model and the obtained formula (7) is based on first principles and correctly predicts the scaling with machine size as well as the up-down poloidal current asymmetry and the impact of the ion mass and charge.

Formula (7) scales roughly as $\propto I_p/\sqrt{n_i}$ which is very similar to the scaling proposed in [12], however, in contrast to the explanation in [12] of the LCO as a special Alfvén wave, the model here includes an Alfvén wave only in combination with the Stringer spin-up mechanism from [23]. Additionally, the poloidal Alfvén speed scaling proposed in [12] featured a weaker $\sqrt{Z/A}$ dependence.

However, the obtained formula does not exhibit such a strong inverse pressure scaling $\propto 1/\beta_e$ as reported in [22] which may explain the overprediction especially for lower frequencies where the LCO begin to resemble ELMs. Recently in ASDEX Upgrade these LCO have been identified as Type-III ELMs [33] as proposed in [22]. While the derived formula does not completely capture the scaling within a given discharge, it does systematically describe the scaling between different discharges and machines. The reason may be that this linear model does not take into account the evolution of the precursor-like mode often seen to increase transport during the LCO and may further increase the equilibiration time scale. The extension of the linear model by the ballooning instability growth and transport in future work may further improve the scaling.

Although this model does not directly offer insight into the dynamics of the L-H transition, its success at describing the LCO phenomena in its vicinity in various plasma species suggests that the recently proposed model of the L-H transition [29] also based on the DALF model and k_{EM} could be applied even to other plasma species and devices.

This work has been carried out within the framework of the EUROfusion Consortium and has received funding from the Euratom research and training programme 2014-2018 and 2019-2020 under grant agreement No 633053. The views and opinions expressed herein do not necessarily reflect those of the European Commission. This work was co-funded by MEYS projects 8D15001 and LM2018117 and Czech science Foundation project

GA19-15229S and grant no. SGS19/180/OHK4/3T/14 of the Grant Agency of CTU in Prague and Russian Science Foundation project 18-72-10028, https://rscf.ru/en/project/18-72-10028/.

* grover@ipp.cas.cz

[1] F. Wagner, G. Becker, K. Behringer, D. Campbell, A. Eberhagen, W. Engelhardt, G. Fussmann, O. Gehre, J. Gernhardt, G. v. Gierke, G. Haas, M. Huang, F. Karger, M. Keilhacker, O. Klüber, M. Kornherr, K. Lackner, G. Lisitano, G. G. Lister, H. M. Mayer, D. Meisel, E. R. Müller, H. Murmann, H. Niedermeyer, W. Poschenrieder, H. Rapp, H. Röhr, F. Schneider, G. Siller, E. Speth, A. Stäbler, K. H. Steuer, G. Venus, O. Vollmer, and Z. Yü, Regime of Improved Confinement and High Beta in Neutral-Beam-Heated Divertor Discharges of the ASDEX Tokamak, Phys. Rev. Lett. **49**, 1408 (1982).

[2] F. Wagner, A quarter-century of H-mode studies, Plasma Physics and Controlled Fusion **49**, B1 (2007).

[3] L. Schmitz, The role of turbulence–flow interactions in L- to H-mode transition dynamics: recent progress, Nuclear Fusion **57**, 025003 (2017).

[4] E.-J. Kimand P. H. Diamond, Zonal Flows and Transient Dynamics of the L-H Transition, Phys. Rev. Lett. **90**, 185006 (2003).

[5] K. Miki, P. H. Diamond, O. D. Gürcan, G. R. Tynan, T. Estrada, L. Schmitz, and G. S. Xu, Spatio-temporal evolution of the L-I-H transition, Physics of Plasmas **19**, 092306 (2012).

[6] P. Manz, M. Xu, N. Fedorczak, S. C. Thakur, and G. R. Tynan, Spatial redistribution of turbulent and mean kinetic energy, Physics of Plasmas **19**, 012309 (2012), https://doi.org/10.1063/1.3676634.

[7] P. H. Diamondand Y.-B. Kim, Theory of mean poloidal flow generation by turbulence, Physics of Fluids B: Plasma Physics **3**, 1626 (1991).

[8] G. D. Conway, C. Angioni, F. Ryter, P. Sauter, and J. Vicente (ASDEX Upgrade Team), Mean and Oscillating Plasma Flows and Turbulence Interactions across the $L-H$ Confinement Transition, Phys. Rev. Lett. **106**, 065001 (2011).

[9] L. Schmitz, L. Zeng, T. L. Rhodes, J. C. Hillesheim, E. J. Doyle, R. J. Groebner, W. A. Peebles, K. H. Burrell, and G. Wang, Role of Zonal Flow Predator-Prey Oscillations in Triggering the

Transition to H-Mode Confinement, Phys. Rev. Lett. **108**, 155002 (2012).

[10] O. Grover, J. Seidl, D. Refy, J. Adamek, P. Vondracek, M. Tomes, P. Junek, P. Hacek, J. Krbec, V. Weinzettl, M. Hron, and S. Z. and, Limit cycle oscillations measurements with Langmuir and ball-pen probes on COMPASS, Nuclear Fusion **58**, 112010 (2018).

[11] A. Yashin, V. Bulanin, V. Gusev, G. Kurskiev, M. Patrov, A. Petrov, Y. Petrov, and S. Tolstyakov, Phenomena of limit-cycle oscillations in the Globus-M spherical tokamak, Nuclear Fusion **58**, 112009 (2018).

[12] E. R. Solano, N. Vianello, E. Delabie, J. Hillesheim, P. Buratti, D. Réfy, I. Balboa, A. Boboc, R. Coelho, B. Sieglin, S. Silburn, P. Drewelow, S. Devaux, D. Dodt, A. Figueiredo, L. Frassinetti, S. Marsen, L. Meneses, C. Maggi, J. Morris, S. Gerasimov, M. Baruzzo, M. Stamp, D. Grist, I. Nunes, F. Rimini, S. Schmuck, I. Lupelli, C. Silva, and J. contributors, Axisymmetric oscillations at L–H transitions in JET: M-mode, Nuclear Fusion **57**, 022021 (2017).

[13] G. S. Xu, B. N. Wan, H. Q. Wang, H. Y. Guo, H. L. Zhao, A. D. Liu, V. Naulin, P. H. Diamond, G. R. Tynan, M. Xu, R. Chen, M. Jiang, P. Liu, N. Yan, W. Zhang, L. Wang, S. C. Liu, and S. Y. Ding, First Evidence of the Role of Zonal Flows for the $L-H$ Transition at Marginal Input Power in the EAST Tokamak, Phys. Rev. Lett. **107**, 125001 (2011).

[14] P. Manz, G. S. Xu, B. N. Wan, H. Q. Wang, H. Y. Guo, I. Cziegler, N. Fedorczak, C. Holland, S. H. Müller, S. C. Thakur, M. Xu, K. Miki, P. H. Diamond, and G. R. Tynan, Physics of Plasmas **19**, 072311 (2012).

[15] G. Tynan, M. Xu, P. Diamond, J. Boedo, I. Cziegler, N. Fedorczak, P. Manz, K. Miki, S. Thakur, L. Schmitz, L. Zeng, E. Doyle, G. McKee, Z. Yan, G. Xu, B. Wan, H. Wang, H. Guo, J. Dong, K. Zhao, J. Cheng, W. Hong, and L. Yan, Turbulent-driven low-frequency sheared ExB flows as the trigger for the H-mode transition, Nuclear Fusion **53**, 073053 (2013).

[16] Z. Yan, G. R. McKee, R. Fonck, P. Gohil, R. J. Groebner, and T. H. Osborne, Phys. Rev. Lett. **112**, 125002 (2014).

[17] I. Cziegler, G. R. Tynan, P. H. Diamond, A. E. Hubbard, J. W. Hughes, J. Irby, and J. L. Terry, Nucl. Fusion **55**, 0083007 (2015).

[18] T. Kobayashi, K. Itoh, T. Ido, K. Kamiya, S.-I. Itoh, Y. Miura, Y. Nagashima, A. Fujisawa, S. Inagaki, K. Ida, , and K. Hoshino, Phys. Rev. Lett. **111**, 035002 (2013).

[19] J. Cheng, J. Q. Dong, L. W. Yan, K. Itoh, K. J. Zhao, W. Hong, Z. H. Hunang, L. Nie,

T. Lan, A. D. Liu, D. F. Kong, M. Xu, G. R. Tynan, Q. W. Yang, X. T. Ding, X. R. Duan, Y. Liu, and HL-2'A Team, Nucl. Fusion **53**, 093008 (2013).

[20] M. Cavedon, T. Pütterich, E. Viezzer, G. Birkenmeier, T. Happel, F. M. Laggner, P. Manz, F. Ryter, U. Stroth, and T. A. U. Team, Interplay between turbulence, neoclassical and zonal flows during the transition from low to high confinement mode at ASDEX Upgrade, Nuclear Fusion **57**, 014002 (2017).

[21] A. Diallo, S. Banerjee, S. Zweben, and T. Stoltzfus-Dueck, Energy exchange dynamics across l–h transitions in NSTX, Nuclear Fusion **57**, 066050 (2017).

[22] G. Birkenmeier, M. Cavedon, G. Conway, P. Manz, U. Stroth, R. Fischer, G. Fuchert, T. Happel, F. Laggner, M. Maraschek, A. Medvedeva, V. Nikolaeva, D. Prisiazhniuk, T. Pütterich, F. Ryter, L. Shao, M. Willensdorfer, E. Wolfrum, and H. Z. and, Magnetic structure and frequency scaling of limit-cycle oscillations close to L- to H-mode transitions, Nuclear Fusion **56**, 086009 (2016).

[23] P. Manz, G. Birkenmeier, G. Fuchert, M. Cavedon, G. D. Conway, M. Maraschek, A. Medvedeva, F. Mink, B. D. Scott, L. M. Shao, and U. Stroth, Poloidal asymmetric flow and current relaxation of ballooned transport during I-phase in ASDEX Upgrade, Physics of Plasmas **23**, 052302 (2016).

[24] G. Xu, H. Wang, M. Xu, B. Wan, H. Guo, P. Diamond, G. Tynan, R. Chen, N. Yan, D. Kong, H. Zhao, A. Liu, T. Lan, V. Naulin, A. Nielsen, J. J. Rasmussen, K. Miki, P. Manz, W. Zhang, L. Wang, L. Shao, S. Liu, L. Chen, S. Ding, N. Zhao, Y. Li, Y. Liu, G. Hu, X. Wu, and X. Gong, Dynamics of L–H transition and I-phase in EAST, Nuclear Fusion **54**, 103002 (2014).

[25] D. Réfy, E. Solano, N. Vianello, S. Zoletnik, D. Dunai, B. Tál, M. Brix, R. Gomes, G. Birkenmeier, E. Wolfrum, F. Laggner, M. Griener, O. Asztalos, E. Delabie, , and and, Identity of the JET m-mode and the ASDEX Upgrade I-phase phenomena, Nuclear Fusion **60**, 056004 (2020).

[26] B. D. Scott, Energetics of the interaction between electromagnetic ExB turbulence and zonal flows, New Journal of Physics **7**, 92 (2005).

[27] B. Scott, Three-dimensional computation of drift Alfvén turbulence, Plasma Physics and Controlled Fusion **39**, 1635 (1997).

[28] M. Arrigoniand A. Steiner, Square-root models for the volterra equations and the explicit solution of these models, Acta biotheoretica **32**, 123 (1983).

[29] T. Eich, P. Manz, and the ASDEX Upgrade team, The separatrix operational space of ASDEX upgrade due to interchange-drift-alfvén turbulence, Nuclear Fusion **61**, 086017 (2021).

[30] R. Fischer, C. J. Fuchs, B. Kurzan, W. Suttrop, E. Wolfrum, and A. U. Team, Integrated Data Analysis of Profile Diagnostics at ASDEX Upgrade, Fusion Science and Technology **58**, 675 (2010).

[31] P. Bilkova, P. Bohm, M. Aftanas, M. Sos, A. Havranek, D. Sestak, V. Weinzettl, M. Hron, R. Panek, and and, High resolution thomson scattering on the COMPASS tokamak—extending edge plasma view and increasing repetition rate, Journal of Instrumentation **13** (01), C01024.

[32] G. Verdoolaegeand J.-M. Noterdaeme, Robust scaling in fusion science: case study for the lh power threshold, Nuclear Fusion **55**, 113019 (2015).

[33] M. Griener and the ASDEX Upgrade Team, Nuclear Fusion , to be submitted (2021).

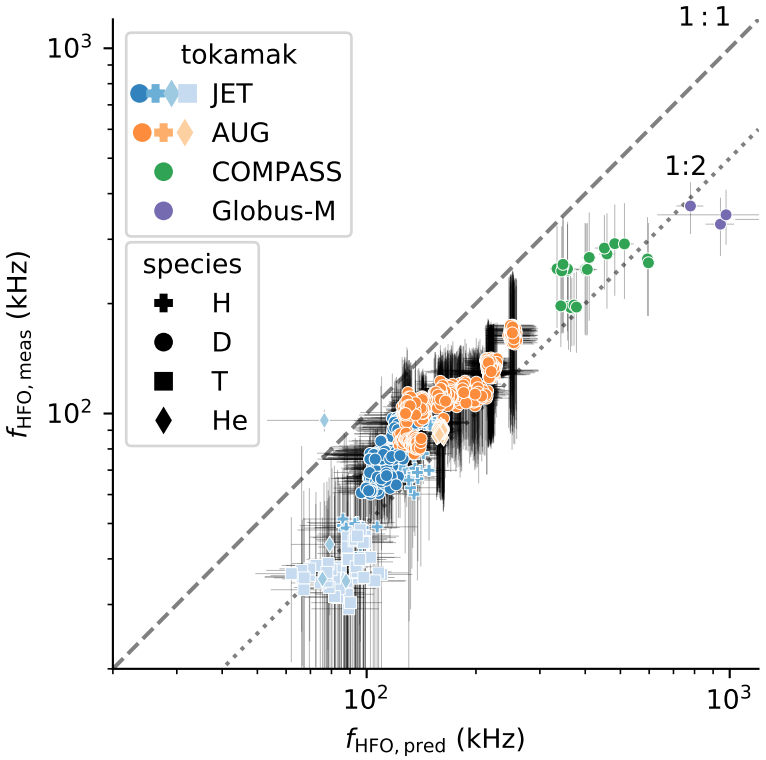

Figure 3.5: Predicted HFO frequency compared with the peak of the HFO spectra observed in magnetics on various devices.

3.2.1 Further extensions of the model

The second eigenfrequency of the system described in section 3.2 could be possibly linked to the observations of high-frequency oscillations (HFO) as reported in [121]. This eigenfrequency can be written as

$$f_{\mathrm{HFO}} = \frac{v_A}{2\pi\sqrt{2}qR}\sqrt{1+(1+\tau_i)k_{\mathrm{EM}}^2} \tag{3.1}$$

with the parameters defined in the draft at the end of section 3.2. Such a dispersion relation would represent a warm-ion kinetic Alfvén wave. However, this formula significantly over-estimates the HFO observations as shown in Figure 3.5 by roughly a factor 2. A closer match is found with the non-kinetic Alfvén wave formula, i.e. when dropping the $\sqrt{1+(1+\tau_i)k_{\mathrm{EM}}^2}$ part in formula (3.1) which is roughly a factor 2.

Nevertheless, the HFO scaling formula without the kinetic coupling enabled the discovery of the HFO in Globus-M where they were previously not identified.

This could be possibly explained by the way the HFO observations are typically done using magnetic coils which are located further away from the plasma. Therefore, they are more likely to see magnetic fluctuations of large scales. Furthermore, the HFOs typically are not a well defined frequency eigenmode but rather a wide spectrum burst event [121]. It is therefore

possible that there are actually such warm-ion kinetic Alfvén waves present in the experiments which also excites a wider spectrum of Alfvén waves, but the magnetic coils at the edge observe the largest power in the lower frequencies of the spectrum which is likely connected with the large-scale waves.

Further study of the HFO including e.g. ECE analysis might provide more information of whether such a picture could be valid.

There is also an ongoing effort to include the $m = 2$ poloidal component in the system of equations. The $m = 2$ component arises from the geodesic component of the curvature operator $\mathcal{K}$ described in section 2.3 $\langle \cos\theta^* \sin\theta^* \partial_x \rangle = \langle \sin 2\theta^* \partial_x \rangle / 2$. By constructing equations for the $m = 2$ sidebands using the $\langle \cdot \sin 2\theta^* \rangle$ products and similar, it is possible to couple such equations back to the $m = 1$ component again through the curvature operator using the identity $\sin x \sin 2x = (\cos x - \cos 3x)/2$ and neglecting the $m = 3$ component. This addition is unlikely to change frequency scaling by much due to the associated prefactor of $(\rho_s / L_\perp)^2 \sim 10^{-4}$, but it could offer provide a more detailed comparison with the magnetic signature seen in the experiment. Additionally, an analogous derivation could be attempted for the GAM sideband balance as done initially in [118] (which in turn inspired this analogous LCO derivation in [117]) which could extend existing GAM scalings.

3.3 Generalization of the separatrix L-H transition model to arbitrary ion mass and charge

The success at describing also Hydrogen and Helium data in the LCO frequency scaling using the DALF scaling parameters led to the idea of applying such generalizations also to the separatrix operational space model [70] in ASDEX Upgrade described in subsection 1.2.6. The original model was developed and tested only with singly charged ions ($Z = 1$) in very pure (low impurity concentration) in Deuterium. In the following article to be submitted to Nuclear Fusion the other DALF scaling parameters such as C representing current resistivity were also generalized to arbitrary ion charge number Z by the author. Great care was taken to explain how Z impacts each parameter of interest. Subsequently the parameters were further generalized by the author to a mixture of ion species using an average ion mass $\bar{A}$ and charge $\bar{Z}$ numbers. The generalization was shown to lead to physically consistent definitions of the cold-ion sound and Alfvén wave velocities.

The author also pointed out the extra factor 2 used in the calculation of k_{EM} in the original work [70] with respect to the correct usage in section 3.2. Therefore, the ratio of $\hat{\beta}$ and $\hat{\mu}$ was renamed to $k_{\mathrm{EM/ES}}$ in the draft sections below to signify this wavenumber represents the "breaking point" between electromagnetic and electrostatic fluctuation scales. For this reason the original k_{EM} wavenumber with the extra factor 2 was renamed to k_{ES} in the article in preparation to signify it represents electrostatic scales. Therefore, the k_{EM} used in section 3.2 is equivalent to $k_{\mathrm{EM/ES}}$ and will be also renamed

in future work for the sake of consistency.

The following two subsections were written nearly exclusively by the author and are part of the article draft to be submitted to Nuclear Fusion.

3.3.1 Ion mass and Charge in interchange-drift-Alfvén turbulence (part of article draft)

In the following we derive how the ion mass $m_i = Am_u$ and charge Z enter the description of interchange-drift-Alfvén turbulence relevant to our study. The controlling scale parameters used in [74, 70] come from the DALF model[114, 115, 116] and were used only with $Z = 1$ in mind. In order to properly describe the full isotope and mass effect they can be generalized to arbitrary Z and A using their original definitions in [114, 116]. The 4 scale parameters with a Z and A dependence are $\hat{\epsilon}$, $\hat{\beta}$, $\hat{\mu}$ and C (Eq. 2.6). Other scale parameters such as the normalized curvature radius ω_B have no Z and A dependence.

While most DALF-related literature also used $Z = 1$, in [24] (chapter 16.2) the main isotope dependence of transport is shown to come from the cold-ion sound speed $c_s = \sqrt{ZT_e/m_i}$ based on DALF-like considerations. Assuming quasi-neutrality $n_e = Zn_i$ the ion pressure is fixed relative to the electron pressure $p_i = \tau_i p_e$ with $\tau_i = T_i/ZT_e$. The warm-ion sound speed is then $c_{si} = \sqrt{1+\tau_i}c_s = \sqrt{(ZT_e + T_i)/m_i}$ following the usual definitions. As c_s cancels in $\hat{\epsilon}$, the parameter $\hat{\epsilon}$ has no Z or A dependence.

The Alfvén speed $v_A = B/\sqrt{\mu_0 n_i m_i} = \sqrt{Z/A}B/\sqrt{\mu_0 n_e m_u}$ depends on Z when one uses the electron density under quasineutrality. Therefore, $\hat{\beta}$ has no explicit Z or A dependence, because the $\sqrt{Z/A}$ dependence present in both c_s and v_A (when using n_e) cancel. On the other hand, the electron thermal speed $v_e = \sqrt{T_e/m_e}$ does not depend on Z or A, and therefore, $\hat{\mu}$ depends on Z and A as $\hat{\mu} \sim Z/A$.

The resistivity parameter C depends on Z as $C \sim Z^{3/2}/\sqrt{A}$ if $\nu_{ei} \sim Z$, because $C \sim \hat{\mu}\nu_{ei}/c_s \sim Z/A \cdot Z/\sqrt{Z/A}$. Furthermore, the numerical constant 0.51 is valid only for $Z = 1$, therefore, for different Z the appropriate Braginski result η_Z should be used.

The characteristic perpendicular wavenumber (normalized to the drift scale $\rho_s = c_s/\Omega_i$ with the ion gyrofrequency $\Omega_i = ZeB/m_i$) at which current induction and electron inertia effects balance $(\rho_s k_\mathrm{EM/ES})^2 = \hat{\beta}/\hat{\mu}$ [114] therefore depends on Z and A as $\rho_s k_\mathrm{EM/ES} \sim \sqrt{A/Z}$. Furthermore, it is useful to consider based on the definitions (2.6) that this wavenumber represents the ratio of the parallel Alfvén and electron thermal time scales or more specifically the ratio of the electron thermal and Alfvén speed $\rho_s k_\mathrm{EM/ES} = v_e/v_A$, i.e. how quickly do electrons move along the field lines relative to ions. Therefore, the Z and A dependence in $k_\mathrm{EM/ES}$ can be also understood to come from the Alfvén speed which includes an implicit Z dependence when using n_e instead of n_i.

Using the considerations above, the parameters can be written in a more practical form from the perspective of comparison to experimental values:

$$\hat{\epsilon} = \frac{(qR)^2}{L_\perp^2} \quad \hat{\beta} = \hat{\epsilon}\beta_{e,d} \quad \hat{\mu} = \hat{\epsilon} Z \frac{m_e}{m_i} \quad C = \hat{\mu}\frac{L_\perp}{c_s}\eta_Z \nu_{ei} \quad (\rho_s k_{\mathrm{EM/ES}})^2 = \beta_{e,d}\frac{m_i}{Z m_e} \tag{3.2}$$

with the so-called dynamic electron beta $\beta_{e,d} = \mu_0 n_e T_e / B^2$ which is proportional (but not equal) to the full plasma beta $\beta = 2(1+\tau_i)\mu_0 n_e T_e / B^2$.

3.3.2 Impact of impurities (part of article draft)

In the presence of impurities one can define an effective ion mass as $m_{i,\mathrm{eff}} = \bar{A} m_u$ with an average mass number weighted by impurity concentration $\bar{A} = \sum n_j A_j / \sum n_j$ over ion densities n_j. The average charge can be defined as $\bar{Z} = \sum n_j Z_j / \sum n_j = n_e / \sum n_j$ with the extended quasineutrality $n_e = \sum n_j Z_j$. Furthermore, collision times generally scale with the parameter Z_{eff} defined by $n_\mathrm{e} Z_{\mathrm{eff}} = \sum_j n_j Z_j^2$.

While the basic DALF model assumes a pure ion fluid, the scaling constants (2.6) calculated with $\bar{A}$, $\bar{Z}$and Z_{eff} can remain useful for the description of turbulence as long as both c_s and v_A still represent the scaling of the sound and Alfvén speeds, respectively, and C describes plasma resistivity in conditions described by $\bar{A}$, $\bar{Z}$and Z_{eff} as is shown below.

The Alfvén speed represents waves where the kinetic plasma pressure periodically equilibrates with the magnetic pressure $\rho_i v_A^2/2 = B^2/2\mu_0$ with the plasma mass density ρ_i, i.e. neglecting the electron mass. In an impure plasma the average mass density can be expressed as $\rho_i = \sum m_u A_j n_j$. In terms of $\bar{A}$, $\bar{Z}$ and n_e it can be expressed as $\rho_i = m_u n_e \bar{A}/\bar{Z}$ which is indeed consistent with the definition $v_A = B\sqrt{\bar{Z}/\mu_0 n_e \bar{A} m_u}$.

The warm-ion sound speed is generally defined as the linearization of the dependence of plasma pressure p on mass density (neglecting electron mass) $c_{si}^2 = \partial p / \partial \rho_i$. Assuming the same ion temperature T_i for all species the total plasma pressure can be expressed as $p = (1+\tau_i)p_e$ with $\tau_i = T_i/\bar{Z}T_e$. Using $\rho_i = m_u n_e \bar{A}/\bar{Z}$ this results in $c_{si}^2 = (1+\tau_i)\bar{Z}T_e/\bar{A}m_u$ which is indeed consistent with the definition of the cold-ion sound speed $c_s = \sqrt{\bar{Z}T_e/\bar{A}m_u}$.

For single charge ions the characteristic electron-ion collision frequency is similar to that of electron-electron collisions $\nu_{\mathrm{ei}} \approx \nu_{\mathrm{ee}}$ and hence often both are used equivalently. The electron-electron Braginskii collision frequency is given by

$$\nu_{\mathrm{ee}} = \frac{4\sqrt{2\pi}}{3} \frac{n_\mathrm{e}\, e^4 \ln\Lambda}{(4\pi\epsilon_0)^2 \sqrt{m_\mathrm{e}}\, T_\mathrm{e}^{3/2}}. \tag{3.3}$$

The term $0.51\nu_{\mathrm{ei}}$ should describe the electric resistivity, which is only valid for single charge ions. To take into account multiple ion species with finite Z_{eff}, the Braginskii result was fitted for $Z_{\mathrm{eff}} = 1, 2, 3, 4$ and ∞ as reported in [74]. This yields

$$\eta_{Z_{\mathrm{eff}}}\nu_{ei} = Z_{\mathrm{eff}}\, f_{Z_{\mathrm{eff}}} 0.51\nu_{\mathrm{ei}}(Z_{\mathrm{eff}} = 1) \simeq Z_{\mathrm{eff}}\, f_{Z_{\mathrm{eff}}} 0.51\nu_{\mathrm{ee}} \tag{3.4}$$

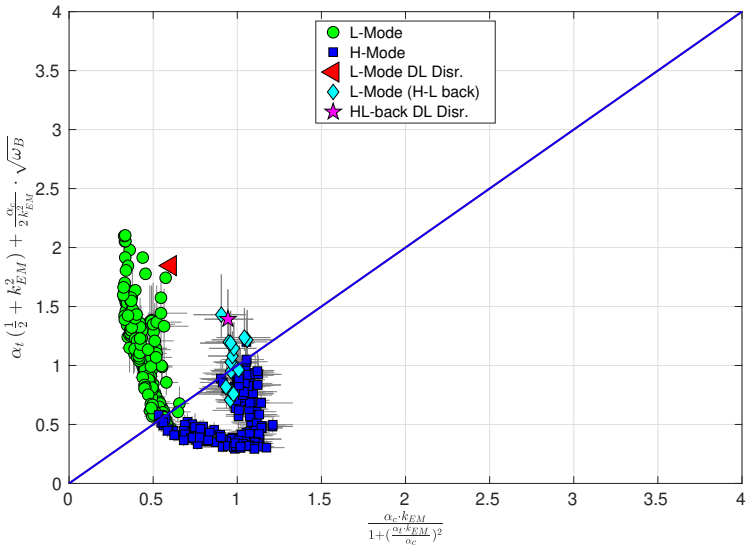

Figure 3.6: Comparison of the H-mode turbulence suppression and growth terms in criterion (1.6) for Helium discharges in ASDEX Upgrade. Data and plot courtesy of Thomas Eich.

where $f_{Z_{\text{eff}}}$ is defined as

$$f_{Z_{\text{eff}}} = (1 - 0.569) \exp\left(-\left(\frac{(Z_{\text{eff}} - 1)}{3.25}\right)^{0.85}\right) + 0.569. \tag{3.5}$$

3.3.3 Ongoing and future work

The generalized scaling parameters were applied through formula (1.6) to the separatrix operational space of ASDEX Upgrade in Hydrogen, Helium and Nitrogen-seeded discharges. Generally very good agreement was found for Helium as shown in Figure 3.6.

Work on Hydrogen and Nitrogen-seeded Deuterium discharges is ongoing, it is complicated by the need for an accurate assessment of the concentration of impurities and Z_{eff} at the separatrix. The $T_e - n_e$ L-H transition boundaries estimated from (1.6) and using (1.5) augmented by the considerations in previous sections for an ASDEX Upgrade-like plasma with $q = 4.5$, $B_t = 2.5$ T, $R = 1.65$ m (like that in Figure 1.5) for several ion species and their mixtures of interest are shown in

The predicted increase of the separatrix T_e in Hydrogen discharges and a slightly lower increase in Helium and slight decrease in an equal Deuterium-Tritium mixture relative to Deuterium is generally consistent with the observations described in subsection 1.2.4, as long as the electron temperature T_e predicted by this model can be used as a proxy for the loss power P_{LH}. No drastic shift in the minimum density is observed for Helium, however, the observation of the line-averaged density density minimum shift in JET [52] cannot be directly compared without a proper estimation of the predicted

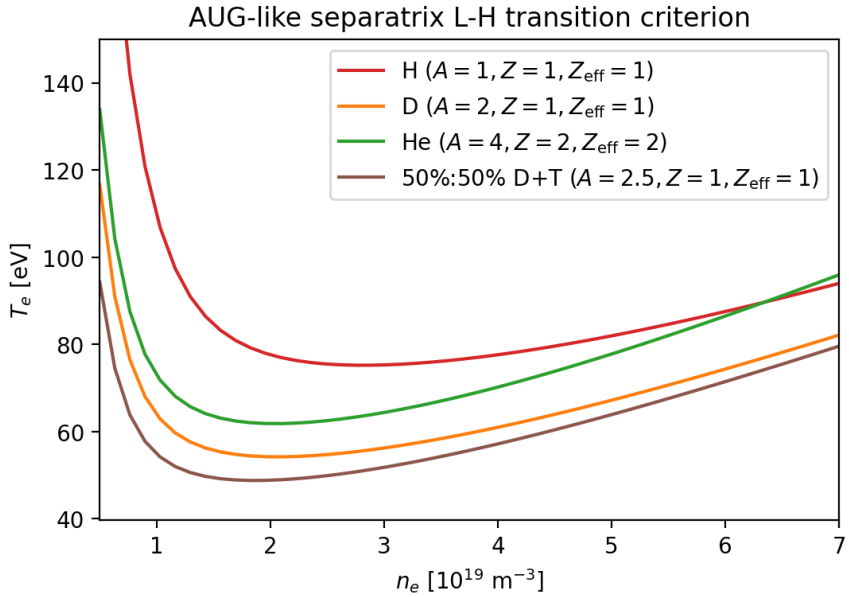

Figure 3.7: Separatrix electron temperature T_e and density n_e at the L-H transition predicted using (1.6) and (1.5) in an ASDEx Upgrade like plasma with $q = 4.5$, $B_t = 2.5$ T, $R = 1.65$ m for plasma species and mixtures of interest.

P_{LH} and $\bar{n}_e$ would be required which would in turn require the knowledge of how e.g. $\bar{n}_e$ and scales with the separatrix n_e in Helium. Nevertheless, the agreement of the observation of LCO in Helium at higher pedestal n_e with the model described in the article draft at the end of section 3.2 suggests that the DALF model's emphasis on the ion density which would be a factor 2 lower in Deuterium at the same $\bar{n}_e$ could be consistent with such observations.

The success of the generalized L-H transition model offers hope that similar predictions could be made also for other devices as well as future reactors such as ITER. In ITER the initial operation phases will likely spend considerable time exploring physics phenomena in Helium and Hydrogen discharges with limited plasma parameters [47]. Therefore, the understanding offered by such a model how to optimize access to H-mode in Hydrogen and Helium may become very valuable. Later, understanding the impact of Deuterium and Tritium mixture ratio may also play an important role in optimizing the ITER operation. However, in order to be fully predictive it will be necessary to obtain good theoretical predictions and/or scalings of the pressure gradient length such as (1.5) wich would be verified also in other tokamaks, because it is crucial for the predictive evaluation P_{LH} using this model as done in [70] for the ASDEX Upgrade Deuterium discharges where such a scaling is known. For instance, there is an ongoing effort to compare and possibly combine the generalized heuristic drift (GHD) [122] model and the turbulence-driven widening [74] model of the SOL fall-off length.

Furthermore, the assumption of the equivalence of the ion and electron temperature profiles should be further investigated. The deeper understanding

of the ion temperature gradient length could possibly also further improve the predictive capabilities of such a model and facilitate a comparison with the ion heat flux model described in subsection 1.2.2.

3.4 I-mode experiments in ASDEX Upgrade

The author took part in the experiments and data analysis at the ASDEX Upgrade tokamak in the scope of the Medium-sized tokamaks work package 1 (MST1) within the topic 4 (5 in the year 2018) and from 2020 of the Work Package Tokamak Exploitation (WPTE) Research Topic 8 (RT08) focusing on natural no-ELM regimes as alternatives to the reference H-mode regime. The main goals of the experiments was to develop a stationary QH-mode and to introduce divertor seeding during I-mode discharges in order to detach the divertor and thereby reduce the heat power loads on the divertor during I-mode bursts. Later experiments studied the dependence of the transition into the I-mode on the magnetic field, plasma current and the edge safety factor. In the most recent WPTE campaign the author proposed his own proposal to search for the I-mode in the favorable ∇B ion drift configuration in order to attempt to reproduce past results in favorable ∇B in Alcator C-mod as noted in section 1.3.

3.4.1 I-mode seeding experiments

In the I-mode seeding experiments within the scope of MST1 different levels of nitrogen puff were applied to a stationary I-mode in reversed B_t/I_p configuration. The goal was to assess the sustainability of the I-mode under seeding conditions and its compatibility with divertor detachment. These experiments intended to follow up on the I-mode seeding experiments performed on Alcator C-mod which have been analyzed only recently [92]. The author was tasked with analyzing poloidal correlation reflectometry [101] data in order to assess the evolution of turbulent fluctuation energy with respect to the introduction of Nitrogen.

As seen in Figure 3.8, the WCM is well visible in the coherence spectrum as a wide band (50 to 150 kHz) after the I-mode regime is entered after 1.75 s. The author developed an algorithm to track the WCM feature in the spectra in order to accommodate the changes in the frequency span and center of the WCM in response to auxiliary heating. The information about the WCM span was then used to characterize the spectrum power distribution as indicated in the left sketch Figure 3.8. Because the total power varies throughout the discharge in response to many actuators such as NBI blips, slight density variation etc., the relative ratios of the power contained in the sketched regions were analyzed for the sake of clarity. Mainly the low-frequency power below the WCM region relative to the total fluctuation power `L/all` was compared with the power in the WCM region above an assumed background turbulence spectrum of with locally fitted powerlaw form `W/(W+P)`. The first nitrogen seeding level from 2.4 s starts a gradual decreasing trend in the ratio of the

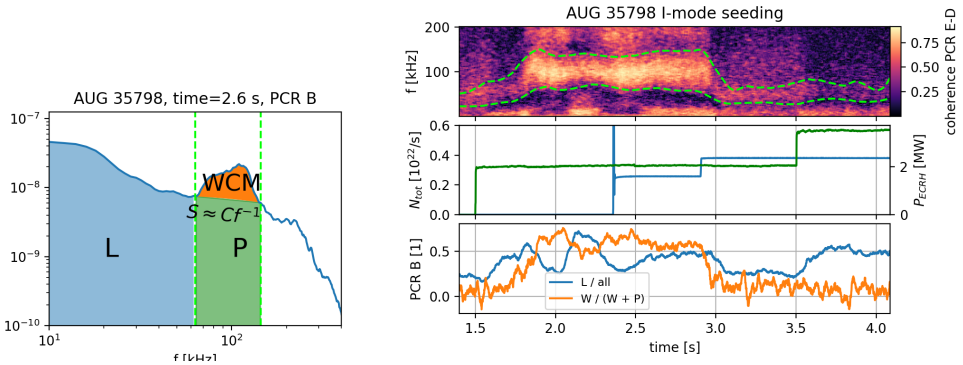

Figure 3.8: Poloidal correlation reflectometry (PCR) fluctuation spectra analysis in seeded I-mode using the spectrum model *(left)* in ASDEX Upgrade discharge 35798. The time-varying WCM spectrum region *(between green dashed lines)* is determined using the coherence of two poloidally separated channels *(*right, top). The different Nitrogen seeding and ECRH heating levels *(right, middle)* are compared with the evolution of the PCR spectrum shape *(right, bottom)*.

fluctuation power in the WCM region. Meanwhile, the low frequency power appears to gradually increase. The second seeding level after 2.9 s prompts a much faster decrease in the WCM power and the WCM and the I-mode are apparently lost when the power ratio reaches L-mode levels around 3 s (as before 1.75 s). A second ECRH step after 3.5 s only increases the low frequency fluctuations relative power and does not recover the WCM or the I-mode.

The edge PCR resonance density layer location varies a little during the discharge as density evolves, which causes the total fluctuation power to vary as well. The use of power ratios mostly removes the impact of such variations. Due to the seeding the L-mode resonance layers before and after the I-mode are not exactly the same, but mostly comparable.

Fortunately, in a later discharge with much higher NBI heating power instead of dominant ECRH it was possible to overcome the degradation of the I-mode with seeding. This effort resulted in a publication [123] co-authored by the author of this thesis summarizing the progress in achieving a stable, detached I-mode regime in ASDEX Upgrade. The author contributed primarily to the analysis of the fluctuation dynamics response to seeding as shown in Figure 8 in the article. Future experiments will aim to build on the success at partial detachment of the I-mode regime with NBI heating.

The experience of observing fluctuation dynamics in the I-mode regime also enabled the author to contribute to the analysis of a simulation model of PREs. This resulted in a publication submitted to Physics of Plasmas authored by Peter Manz and co-authored by the author of the thesis.

3.4.2 I-mode transition power threshold dependence

The discharges for this I-mode study were performed in July 2019 in the scope of MST1 Topic 4. The discharges were executed in an experimental “grid”

of two levels of the plasma current $I_p \in [0.6, 0.8]$ MA and toroidal magnetic field strengths $B \in [1.75, 2.45, 3.14]$ T, resulting in different edge safety factor values q_{95} for nearly each discharge. The goal of this experiment was to asses the effect of B, I_p and q_{95} on the power threshold for the transition from L-mode into the I-mode and also the later transition to H-mode. These discharges had a continuous power ramp in NBI heating in an upper-single null divertor configuration, preventing early H-mode access. For all the discharges the Greenwald fraction was held constant at $n_e/n_{GW} \approx 0.5$ in order to prevent any expected confinement degradation with higher fraction values.

The dataset for the analysis was formed by inspection of the evolution of the total loss power P_{tot} (with NBI shine-through and energy change subtracted), the confined thermal energy W_{th} and the total confinement time $\tau_{E,tot}$ (including fast particles) in these discharges by performing a rolling mean and standard deviation (used as errorbars in the graphs) over 50 ms in order to capture the quasi-periodic variation in the signals. The times of the L-I and I-H transitions at which the rolling mean and st. deviations of the mentioned signals and other global quantities (such as B, I_p, q_{95}, n_e) were selected to be just before any suspicious dips in the signals (likely due calculation errors during transport barrier formation) or changes in the slope of the signals (especially $\tau_{E,tot}$ or W_{th} signifying a confinement change) in order to capture the plasma state just before the transition and remove the effect of imprecise calculations.

Unfortunately, following the considerations described in subsection 2.2.1 it becomes clear that holding $n_e/n_{GW} = 0.5$ amounts to conditioning on the n_e/n_{GW} variable which is a collider and therefore introduces a non-causal relationship between I_p and n. Therefore, I_p becomes a confounder of the effect of q_{95} on P even if it had no direct effect on P itself, because it can have an additional effect through n.

I_p is a root node and has no confounders (causes common with P), so the total effect can be estimated directly without the need for conditioning. However, it is mostly impossible to separate the total effect into the mediation via n_e or q_{95}, because there is not enough n_e variation and conditioning on q_{95} (a collider) would introduce spurious correlations between B_t and

The magnetic field is also a root node and is not confounded by any other causes common with P. Therefore, the total effect (i.e. taking into account also any indirect effects mediated by q_{95} or shaping) can be trivially estimated by regressing P on B_t without any other regressors (i.e. conditioning on other quantities). Conditioning on I_p or n_e would not change the causal dependence structure, but would decrease the number of effective independent samples with respect to the degrees of freedom of the model.

As seen in Figure 3.9, owing likely to the unexplained lower P_{IH} at higher I_p the difference $\Delta P = P_{IH} - P_{LI}$ shows the expected broadening of ΔP with increasing B as discussed in section 1.3 only for the lower currents as shown below. For the higher currents no statistically significant (within errorbars) broadening is observed.

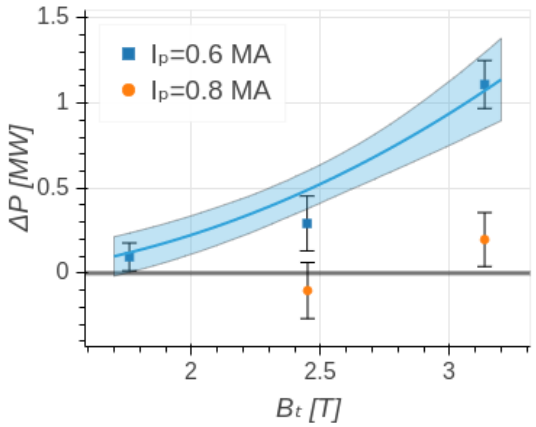

Figure 3.9: Difference in the L-I and I-H transition power thresholds ΔP depending on the magnetic field B_t and the plasma current I_p in ASDEX Upgrade MST1 T04 discharges.

The dependence was further analyzed using powerlaw regression. First the standard approach outlined in section 2.2 was used which resulted in scalings $P_{LI} \propto B^{1.6\pm0.3}$ and $P_{IH} \propto B^{1.5\pm0.3}$ where the errors are 1 standard deviation and the p-values were below 5% (i.e. statistically significant). Therefore, within the uncertainties it was not possible to distinguish the trends which would explain the $\Delta P(B)$ dependence. Regardless, both the observed scalings are stronger than linear which is at odds with the scaling (1.3). This could very likely be due to this analysis estimating only the total effect of B_t variation and not just the direct effect due to the difficulties in separating the q_{95} dependence as discussed above.

In order to reduce the uncertainty and attempt to explain the $\Delta P(B)$ dependence a subset of the discharges $I_p = 0.6$ MA was used with a Bayesian model using the PyMC3 framework [124] for the power law which enables to regress even on a such a small number of points with appropriate prior distributions and can properly take into account the Normal distributions of the uncertainties and errors. This resulted in scalings $P_{LI} \propto B^{1.28\pm0.06}$ and $P_{IH} \propto B^{1.60\pm0.04}$ which are indeed statistically distinguishable within the coefficients' uncertainty and thus can explain the observed $\Delta P(B)$ dependence.

3.4.3 Investigation of the I-mode separatrix operational space

Motivated by the recent success of explaining the H-mode access threshold in ASDEX Upgrade through the separatrix operational space [70] and the recent theory of I-mode access [83] described in section 1.3 a similar effort was undertaken to characterize the I-mode separatrix operational space in ASDEX Upgrade. The initial idea was to verify the operational limits in terms of the separatrix electron dynamic plasma beta β_e and collisionality ν_e^* proposed by the theory. The β_e limit corresponds to $k_{\mathrm{EM/ES}}$ as used in section 3.3. Since the choice of ν_e^* is based on the T_i/T_e ratio dependence in Figure 4.20

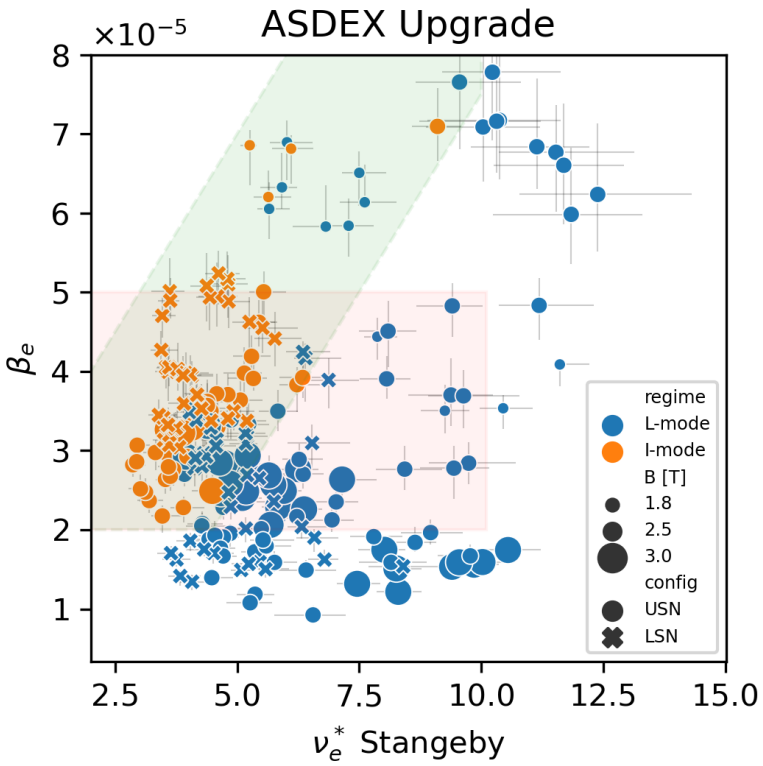

Figure 3.10: Comparison of the L-mode and I-mode existence in the dynamic beta β_e and collisionality (as defined by Stangeby [84]) ν_e^* in ASDEX Upgrade. The red rectangle shows the original I-mode existence boundary proposed in [83], the green region suggests a possible boundary more in line with experimental observations. Separatrix data courtesy of Thomas Eich.

in [84], the definition of collisionality in [84] $\nu_e^* = 10^{-16} n_e L_c / T_e^2$ for electron density n_e [10^{19} m^{-}3] and temperature T_e [eV] with the parallel connection length estimate [m] $L_c \approx \pi q R$ was used. The dataset was obtained using the same analysis technique as used in [74, 70] and section 3.3 which fits the edge Thomson Scattering diagnostic profiles averaged over windows of ~ 300 ms.

While many of the I-mode experiments obtained also an H-mode towards the end of the heating ramp, these H-mode phases were typically too short and non-stationery in order to obtain reliable edge Thomson Scattering profile fits. Therefore, this analysis can reliably determine only the lower boundary of access to I-mode and not the upper limit set by the access to H-mode.

The initial analysis displayed in Figure 3.10 showed that the lower boundary of $\beta_e = 2 \cdot 10^{-5}$ proposed by the theory was indeed quite close to the experimental observations at low collisionality. However, for high collisionality the lower β_e boundary appeared to increase nearly linearly with collisionality. Furthermore, this trend seemed to depend on the magnetic field strength.

A linear dependence between collisionality and β_e suggests the existence of a critical temperature T_e dependent on the magnetic field strength B. If the T_i/T_e ratio would be also determined by ν_e^*, this could correspond to

a critical T_i temperature as well. Unfortunately, without actual T_i profile measurements this cannot be fully distinguished. Generally the experimental observations at least agree with the general idea of the I-mode being accessible only at lower collisionalities.

3.4.4 Search for I-mode in favorable ∇B drift

The main idea of the proposal was to attempt to reproduce the Alcator C-mod results [81] where the I-mode was obtained even in the favorable (for H-mode) ion ∇B drift configuration (i.e. the drift pointing towards the active divertor) in a special plasma shape shown in Figure 3.11. Motivated by the experience in COMPASS of the X-point configuration having a significant impact on the access to H-mode as reported in subsection 3.1.2, such an experiment seemed plausible. The author proposed to try to reproduce such a scenario in ASDEX Upgrade with a similar shape.

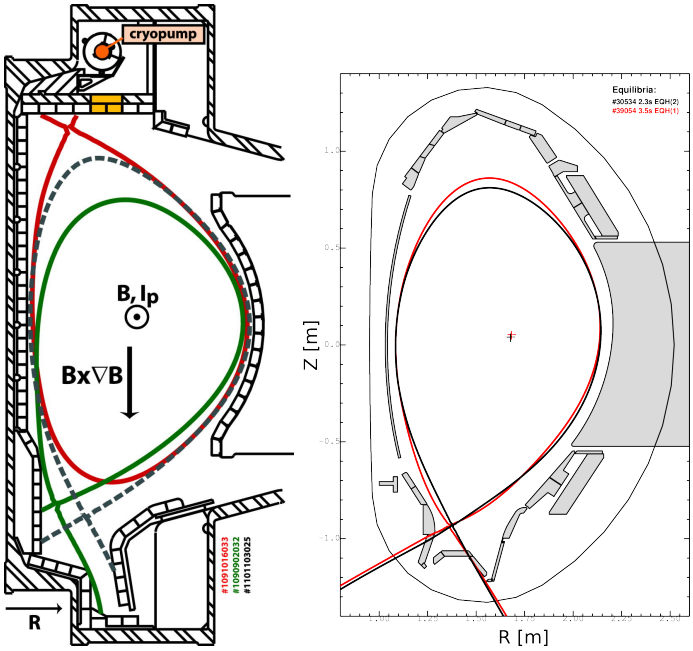

Figure 3.11: Comparison of the special shape in which it was possible to obtain the I-mode in Alcator C-mod with the favorable ∇B drift configuration *(left, green)* reproduced from [81] with permission from AIP and the shape of past PEP-39 "mid X-point" discharge 30534 in ASDEX Upgrade *(right, black)* and the derived new discharge shape in 39054 *(right, red)*

In order to prevent a lengthy scenario development from scratch which would not be possible with the initially allocated discharge budget, the author analyzed old ASDEX Upgrade experiments conducted within the PEP-39 effort studying the impact of the X-point configuration on the access to H-mode. Eventually in 2 past discharges from 2016 with a shape somewhat similar to the target C-mod shape as compared in Figure 3.11 the author found signature similar to an I-mode-like WCM (though at somewhat lower

frequencies just below 100 kHz) in reflectometry during a gradual transition to H-mode. Therefore, the initial experiments attempted to reproduce such a discharge with the same plasma shape but a much slower NBI heating ramp. After initial difficulties with reproducing the same plasma shape with an updated real-time feedback control system, the WCM feature was indeed observed while the plasma entered a state of slightly improved energy confinement as measured by H_{98}.

However, concerns were raised whether this may be only a somewhat irregular I-phase, because the WCM-like feature was observed at frequencies similar to that of the precursor modes in short I-phases preceding the heating ramp. Subsequent dedicated discharges focused on distinguishing these two phenomena. Eventually it became clear that although the frequency ranges of the two phenomena are similar, they are qualitatively different based on correlation ECE results. They also showed that the WCM feature is quite comparable to how the WCM looks in "typical" I-mode discharges in the unfavorable ∇B drift configuration. Furthermore, the impurity confinement time measurements by laser blow-off injection of trace amounts of Ni showed that the I-mode candidate has a significantly higher impurity confinement time. This also suggested that the I-mode candidate is not a typical I-mode with an L-mode-like density and impurity confinement, but rather closer to an H-mode-like confinement in that respect.

Finally, the scenario was tested with initial ECRH steps instead of NBI steps or ramp. The aim was to compare the impact of balanced electron-ion heating versus the possibly dominant ion heating with reduced-voltage NBI in the previous discharges. The time traces from the most successful discharge are shown in Figure 3.12. After an initial L-mode phase the first ECRH step is applied at 2.4 s. Subsequently the WCM-like feature appears in reflectometry and confinement improves. The density and energy confinement improves as seen in the increase of the line-averaged density both in the edge and core. The drop in E_r minimum suggests the edge rotation increases as in H-mode. However, the next laser blow-off injection of Nickel for impurity confinement assessment at 3 s apparently stops this rise reminiscent of an unstable ELM-free H-mode. The impurity injection shows the particle confinement is indeed rather high, more similar to H-mode.

Subsequently the discharge maintains an ELM-free-like H-mode behavior (no large bursts seen in the divertor shunt currents or edge radiation) with the WCM-like feature present all the time. At 4.4 s the $\sim$ 2.5 MW of ECRH heating is replaced with 2.5 MW of NBI heating. Subsequently the discharge features change, there appear more small bursts in edge radiation and the confinement becomes worse. Unfortunately, after 4.65 s a large MHD mode caused possibly the the NBI moment input leads to a general loss of confinement and degradation of the discharge. A subsequent extra ECRH heating step after 4.9 s somewhat recovers this loss and leads to a clear Type-I ELMy H-mode. The WCM-like feature remains observable even during this phase.

Analysis of the separatrix electron and ion temperature and density in the

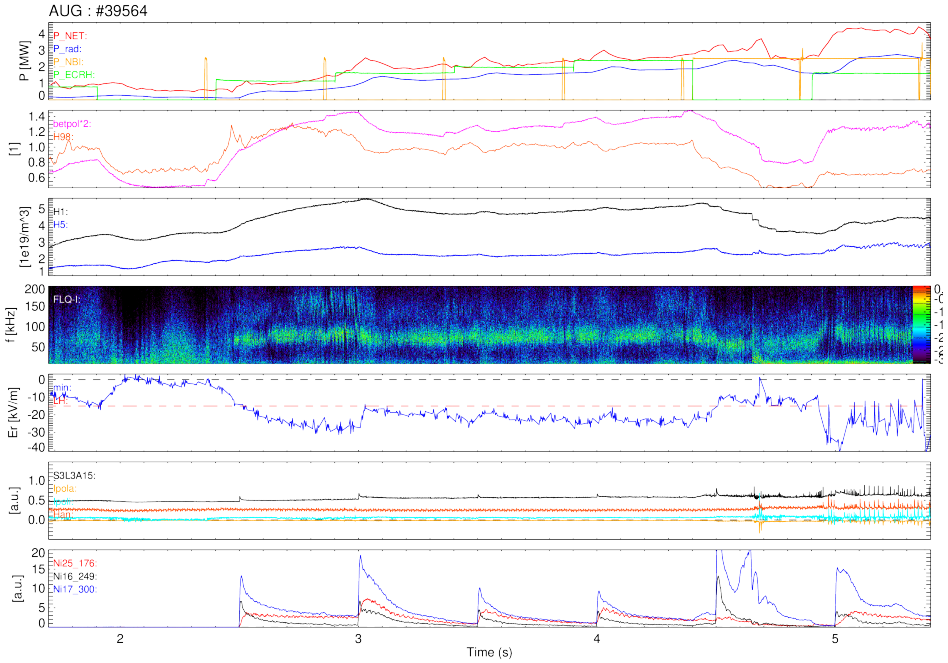

Figure 3.12: Time traces of relevant quantities in ASDEX Upgrade discharge 39564. The first panel from the top shows in order the net loss power, bulk radiation power and total NBI (including blips for T_i measurements) and ECRH input power, all in MW. The second panel gives and indication of the quality of confinement using the poloidal beta β_p (proportional to confined energy) and the confinement improvement factor H_{98}. The third panel shows the evolution of line-averaged density as measured by the core (H1) and edge (H5) interferometer chords. The WCM-like feature is monitored in mid-pedestal density fluctuation spectra measured by the Q-band reflectometry is shown in the fourth panel. The fifth panel shows an estimate of the minimum radial electric field E_r versus the typical values at the L-H transition of -15 kV/m. The absolute value may not be fully representative since old calibration was used, but relative changes are significant. The sixth panel shows the time traces of shunt divertor currents and D_α line radiation as monitors of ELMs and bursts. The final panel shows the line radiation of Nickel impurities introduced into the machine by laser blow-off.

scope of the separatrix operational space model described in subsection 1.2.6 revealed that during most of the ELM-free phase the separatrix electron temperature was just about at the boundary of H-mode turbulence suppression given by (1.6) as shown in Figure 3.13. At the same time, the separatrix ion temperature T_i mapped to the outer midplane appears to be a factor ~ 2 larger. There is uncertainty in the mapping of T_i data to the same separatrix location, but this point is the one measured furthest out anyway, thereby being more of a lower bound. After the transition to clear ELMy H-mode after 4.9 s the (1.6) condition is indeed fulfilled for the electron temperature and the T_i/T_e ratio is reduced as assumed in subsection 1.2.6.

The high T_i/T_e ratio during the ELM-free phase with the WCM-like feature could be consistent with the I-mode access theory described in section 1.3. However, further analysis is needed in order to properly assess the T_i profile and gradient impact on (1.6).

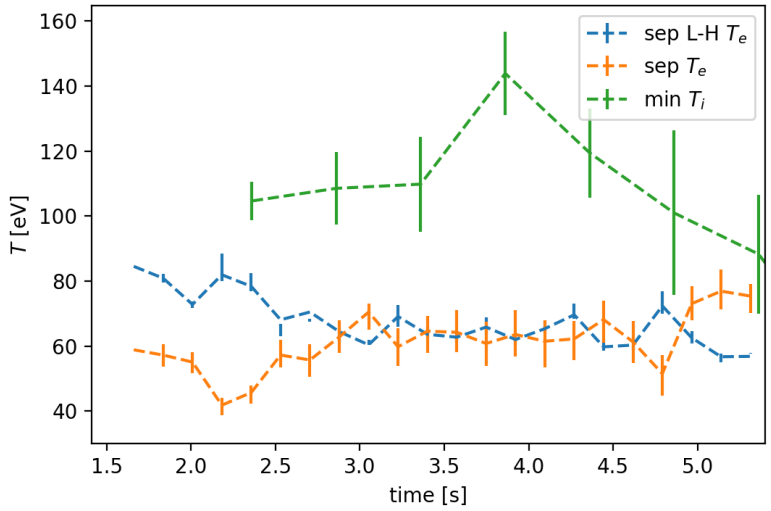

Figure 3.13: Separatrix electron temperature T_e and density n_e and ion temperature T_i (mapped to outer midplane) and the L-H transition T_e predicted by (1.6) evolution in ASDEX Upgrade discharge #39564. Electron separatrix data courtesy of Thomas Eich, ion temperature data courtesy of Eleonora Viezzer.

It is important to note that in all the discharges the bulk plasma radiation was quite high. This may be due to the non-standard plasma shape which leads to heating of first wall components which are not typically under such loads and release impurities. In the future such scenarios could be re-examined after boronization to hopefully mitigate such issues and rule out the possibility that the high radiation losses were simply degrading the H-mode.

Chapter 4

Conclusions and Outlook

Understanding and controlling the transition into enhanced confinement regimes is a necessary ingredient for the success of future fusion power plants. The survey of past work in chapter 1 shows that over the past decades a lot of progress has been made in predicting confinement and power requirements necessary for entering enhanced confinement regimes.

The studies of the transition into the high confinement regime (H-mode) in the COMPASS tokamak described in section 3.1 conducted and analyzed in the scope of this thesis aimed to shed light on the mechanisms leading to the transition through the study of the associated phenomena of limit cycle oscillations. Additionally, the impact of the X-point and divertor configuration on the L-H transition power threshold was carefully analyzed and characterized as shown.

The effort to understand limit cycle oscillations in COMPASS described in subsection 3.1.1 did not result in deeper insight into the role of zonal flows in the L-H transition, because their role in the limit cycle oscillations in the vicinity of the transition appeared to be insignificant. This suggested the L-H transition in COMPASS is dominantly controlled by the pressure-gradient-induced mean flow as is the case also in ASDEX Upgrade and some types of L-H transitions in HL-2A and EAST.

However, the effort has led to the more general undertaking of creating a scaling for these non-zonal-flow-related, pressure relaxation limit cycle oscillations observed in many tokamaks as shown insection 3.2. Through this effort a reduced model, in turn based on the first-principles-based turbulence model DALF, was developed to describe the sideband balance of the parallel current and flows with the pressure and vorticity asymmetry. The resulting scaling covers the widest available range of frequencies, machine sizes and plasma ion species; from one of the smallest tokamaks capable of accessing H-mode (Globus-M) to the largest tokamak in existence at the time of writing (JET); from Hydrogen through deuterium, Tritium to Helium. Additionally, the model also explains the associated magnetic signature asymmetry.

Further extensions to the model discussed in subsection 3.2.1 could provide finer detail for the comparison with the experimentally observed magnetic signature by including the $m = 2$ component, though it is unlikely to improve the frequency scaling itself. A similar analysis could be also done for the

analogous derivation of the Geodesic acoustic mode and perhaps extend existing frequency scalings. Inclusion of the ballooning transport terms in the model promises the greatest chance of improving the frequency scaling of the limit cycle oscillations and could perhaps even extend to Type-III edge localized modes. This will require further analysis of the pressure gradient length in discharges where such measurements are available.

Even though the pressure limit cycle oscillation model did not offer direct insight into the dynamics of the transition to the high confinement regime, its extension to arbitrary main ion species proved very valuable for the generalization of the separatrix operational space model which is also derived from the same DALF model described in section 2.3. The generalization of the DALF scaling parameters to mixtures of ion species shown in section 3.3 provides an opportunity to describe the L-H transition including the isotope effect and possibly even the impact of impurity seeding using a model derived from first principles.

However, in order for this model to be fully predictive towards future reactors such as ITER, a scaling or an extension of the model will have to be developed for the pressure gradient length scale. Furthermore, the assumption of the equivalence of the ion and electron temperature gradients needs to be tested and possibly another scaling or reduced model for the description of the ion temperature profile may need to be developed as well.

The investigation of the I-mode confinement regime in the ASDEX Upgrade tokamak shows some progress towards determining its compatibility with reactor-relevant parameters. While the impurity seeding of I-mode has been found to degrade it as shown in subsection 3.4.1, further experiments with dominant neutral beam injection heating showed that in principle it is possible to achieve a detached stationary I-mode.

The study of the I-mode power threshold access dependence on the magnetic field, plasma current and the edge safety factor discussed in subsection 3.4.2 was unfortunately determined to be inconclusive due to the experimental design of the study which did not take into account confounding by density through the conditioning on fixed Greenwald fractions. In future experiments the methodology of causal graphical and structural models could offer a way to prevent common sources of confounding or collider conditioning bias by e.g. appropriately varying the plasma shape as explained in subsection 2.2.1. Causal graphical models can also help in separating indirect and direct effects of varying certain quantities and thereby possibly shed light on physical mechanisms.

An alternative approach to the the study of the I-mode existence parameter space based on theoretical considerations described in Figure 3.10 revealed that the separatrix boundary conditions derived from simulations partially agree with the conditions observed in experiments. However, the collisionality as a proxy for the ion temperature decoupling from the electron temperature does not appear to be the best possible quantity of interest. Further experiments focusing on the behavior of the ion and electron temperatures and their gradients are required in order to fully assess this theory.

The robust experimental observations with unique probe measurements of the impact of the X-point position within the divertor region on the L-H power threshold in COMPASS and the electric field profile shown in subsection 3.1.2 offer an opportunity to explain such dependencies observed also in other devices. However, ongoing SOLPS-ITER simulations and a wider team effort in progress are required to arrive at conclusive results.

The X-point position within the divertor region in the ASDEX Upgrade was found to have significant impact on suppressing typical access to H-mode and achieving a Type-I edge-localized-mode-free regime as shown in subsection 3.4.4, reminiscent of an I-mode even in the favorable ∇B ion drift direction in terms of featuring a weakly-coherent-like turbulent spectrum. However, the H-mode-like density confinement suggests that this is not a typical I-mode. In this sense this is only a partial reproduction of similar results of I-mode access in the Alcator C-mod tokamak in the favorable ∇B ion drift direction configuration. Future analysis and experiments are needed to further compare these results with those from C-mod and to determine the compatibility of this edge-localized-mode-free regime with reactor-relevant conditions.

4.1 General conclusions and summary

To summarize and generalize the aforementioned conclusions and outlook, the comparison of experimental data from several tokamaks with reduced models based on the DALF turbulence model suggests that parallel flows and current governed by the sound speed and Alfvén parallel scales play an important role in determining the physics of accessing enhanced confinement regimes.

The good agreement of the experimental data from the vicinity of the separatrix with the models and the robust experimental observation of the impact of the divertor and X-point configuration on the access to enhanced confinement points to the confined plasma boundary conditions as the key to understanding and controlling access to enhanced confinement in the studied range of parameters.

In order to further corroborate these theoretical considerations and to make them fully predictive it will be necessary to study the impact and scaling of the ion temperature as well as the pressure profile gradient lengths.

4.2 Summary and declaration of direct contributions by the author

The author of this thesis made the following significant, direct contributions to the results of collective scientific work:

- section 3.1: preparation, execution and analysis of experiments in the COMPASS tokamak dedicated to the study of the L-H transition and LCO, subsequent article [63] conceptualization, writing and probe, magnetics analysis

  certified by Jakub Seidl on behalf of the author team 

- section 3.2: conceptualization, development of new LCO model extension, database compilation and comparison with model, article conceptualization and writing

  certified by Peter Manz on behalf of the author team 

- section 3.3: formula derivation for the generalization of DALF-based separatrix operational space model to arbitrary ion mass and charge, writing of relevant article sections

  certified by Thomas Eich on behalf of the author team 

- section 3.4: conceptualization of power ratio analysis of reflectometry measurements in article [123], I-mode threshold database compilation and analysis, preparation and analysis of I-mode search in favorable ∇B drift experiments

  certified by Tim Happel on behalf of the author team

Acknowledgments

I would like to thank my supervisor-specialist Mgr. Jakub Seidl, Ph.D. for the mentoring and support during the LCO campaigns and interesting discussions about data analysis methods and plasma turbulence; prof. Peter Manz for the fruitful collaboration on the LCO scaling and introducing me to the DALF model; Dr. Tim Happel for the unending support and helpful discussions during all the various experiments in ASDEX Upgrade; Dr. Thomas Eich for the collaboration on the separatrix analysis and model and many discussions; my supervisor Ing. Martin Hron, Ph.D. for cheerful support and helpful discussions and suggestions; and finally the whole COMPASS and ASDEX Upgrade teams, especially operators and session leaders, diagnosticians and technicians, for the barrier-breaking dedication to the experiment and diagnostics design, preparation and maintenance.

This work has been carried out within the framework of the EUROfusion Consortium and has received funding from the Euratom research and training programme 2014-2018 and 2019-2020 under grant agreement No 633053. The views and opinions expressed herein do not necessarily reflect those of the European Commission. This work was co-funded by MEYS projects 8D15001 and LM2018117 and Czech science Foundation project GA19-15229S and grant no. SGS19/180/OHK4/3T/14 of the Grant Agency of CTU in Prague.

Nomenclature

n_e/n_{GW} Greenwald fraction, page 6

α_t normalized collisionality in the DALF model, page 14

β_e dynamic electron beta $\mu_0 n_e T_e/B^2$, proportional (but not equal) to the full plasma beta, page 62

λ_{p_e} pressure gradient length scale, page 14

ν_e^* electron collisionality, ratio of the connection length L_c and the electron-electron collision mean free path, approximated according to Stangeby as $10^{-16} n_e L_c/T_e^2$, page 69

τ_E energy confinement time, page 3

a minor radius, typically half of the width of the LCFS plasma boundary, page 24

$B(, B_t)$ (toroidal) reference magnetic field strength, typically on-axis, in units of tesla, page 23

E_r radial electric field, page 7

H_{98} confinement improvement factor according to the IPB98(y,2) scaling, page 6

k_{EM} $\beta_e m_i/m_e$ characteristic parallel wavenumber normalized to ρ_s. Smaller wavenumbers (larger scales) are more electromagnetic., page 60

L_c parallel connection length, in units of meter, estimated as $\pi q R$, page 69

n_e electron density (or concentration), in units of $10^{19}\,\mathrm{m}^-3$, page 14

$n_{e,min}$ minimum density of the non-monotonic dependence of the L-H transition power threshold on density, page 10

P_{LH} threshold power for the L-H transition, page 9

P_{loss} loss power, includes radiation losses, page 9

q edge safety factor, either the cylindrical approximation for separatrix data or q_{95} for pedestal data, page 25

R major radius, typically the geometric mean of the LCFS plasma boundary, page 24

T_e electron temperature, in units of eV (mean kinetic energy equivalent), page 14

$\bar{A}$ average ion mass number, page 12

ω_B normalized curvature radius in the DALF model, page 26

CGM causal graphical model, page 23

DALF drift-Alfvén wave turbulence model, page 25

ECRH electron cyclotron resonance heating, page 19

EDA H-mode enhanced D_α H-mode regime, page 18

ELM edge localized mode, page 8

ETB edge transport barrier, page 7

GAM geodesic acoustic mode, page 16

GLM generalized linear model, page 22

HFO high-frequency oscillations, page 59

ICRH Ion cyclotron resonance heating, page 20

LCFS last closed flux surface, page 11

LCO limit cycle oscillation, page 13

NBI neutral beam injection, page 19

pedestal shift of the pressure profile due to the narrow edge gradient region, page 7

PRE pressure relaxation events, page 17

QCE quasi-continuous exhaust regime, page 18

QH-mode quiescent H-mode, page 18

separatrix manifold separating open and closed (within the tokamak chamber) field line topologies, page 11

SOL scrape-off layer, page 11

TS Thomson Scattering diagnostic, page 19

WCM weakly coherent mode, page 16

ZF zonal flow, page 12

Bibliography

[1] M. Kikuchi and K. Lackner. *Fusion physics*. Vienna: International Atomic Energy Agency, 2012. ISBN: 978-920-1304-100.

[2] Kai Henrik Nordlund et al. "European research roadmap to the realisation of fusion energy". In: (2018).

[3] Slavomir Entler et al. "Approximation of the economy of fusion energy". In: *Energy* 152 (2018), pp. 489–497.

[4] K. Miyamoto. *Plasma Physics for Controlled Fusion (Springer Series on Atomic, Optical, and Plasma Physics)*. Springer, 2016. ISBN: 978-3-662-49781-4.

[5] J. Wesson. *Tokamaks*. 4th ed. New York: Oxford University Press, 2011.

[6] K. Ikeda. "Progress in the ITER Physics Basis". In: *Nuclear Fusion* 47.6 (2007).

[7] ITER Physics Expert Group on Confinement et al. "Chapter 2: Plasma confinement and transport". In: *Nuclear Fusion* 39.12 (1999), p. 2175.

[8] F. F. Chen. *Introduction to Plasma Physics and Controlled Fusion*. 3rd ed. Springer International Publishing Switzerland: Springer, 2016. ISBN: 978-3-319-22308-7.

[9] Raúl Sánchez and David Newman. "Primer on Complex Systems". In: *A Primer on Complex Systems*. Springer, 2018, pp. 3–39.

[10] J. E. Maggs and G. J. Morales. "Generality of Deterministic Chaos, Exponential Spectra, and Lorentzian Pulses in Magnetically Confined Plasmas". In: *Phys. Rev. Lett.* 107 (18 Oct. 2011), p. 185003.

[11] O. E. Garcia et al. "Stochastic modelling of intermittent fluctuations in the scrape-off layer: Correlations, distributions, level crossings, and moment estimation". In: *Physics of Plasmas* 23.5 (2016), p. 052308.

[12] P. Manz et al. "The diffusion limit of ballistic transport in the scrape-off layer". In: *Physics of Plasmas* 27.2 (2020), p. 022506.

[13] S. Wiesen et al. "The new SOLPS-ITER code package". In: *Journal of Nuclear Materials* 463 (2015). PLASMA-SURFACE INTERACTIONS 21, pp. 480–484. ISSN: 0022-3115.

[14] R Simonini et al. “Models and Numerics in the Multi-Fluid 2-D Edge Plasma Code EDGE2D/U”. In: *Contributions to Plasma Physics* 34.2-3 (1994), pp. 368–373.

[15] E.J. Doyle (Chair Transport Physics) et al. “Chapter 2: Plasma confinement and transport”. In: *Nuclear Fusion* 47.6 (2007), S18.

[16] DC McDonald et al. “Recent progress on the development and analysis of the ITPA global H-mode confinement database”. In: *Nuclear Fusion* 47.3 (2007), p. 147.

[17] Geert Verdoolaege et al. “First Analysis of the Updated ITPA Global H-Mode Confinement Database”. In: *27th IAEA Fusion Energy Conference*. International Atomic Energy Agency. 2018.

[18] H. Yamada et al. “Characterization of energy confinement in net-current free plasmas using the extended International Stellarator Database”. In: *Nuclear Fusion* 45.12 (2005), p. 1684.

[19] Hartmut Zohm. “On the Minimum Size of DEMO”. In: *Fusion Science and Technology* 58.2 (2010), pp. 613–624.

[20] OJWF Kardaun et al. “The tortuous route of confinement prediction near Operational Boundary Improvement of analysis based on ITERH. DB4/L. DB3 database”. In: *21st IAEA Fusion Energy Conference*. International Atomic Energy Agency. 2007.

[21] Martin Greenwald. “Density limits in toroidal plasmas”. In: *Plasma Physics and Controlled Fusion* 44.8 (July 2002), R27–R53.

[22] G. Verdoolaege et al. “The updated ITPA global H-mode confinement database: description and analysis”. In: *Nuclear Fusion* 61.7 (May 2021), p. 076006.

[23] ASDEX Team. “The H-Mode of ASDEX”. In: *Nuclear Fusion* 29.11 (1989), p. 1959.

[24] M Bessenrodt-Weberpals et al. “The isotope effect in ASDEX”. In: *Nuclear Fusion* 33.8 (Aug. 1993), pp. 1205–1238.

[25] F. Wagner et al. “Regime of Improved Confinement and High Beta in Neutral-Beam-Heated Divertor Discharges of the ASDEX Tokamak”. In: *Phys. Rev. Lett.* 49 (19 Nov. 1982), pp. 1408–1412.

[26] J. C. Hillesheim et al. “Stationary Zonal Flows during the Formation of the Edge Transport Barrier in the JET Tokamak”. In: *Phys. Rev. Lett.* 116 (6 Feb. 2016), p. 065002.

[27] Laboratorio Nacional de Fusión, Madrid. *Pedestal*. URL: `http://fusionwiki.ciemat.es/wiki/Pedestal` (visited on 08/18/2021).

[28] R.P. Wenninger et al. “DEMO divertor limitations during and in between ELMs”. In: *Nuclear Fusion* 54.11 (Nov. 2014), p. 114003.

[29] R.A. Pitts et al. “Physics basis for the first ITER tungsten divertor”. In: *Nuclear Materials and Energy* 20 (2019), p. 100696. ISSN: 2352-1791.

[30] C. Silva et al. “Reciprocating probe measurements of ELM filaments on JET”. In: *Plasma Physics and Controlled Fusion* 51.10 (2009), p. 105001.

[31] H. Zohm. “Edge localized modes (ELMs)”. In: *Plasma Physics and Controlled Fusion* 38.2 (1996).

[32] G. T. A. Huijsmans et al. “Modelling of edge localised modes and edge localised mode control”. In: *Physics of Plasmas* 22.2 (2015), p. 021805.

[33] P.B. Snyder et al. “Pedestal stability comparison and ITER pedestal prediction”. In: *Nuclear Fusion* 49.8 (July 2009), p. 085035.

[34] Y. Ma et al. “Scaling of H-mode threshold power and L–H edge conditions with favourable ion grad-Bdrift in Alcator C-Mod tokamak”. In: *Nuclear Fusion* 52.2 (Jan. 2012), p. 023010.

[35] Y R Martin, T Takizuka, and the ITPA CDBM H-mode Threshold Database Working Group. “Power requirement for accessing the H-mode in ITER”. In: *Journal of Physics: Conference Series* 123.1 (2008), p. 012033.

[36] F. Ryter et al. “Experimental evidence for the key role of the ion heat channel in the physics of the L–H transition”. In: *Nuclear Fusion* 54.8 (2014), p. 083003.

[37] P. Gohil et al. “L–H transition studies on DIII-D to determine H-mode access for operational scenarios in ITER”. In: *Nuclear Fusion* 51.10 (Aug. 2011), p. 103020.

[38] C F Maggi et al. “Isotope effects on L-H threshold and confinement in tokamak plasmas”. In: *Plasma Physics and Controlled Fusion* 60.1 (2018), p. 014045.

[39] M. Schmidtmayr et al. “Investigation of the critical edge ion heat flux for L-H transitions in Alcator C-Mod and its dependence on B T”. In: *Nuclear Fusion* 58.5 (2018), p. 056003.

[40] W. Fundamenski et al. “A new model of the L–H transition in tokamaks”. In: *Nuclear Fusion* 52.6 (Apr. 2012), p. 062003.

[41] ASDEX Team. “The H-Mode of ASDEX”. In: *Nuclear Fusion* 29.11 (1989), p. 1959.

[42] F. Ryter et al. “Survey of the H-mode power threshold and transition physics studies in ASDEX Upgrade”. In: *Nuclear Fusion* 53.11 (2013), p. 113003.

[43] C.F. Maggi et al. “L–H power threshold studies in JET with Be/W and C wall”. In: *Nuclear Fusion* 54.2 (2014), p. 023007.

[44] A.V. Chankin et al. “Possible influence of near SOL plasma on the H-mode power threshold”. In: *Nuclear Materials and Energy* 12 (2017). Proceedings of the 22nd International Conference on Plasma Surface Interactions 2016, 22nd PSI, pp. 273–277. ISSN: 2352-1791.

[45] E Righi et al. “Isotope scaling of the H mode power threshold on JET”. In: *Nuclear Fusion* 39.3 (Mar. 1999), pp. 309–319.

[46] F Ryter et al. “L-H transition physics in hydrogen and deuterium: key role of the edge radial electric field and ion heat flux”. In: *Plasma Physics and Controlled Fusion* 58.1 (Oct. 2015), p. 014007.

[47] A. Loarte et al. “H-mode plasmas in the pre-fusion power operation 1 phase of the ITER research plan”. In: *Nuclear Fusion* 61.7 (June 2021), p. 076012.

[48] F. Ryter et al. “H-mode threshold and confinement in helium and deuterium in ASDEX Upgrade”. In: *Nuclear Fusion* 49.6 (May 2009), p. 062003.

[49] D C McDonald et al. “ELMy H-modes in JET helium-4 plasmas”. In: *Plasma Physics and Controlled Fusion* 46.3 (Feb. 2004), pp. 519–534.

[50] Jon Hillesheim et al. “Proc. 26th IAEA Fusion energy Conf.” In: EX/5-2. Kyoto, Japan, 2016.

[51] U. Plank et al. “H-mode power threshold studies in mixed ion species plasmas at ASDEX Upgrade”. In: *Nuclear Fusion* 60.7 (June 2020), p. 074001.

[52] E.R. Solano, G. Birkenmeier, and JET contributors. “L-H transition threshold studies in Helium plasmas at JET”. In: *Nuclear Fusion* (Apr. 2021), submitted.

[53] P. Manz et al. “Spatial redistribution of turbulent and mean kinetic energy”. In: *Physics of Plasmas* 19.1 (2012), p. 012309.

[54] P. H. Diamond and Y.-B. Kim. “Theory of mean poloidal flow generation by turbulence”. In: *Physics of Fluids B: Plasma Physics* 3.7 (1991), pp. 1626–1633.

[55] P. Manz et al. “Zonal flow triggers the L-H transition in the Experimental Advanced Superconducting Tokamak”. In: *Physics of Plasmas* 19 (2012), p. 072311.

[56] Ondrej Grover et al. “First simultaneous measurements of Reynolds stress with ball-pen and Langmuir probes”. In: *Review of Scientific Instruments* 88.6 (2017), p. 063501.

[57] C. Silva et al. “Comparison of fluctuations properties measured by Langmuir and ball-pen probes in the ISTTOK boundary plasma”. In: *Plasma Physics and Controlled Fusion* 57.2 (2015), p. 025003.

[58] J. Adámek et al. “Profile measurements of the electron temperature on the ASDEX Upgrade, COMPASS, and ISTTOK tokamak using Thomson scattering, triple, and ball-pen probes”. In: *Review of Scientific Instruments* 87.4, 043510 (2016).

[59] E.-J. Kim and P. H. Diamond. “Zonal Flows and Transient Dynamics of the L-H Transition”. In: *Phys. Rev. Lett.* 90 (18 May 2003), p. 185006.

[60] K. Miki et al. “Spatio-temporal evolution of the L-I-H transition”. In: *Physics of Plasmas* 19.9 (2012), p. 092306.

[61] G. D. Conway et al. “Mean and Oscillating Plasma Flows and Turbulence Interactions across the $L{-}H$ Confinement Transition”. In: *Phys. Rev. Lett.* 106 (6 Feb. 2011), p. 065001.

[62] L. Schmitz et al. “Role of Zonal Flow Predator-Prey Oscillations in Triggering the Transition to H-Mode Confinement”. In: *Phys. Rev. Lett.* 108 (15 Apr. 2012), p. 155002.

[63] O. Grover et al. “Limit cycle oscillations measurements with Langmuir and ball-pen probes on COMPASS”. In: *Nuclear Fusion* 58.11 (Oct. 2018), p. 112010.

[64] A.Yu. Yashin et al. “Phenomena of limit-cycle oscillations in the Globus-M spherical tokamak”. In: *Nuclear Fusion* 58.11 (Oct. 2018), p. 112009.

[65] Emilia R. Solano et al. “Axisymmetric oscillations at L–H transitions in JET: M-mode”. In: *Nuclear Fusion* 57.2 (2017), p. 022021.

[66] G. S. Xu et al. “First Evidence of the Role of Zonal Flows for the $L{-}H$ Transition at Marginal Input Power in the EAST Tokamak”. In: *Phys. Rev. Lett.* 107 (12 Sept. 2011), p. 125001.

[67] G.R. Tynan et al. “Turbulent-driven low-frequency sheared ExB flows as the trigger for the H-mode transition”. In: *Nuclear Fusion* 53.7 (2013), p. 073053.

[68] M. Cavedon et al. “Interplay between turbulence, neoclassical and zonal flows during the transition from low to high confinement mode at ASDEX Upgrade”. In: *Nuclear Fusion* 57.1 (2017), p. 014002.

[69] G. Birkenmeier et al. “Magnetic structure and frequency scaling of limit-cycle oscillations close to L- to H-mode transitions”. In: *Nuclear Fusion* 56.8 (July 2016), p. 086009.

[70] T. Eich, P. Manz, and the ASDEX Upgrade team. “The separatrix operational space of ASDEX Upgrade due to interchange-drift-Alfvén turbulence”. In: *Nuclear Fusion* 61.8 (July 2021), p. 086017.

[71] B. N. Rogers, J. F. Drake, and A. Zeiler. “Phase Space of Tokamak Edge Turbulence, the $L - H$ Transition, and the Formation of the Edge Pedestal”. In: *Phys. Rev. Lett.* 81 (20 Nov. 1998), pp. 4396–4399.

[72] Bruce D. Scott. “Drift wave versus interchange turbulence in tokamak geometry: Linear versus nonlinear mode structure”. In: *Physics of Plasmas* 12.6 (2005), p. 062314.

[73] H Meyer et al. “H-mode physics of near double null plasmas in MAST and its applications to other tokamaks”. In: *Nuclear Fusion* 46.1 (Dec. 2005), pp. 64–72.

[74] T. Eich et al. “Turbulence driven widening of the near-SOL power width in ASDEX Upgrade H-Mode discharges”. In: *Nuclear Fusion* 60.5 (Apr. 2020), p. 056016.

[75] W. Suttrop et al. “Experimental conditions to suppress edge localised modes by magnetic perturbations in the ASDEX Upgrade tokamak”. In: *Nuclear Fusion* 58.9 (July 2018), p. 096031.

[76] A. Loarte et al. “Progress on the application of ELM control schemes to ITER scenarios from the non-active phase to DT operation”. In: *Nuclear Fusion* 54.3 (Feb. 2014), p. 033007.

[77] D.G. Whyte et al. “I-mode: an H-mode energy confinement regime with L-mode particle transport in Alcator C-Mod”. In: *Nuclear Fusion* 50.10 (Aug. 2010), p. 105005.

[78] A.E. Hubbard et al. “Physics and performance of the I-mode regime over an expanded operating space on Alcator C-Mod”. In: *Nuclear Fusion* 57.12 (Oct. 2017), p. 126039.

[79] F. Ryter et al. “I-mode studies at ASDEX Upgrade: L-I and I-H transitions, pedestal and confinement properties”. In: *Nuclear Fusion* 57.1 (Oct. 2016), p. 016004.

[80] I. Cziegler et al. “Turbulence Nonlinearities Shed Light on Geometric Asymmetry in Tokamak Confinement Transitions”. In: *Phys. Rev. Lett.* 118 (10 Mar. 2017), p. 105003.

[81] A. E. Hubbard et al. “Edge energy transport barrier and turbulence in the I-mode regime on Alcator C-Mod”. In: *Physics of Plasmas* 18.5 (2011), p. 056115.

[82] D. Silvagni et al. “I-mode pedestal relaxation events at ASDEX Upgrade”. In: *Nuclear Fusion* 60.12 (Oct. 2020), p. 126028.

[83] P. Manz et al. “Physical mechanism behind and access to the I-mode confinement regime in tokamaks”. In: *Nuclear Fusion* 60.9 (Aug. 2020), p. 096011.

[84] P. C. Stangeby. *The Plasma Boundary of Magnetic Fusion Devices*. Series in Plasma Physics and Fluid Dynamics. Taylor & Francis, 2000. ISBN: 9780750305594.

[85] K. H. Burrell et al. “Quiescent double barrier high-confinement mode plasmas in the DIII-D tokamak”. In: *Physics of Plasmas* 8.5 (2001), pp. 2153–2162.

[86] E. Viezzer. “Access and sustainment of naturally ELM-free and small-ELM regimes”. In: *Nuclear Fusion* 58.11 (Sept. 2018), p. 115002.

[87] Y. Takase et al. “Radiofrequency-heated enhanced confinement modes in the Alcator C-Mod tokamak”. In: *Physics of Plasmas* 4.5 (1997), pp. 1647–1653.

[88] B. LaBombard et al. “New insights on boundary plasma turbulence and the quasi-coherent mode in Alcator C-Mod using a Mirror Langmuir Probe”. In: *Physics of Plasmas* 21.5 (2014), p. 056108.

[89] L. Gil et al. “Stationary ELM-free H-mode in ASDEX Upgrade”. eng. In: *46th EPS Conference on Plasma Physics*. 2019.

[90] M. Faitsch et al. “Broadening of the power fall-off length in a high density, high confinement H-mode regime in ASDEX Upgrade”. In: *Nuclear Materials and Energy* 26 (2021), p. 100890. ISSN: 2352-1791.

[91] G.F. Harrer et al. “Parameter dependences of small edge localized modes (ELMs)”. In: *Nuclear Fusion* 58.11 (Sept. 2018), p. 112001.

[92] M.L. Reinke et al. “Radiative heat exhaust in Alcator C-Mod I-mode plasmas”. In: *Nuclear Fusion* 59.4 (Mar. 2019), p. 046018.

[93] Arne Kallenbach et al. “Developments towards an ELM-free pedestal radiative cooling scenario using noble gas seeding in ASDEX Upgrade”. In: *Nuclear Fusion* (Sept. 2020).

[94] R. Pánek et al. “Status of the COMPASS tokamak and characterization of the first H-mode”. In: *Plasma Physics and Controlled Fusion* 58.1 (2016), p. 014015.

[95] S. Coda et al. “Overview of the TCV tokamak program: scientific progress and facility upgrades”. In: *Nuclear Fusion* 57.10 (June 2017), p. 102011.

[96] S J Fielding et al. “H-modes on COMPASS-D with high-power ECRH”. In: *Plasma Physics and Controlled Fusion* 40.5 (May 1998), pp. 731–735.

[97] R Pánek et al. “Reinstallation of the COMPASS-D tokamak in IPP ASCR”. In: *Czechoslovak Journal of Physics* 56.2 (2006), B125–B137.

[98] P. Bilkova et al. “High resolution Thomson scattering on the COMPASS tokamak—extending edge plasma view and increasing repetition rate”. In: *Journal of Instrumentation* 13.01 (Jan. 2018), pp. C01024–C01024.

[99] J. Adámek et al. “Direct Measurements of the Electron Temperature by a Ball-pen/Langmuir probe”. In: *2nd EPS Conference on Plasma Physcs*. Vol. 29. 2005.

[100] H. Meyer et al. “Overview of physics studies on ASDEX Upgrade”. In: *Nuclear Fusion* 59.11 (July 2019), p. 112014.

[101] D Prisiazhniuk et al. “Density fluctuation correlation measurements in ASDEX Upgrade using poloidal and radial correlation reflectometry”. In: *Plasma Physics and Controlled Fusion* 60.7 (May 2018), p. 075003.

[102] E. Joffrin et al. “Overview of the JET preparation for deuterium–tritium operation with the ITER like-wall”. In: *Nuclear Fusion* 59.11 (Aug. 2019), p. 112021.

[103] V.K. Gusev et al. “Review of Globus-M spherical tokamak results”. In: *Nuclear Fusion* 55.10 (July 2015), p. 104016.

[104] B. B. Kadomtsev. “Tokamaks and dimensional analysis”. In: *Soviet Journal of Plasma Physics* 1.295 (1975).

[105] D C McDonald et al. “The impact of statistical models on scalings derived from multi-machine H-mode threshold experiments”. In: *Plasma Physics and Controlled Fusion* 48.5A (Apr. 2006), A439–A447.

[106] Annette J Dobson and Adrian G Barnett. *An introduction to generalized linear models*. CRC press, 2018.

[107] Skipper Seabold and Josef Perktold. “statsmodels: Econometric and statistical modeling with python”. In: *9th Python in Science Conference*. 2010.

[108] Geert Verdoolaege and Jean-Marie Noterdaeme. “Robust scaling in fusion science: case study for the LH power threshold”. In: *Nuclear Fusion* 55.11 (2015), p. 113019.

[109] A. Murari et al. “A statistical methodology to derive the scaling law for the H-mode power threshold using a large multi-machine database”. In: *Nuclear Fusion* 52.6 (May 2012), p. 063016.

[110] A. Murari et al. “Non-power law scaling for access to the H-mode in tokamaks via symbolic regression”. In: *Nuclear Fusion* 53.4 (Mar. 2013), p. 043001.

[111] OJ Kardaun, A Kallenbach, and P McCarthy. *Next step tokamak physics: confinement-oriented global database analysis*. Tech. rep. 2001.

[112] Judea Pearl. *Causality: models, reasoning and inference*. Vol. 29. Springer, 2000.

[113] Peter Spirtes et al. *Causation, prediction, and search*. MIT press, 2000.

[114] B Scott. “Three-dimensional computation of drift Alfvén turbulence”. In: *Plasma Physics and Controlled Fusion* 39.10 (Oct. 1997), pp. 1635–1668.

[115] B. Scott. “Computation of Warm-Ion Drift Alfvén Turbulence”. In: *Contributions to Plasma Physics* 38.1-2 (1998), pp. 171–176.

[116] Bruce D Scott. “Computation of electromagnetic turbulence and anomalous transport mechanisms in tokamak plasmas”. In: *Plasma Physics and Controlled Fusion* 45.12A (Nov. 2003), A385–A398.

[117] P. Manz et al. “Poloidal asymmetric flow and current relaxation of ballooned transport during I-phase in ASDEX Upgrade”. In: *Physics of Plasmas* 23.5 (2016), p. 052302.

[118] Bruce D Scott. “Energetics of the interaction between electromagnetic ExB turbulence and zonal flows”. In: *New Journal of Physics* 7 (Apr. 2005), pp. 92–92.

[119] L. Schmitz. “The role of turbulence–flow interactions in L- to H-mode transition dynamics: recent progress”. In: *Nuclear Fusion* 57.2 (2017), p. 025003.

[120] Anna Kostic. “LH transition with different X-point heights in the COMPASS tokamak”. MA thesis. Nancy,France: University of Lorraine, 2013.

[121] D.I. Réfy et al. “Identity of the JET M-mode and the ASDEX Upgrade I-phase phenomena”. In: *Nuclear Fusion* 60.5 (Mar. 2020), p. 056004.

[122] A.O. Brown and R.J. Goldston. “Generalization of the Heuristic Drift SOL model for finite collisionality and effect on flow shearing rate vs. interchange growth rate”. In: *Nuclear Materials and Energy* 27 (2021), p. 101002. ISSN: 2352-1791.

[123] T. Happel et al. “Approaching detachment in I-mode—response of core confinement and the edge pedestal in the ASDEX Upgrade tokamak”. In: *Nuclear Fusion* 61.3 (Feb. 2021), p. 036026.

[124] John Salvatier, Thomas V Wiecki, and Christopher Fonnesbeck. “Probabilistic programming in Python using PyMC3”. In: *PeerJ Computer Science* 2 (2016), e55.

Prohlašuji, že jsem tuto disertaci vypracoval samostatně a použil jsem pouze podklady (literaturu, projekty, SW, atd.) uvedené v přiloženém seznamu.

Nemám závažný důvod proti použití tohoto školního díla ve smyslu § 60 Zákona č. 121/2000 Sb., o právu autorském, o právech souvisejících s právem autorským a o změně některých zákonů (autorský zákon).

V Praze dne 1.9.2021